ABSTRACT

Title of dissertation: SEDIMENT SUSPENSION EVENTS FROM RIPPLE BEDS IN OSCILLATORY FLOW: EXPERIMENTS

Philip Leland Knowles
Doctor of Philosophy, 2009

Dissertation directed by: Associate Professor Kenneth T. Kiger
Department of Mechanical Engineering

An experimental sediment flume is used to investigate sediment transport mechanics within an oscillatory turbulent boundary layer over a mobile sediment bed in the ripple bed regime. Two-phase PIV is utilized to simultaneously capture data from each phase, allowing examination of suspension mechanisms, carrier phase stresses, and to obtain statistics to describe the momentum exchange between the phases. The technique employs median filtering, as well as size and brightness criteria to separate and accurately identify each phase. Independent well-conditioned tests have been conducted to improve the algorithm to account for the imaging conditions encountered in the vicinity of a mobile bed in order to minimize cross-talk between the phases and allow quantification of the dispersed phase concentration. Results show that large-scale vortical structures are responsible for the ejection of sediment from the bed into the outer flow. These structures are a significant source of turbulent transport, but their overall contribution to the bed stress is small compared to the mean flow. Triple decomposition of the equations of motion show

that long time averaged sediment flux is of similar magnitude to cyclic fluctuations and the time averaged flow consists of two counter rotating cells. Turbulent kinetic energy created at flow reversal advects over the sediment bed and keeps particles suspended in the flow. Calculation of the vertical particle drag, body force, and convection terms revels that at flow reversal the body force terms are larger than the drag causing the particles on average to settle. The particle convection terms are small compared to particle drag and body force terms. Some of the terms most significant in the particle drag are the fluctuating components indicating that the turbulence is keeping the particles suspended in the outer flow.

SEDIMENT SUSPENSION EVENTS FROM RIPPLE BEDS IN OSCILLATORY FLOW: EXPERIMENTS

by

Philip Leland Knowles

Dissertation submitted to the Faculty of the Graduate School of the
University of Maryland, College Park in partial fulfillment
of the requirements for the degree of
Doctor of Philosophy
2009

Advisory Committee:
Associate Professor Kenneth T. Kiger, Chair
Associate Professor Elias Balaras
Professor Richard Calabrese
Professor James Duncan
Professor James Wallace

Table of Contents

List of Tables iii

List of Figures iv

1 Introduction 1
1.1 Statement of the problem . . . 1
1.2 Phase coupling . . . 3

2 Literature review 8
2.1 Previous work . . . 8

3 Experimental Goals, facility, and measurement devepment 22
3.1 Goals . . . 22
3.2 Experimental facility . . . 22
3.2.1 qualification of facility . . . 24
3.3 Introduction to Experimental technique . . . 32
3.4 Image processing and dispersed phase identification . . . 38
3.4.1 Dispersed Phase particle identification . . . 40
3.5 Quantification of measurement errors . . . 43

4 Using light sheet technque for concentration measurements 45
4.1 Single particle light scattering . . . 45
4.2 Calibration procedure for effective detection volume . . . 53
4.2.1 Concentration validation . . . 59

5 Results and discussion 66
5.1 Description of the flow . . . 66
5.2 Particle momentum equation development . . . 79
5.2.1 Sediment quantities . . . 85
5.2.2 Conservation equation terms . . . 92

6 Conclusion 100

A Experimental facility drawings 105

Bibliography 143

List of Tables

3.1 Test conditions 31

4.1 concentration multiplied by the absorption coefficient for Beer's law of C_1, C_2, and C_3 respectively 51

List of Figures

2.1 Rippled bed forms observed in oscillatory flow [2] 9

2.2 Experiments showing collapse of $\frac{a}{\lambda}$ on a single line for $\frac{\rho D}{(\rho_s-\rho)g\tau^2} < 5x10^{-5}$ [2] 11

2.3 Hand-drawn concentration profiles. The curves show a continuous transition from upward convex for fine sand to upward concave for course sand. The numbers on the curves indicate the grain size interval in millimeters [19] 15

3.1 Drawing of UMD oscillating water channel (all dimensions in mm) . . 23

3.2 Sketch of experimental environment 24

3.3 Schematic showing test section with sediment and false floor used to qualify oscillating sediment tunnel performance by examining boundary layer characteristics. 25

3.4 All plots are for sinusoidal oscillations with U_{max} = 0.30 m/s and period=8 sec. a) wall normal variation of stream-wise velocity plotted with the analytical Stokes oscillating plate solution, b) same as a) but smaller region depicted to show near-wall behavior, c) wall normal variation of stream-wise RMS velocity, and d) span-wise variation of the stream-wise velocity. 26

3.5 All plots are for sinusoidal oscillations with U_{max} = 1.47 m/s and period=7 sec. a) wall normal variation of stream-wise velocity plotted with the analytical Stokes oscillating plate solution, b) same as a) but smaller region depicted to show near-wall behavior, c) wall normal variation of stream-wise RMS velocity, and d) span-wise variation of the stream-wise velocity. 27

3.6 Regime map for UMD oscillating water channel where U_{max} is the maximum velocity for the sinusoidal velocity forcing and τ is the period. The solid black line indicates the regimes possible in the UMD oscillating water channel 28

3.7 Ripple profile non-dimensionalized by the ripple wavelength (λ) . . . 29

3.8 Ripple wavelength (red) plotted with previous experiments in the literature [2] 30

3.9 Approximate Graphical representation of imaged two-phase PIV regions in red and regions that can be obtain using symmetry of the flow in green. 32

3.10 Schematic of experimental measurement techniques used in dilute flow 33

3.11 Schematic of image processing: (a) the original 2 phase PIV image, (b) dispersed phase only image constructed from applying median filter to original image, (c) carrier phase tracer particles only image constructed from subtracting image b from image a, (d) velocity field for dispersed phase, (e) velocity field for carrier phase, (f) 39

3.12 Particle discrimination sequence from a 10mmx10mm region of a single image. (a) Unmodified two-phase PIV image, (b) image after the median filter is applied, (c) all continuous objects identified, and (d) objects identified as particles based on size and brightness 40

3.13 Two-phase PIV image showing particles that should be identified as valid and invalid samples of dispersed phase. (a) raw image, (b)(c)(d) valid images, invalid due to (e) blocked particle image, (f) particle outside of light sheet but illuminated by bed reflections, and (g) excessive particle concentration preventing identification of discrete objects. 42

3.14 Dispersed phase sub-pixel interpolation error from artificially displacing 50 particles shifted 1000 times between a 0 and 1 pixel offset. Each of the 50,000 data points is represented by blue circle. 44

4.1 Incident light source on a particle 46

4.2 Normalized laser sheet intensity for a) concentration C_0 and f) concentration C_3. 1/e sheet width (green lines with triangles) and $1/(e^2)$ (red lines with circles) based on the mean sheet intensity in the center/top hat portion of the sheet. Profiles b) through d) and g) through i) are intensity profile plots at 120 mm, 60 mm, and 0 mm respectfully from a) and f). The profiles in e) are the intensity profiles in b) through d) normalized by the mean intensity in the center of the sheet and the $1/e$ sheet width. The profiles in j) are the intensity profiles in g) through i) normalized by by the mean intensity in the center of the sheet and the $1/e$ sheet width. 49

4.3 Normalized energy flux vs distance from the sediment bed for C_0, C_1, C_2, and C_3 concentrations of tracer particles, and Beers law fits to the energy flux curves 50

4.4 Iso-contours of particle brightness vs z for a typical single particle. Nominal light sheet position and $1/e$ thickness denoted by the grey band 55

4.5 Average particle brightness vs distance from the center of the light sheet for particles at a) y=6 mm, b) y=17 mm, and c) y=34 mm, with and without the reflective bed. Particle size vs distance from the center of the light sheet for particles at d) y=6 mm, e) y=17 mm, and f) y=34 mm, with and without the reflective bed. 57

4.6 Effective measurement depth in the light sheet of individual particles with and without a reflective sediment bed along with 1/e sheet width measurements with and without tracer particles. Fit lines are a least squares fit to the individual particles 60

4.7 Measured vs actual sediment particle volume fraction for various average brightness identification criteria 61

4.8 Particle concentration using $1/e$ sheet width and particle concentration using sheet width obtain directly from traversing particles through the light sheet. Dash-dot lines are $\pm 15\%$ error bounds. . . . 62

4.9 Measured vs actual sediment particle volume fraction for various average brightness identification criteria. Dotted lines are $\pm 15\%$ error bounds. 63

4.10 Uncorrected and corrected ensemble averaged particle volume fraction of a sediment cloud traversing over a ripple bed with ripple crest located at the origin and ripple wavelength (λ) 65

5.1 Fluid stream lines with the background colored by fluid velocity magnitude at t/τ=0.00, 0.09, 0.16, 0.27, 0.33, 0.38, 0.44, and 0.49 67

5.2 Turbulent kinetic energy of the fluid at t/τ=0.00, 0.09, 0.16, 0.27, 0.33, 0.38, 0.44, and 0.49 68

5.3 Fluid Reynolds stress at t/τ=0.00, 0.09, 0.16, 0.27, 0.33, 0.38, 0.44, and 0.49 70

5.4 Particle stream lines with the background colored by particle volume fraction at t/τ=0.00, 0.09, 0.16, 0.27, 0.33, 0.38, 0.44, and 0.49 72

5.5 Filled contour plots of fluid Reynolds stress with contour lines of particle volume fraction on the left and filled contour plots of the difference between fluid Reynolds stress and particle Reynolds stress on the right $\langle u'_f v'_f \rangle - \langle u'_p v'_p \rangle$ at t/τ=0.00, 0.09, 0.16, and 0.27 with the origin located at the tip of the ripple crest 74

5.6 Filled contour plots of fluid Reynolds stress with contour lines of particle volume fraction on the left and filled contour plots of the difference between fluid Reynolds stress and particle Reynolds stress on the right $\langle u'_f v'_f \rangle - \langle u'_p v'_p \rangle$ at t/τ=0.33, 0.38, 0.44, and 0.49 with the origin located at the tip of the ripple crest 75

5.7 $\langle u_f \rangle \langle v_f \rangle$ and $\langle u'_f v'_f \rangle$ integrated over the entire ripple wavelength in the stream wise direction versus time. Plots in the middle are instantaneous realizations of velocity magnitude at local maxima of the coherent stress with fluid stream lines in white and the integral path line in green. Plots on the right are instantaneous realizations of fluid Reynolds stress at local maxima with the red line indicating the integral path. 77

5.8 Qualitative illustration of ripple shape morphology. Colored arrows indicate direction of flow for the corresponding colored ripple profile. 79

5.9 Ensemble averaged particle flux integrated over entire wavelength at y/λ=0.03, 0.10, 0.17, and 0.24 as a function of time 85

5.10 Ensemble averaged particle density (g/cm^3) integrated over the ripple wavelength at y/λ=0.03, 0.10, 0.17, and 0.24 as a function of time. Above the plot are instantaneous realizations of particle density at various times labeled T1, T2, T3, and T4, which correspond to various peaks in the ensemble averaged particle density integrated over the ripple wavelength, while the dashed lines in the instantaneous realizations of particle density correspond to the data locations integrated in the lower plot. 87

5.11 Fluid stream lines in black solid lines and particle stream lines in black dashed lines with the background colored by the time averaged vertical sediment flux $g/(m^2\ s)$ 89

5.12 Nielsen's diffusive concentration model 2.9 for time averaged concentration over the ripple crest along with Davies and Thorne's suggested reference concentration update to Nielsen's model compared to UMD experimental data and least squared exponential fit to data. Data is shown in a) linear and b) normalized semilog scale 91

5.13 Time averaged particle conservation of mass terms, a) $\rho_p\widetilde{\alpha_p}\ \widetilde{u_p}$, b) $\rho_p\widetilde{\alpha_p}\ \widetilde{v_p}$, c) $\rho_p\widetilde{\widehat{\alpha_p}\ \widehat{u_p}}$, d) $\rho_p\widetilde{\widehat{\alpha_p}\ \widehat{v_p}}$, e) $\rho_p\widetilde{\alpha_p'\ u_p'}$, f) $\rho_p\widetilde{\alpha_p'\ v_p'}$ 93

5.14 Plots on the left are the total particle drag in the y direction, while the plots on the right are the magnitude of body forces at t/τ=0.00, 0.09, 0.16, and 0.27 with the origin located at the tip of the ripple crest. Solid black lines on each of the plots indicates the boundaries between measurement regions. 95

5.15 Plots on the left are the total particle drag in the y direction, while the plots on the right are the magnitude of body forces at t/τ=0.33, 0.38, 0.44, and 0.49 with the origin located at the tip of the ripple crest. Solid black lines on each of the plots indicates the boundaries between measurement regions. 96

5.16 Plots of the sum of the convection terms in the particle momentum equation in the y direction at t/τ=0.00, 0.09, 0.16, 0.27, 0.33, 0.38, 0.44, and 0.49. Solid black lines on each of the plots indicates the boundaries between measurement regions. 97

Chapter 1

Introduction

1.1 Statement of the problem

The migration of sediment on the continental shelf is an important topic in coastal studies. The migration of sediment plays a key role in the accurate prediction of coastal flooding, coastal erosion, and the dispersal of man made pollutants. This transport is controlled by the combination of two features of the flow environment: the mean current and the oscillatory wave motion. The mean current produces a benthic boundary layer on the ocean floor, while the surface wave motion produces an oscillating boundary layer superimposed on the benthic boundry layer and is typically much smaller, producing a more intense shear on the sediment bed. As a result, this oscillatory component (in conjuction with the mean flow) often plays a dominant factor in the mobilization of particles from the bed. When sediment transport simulations are performed on a regional scale, by necessity the grid size must be appreciably larger than the length scales of the flow responsible for sediment transport. Therefore the effects of sediment transport at these scales typically must be modeled.

The flow near the sediment bed is by its very nature an unsteady liquid-solid multi-phase flow. The sediment bed geometry and suspended sediment load are a function of environmental conditions, both of which have an effect on the shear

stress at the bottom of the oscillatory boundary layer. To accurately predict the bottom boundary layer, the modification of the shear stress by the presence of the sediment particles must be understood. In general, there are two bed form conditions observed in oscillatory sediment transport: rippled bed and sheet flow. The rippled bed condition corresponds to conditions where small ripple like structures form, creating a large effective roughness that generates and interacts with coherent fluid structures. Ripple bed geometries can result in 2D or 3D ripple shapes depending on characteristics of the oscillatory motion. Sheet flow is where the entire sediment bed becomes fluidized, resulting in a dense moving granular flow. The large mass and volume fractions of suspended sediment near the bed can also alter the carrier phase flow due to their mutual dynamic interaction. The modification of the carrier phase flow by the presence of the dispersed phase particles must be understood to accurately predict the bottom boundary layer flow quantities.

Multiphase flows in general are categorized according to the relative effective magnitude of the dispersed phase properties on the carrier phase flow properties, which can be dependant on the volume fraction and mass fraction of the dispersed phase. If there is no perceptible effect on the carrier phase from the presence of the dispersed phase, the flow is said to be one-way coupled. For larger volume fractions, the presence of the dispersed phase can have a measurable effect on the carrier phase and is therefore referred to as two-way coupling. Under sediment transport conditions, the flow near the sediment bed is two-way coupled, while the flow farther away from the sediment bed is one-way coupled.

1.2 Phase coupling

The equations of motion for the carrier and dispersed phase can be described in a Lagrangian or Eularian frame of reference. The Lagrangian method describes the phase as a collection of discrete elements, requiring calculation of the forces on the surface of the element boundary and tracking the motion of each and every individual element. For large numbers of particles, this approach is computationally expensive and typically practical for only simplified, fundamental problems. In the Eularian approach, the fluid motion is described using the necessary properties (density, velocity, pressure, etc.) as functions of space and time. The Eularian equation of motion for each phase is described by:

$$\frac{\partial}{\partial t}(\rho_k u_{i,k}) + \frac{\partial}{\partial x_j}(\rho_k u_{i,k} u_{j,k}) = -\frac{\partial p_k}{\partial x_i} + \frac{\partial \tau_{ij,k}}{\partial x_j} + \rho_k g_{i,k} \tag{1.1}$$

where k indicates the phase; i,j=1, 2, and 3 are the three coordinate directions x, y, z, u is the velocity, p is the pressure, and τ is the stress tensor. Particle-fluid interactions enter into equation 1.1 in the form of boundary conditions at the particle-fluid interface. From a mathematical perspective, this means that the governing equations for the carrier phase are no longer continuous and differentiable everywhere when observing the flow on a macro scale. Also, jump boundary conditions must be applied across the phase interfaces to properly conserve mass, momentum, and energy. The derivation of the constitutive equations for this type of domain is considerably more complicated than for the continuous single phase flow. The constitutive equations can be solved on a micro-scale between the particles assuming moving boundaries, but this procedure is prohibitively expensive when considering

large scale systems.

Through proper averaging of the constitutive equations, the mean properties can be approximated as continuous and calculated on a macro scale. Fortunately in engineering applications, the microscopic details of the flow near a fluid-particle interface rarely need to be resolved. However, the effect of the micro-scale physics can have a significant effect on the macroscopic flow, and therefore the micro-scale effects need to be represented in a description of the macro-scale flow. The effects of the fluid property fluctuations around its mean value and the presence of the dispersed phase must be conserved in the equations to accurately represent the carrier phase flow, which is non-trivial. The ensemble averaged Eularian momentum balance can be written as [1]:

$$\begin{aligned}\frac{\partial}{\partial t}(\rho_k \alpha_k \langle u_{i,k}\rangle) + \frac{\partial}{\partial x_j}(\alpha_k \rho_k \langle u_{i,k}\rangle \langle u_{j,k}\rangle) = \\ -\frac{\partial}{\partial x_j}(\alpha_k \langle p_k\rangle) + \frac{\partial}{\partial x_j}[\alpha_k (T^V_{ij,k} + T^T_{ij,k})] + \alpha_k \rho_k \langle g_i\rangle + \langle M_{i,k}\rangle\end{aligned} \tag{1.2}$$

where k indicates the phase, i,j=1, 2, 3 are the three coordinate directions, the ($\langle\ \rangle$) indicates the ensemble average of the quantity between the angle brackets, i.e. $\langle F\rangle(x_o, y_o, z_o) \equiv \lim_{N\to\infty} \frac{1}{N} \sum_{n=1}^{N} f(x_o, y_o, z_o, n)$, α_k is the volume fraction for the k$^{\text{th}}$ phase, $\langle u_i\rangle$ is the mass weighted mean velocity in the i$^{\text{th}}$ direction, $T^V_{ij,k}$ is the average viscous stress tensor ($T^V_{ij,k} = \mu \frac{\partial \langle u_{i,k}\rangle}{\partial x_j}$) and is zero for the sediment in this case, $T^T_{ij,k}$ is the turbulent stress tensor ($T^T_{ij,k} = \rho u'_{i,k} u'_{j,k}$), the apostrophe indicates the fluctuating component of the quantity relative to the ensemble mean, and $M_{i,k}$ is the momentum source term from interfacial transfer between phases in the i$^{\text{th}}$ direction. By averaging the constitutive equations, a model must be introduced

for the interfacial momentum transfer $M_{i,k}$ and the turbulent stress tensor T_k^T to properly close the averaged equations of motion. The simplest way to model M_i is to formulate a sum of the known interfacial forces as [1]:

$$M_{i,k} = (\langle v_{i,k}^b \rangle - \langle v_{i,k} \rangle)\Gamma_k - M_{m,i} + \frac{\alpha_k}{V_p}(F_i^D + F_i^V + F_i^B + F_i^L + F_i^W) \tag{1.3}$$

where $\widehat{v_{i,k}^b}$ is the ensemble averaged mean velocity of the interface between phases, $\widehat{v_{i,k}}$ is the mean velocity of the k^{th} phase, Γ_k is the mass source term from phase change or chemical reaction, $M_{m,i}$ is the mixture momentum source from surface tension effects, V_p is the volume of a particle, F_i^D is the drag force, F_i^V is the force from virtual mass, F_i^B is the basset history force, F_i^L is the lift force, and F_i^W is the lift force due to the velocity distribution changes around particle near a wall.

The mass source term in equation 1.3 is important when the phase change transfers momentum from one phase to the other. An example of this is evaporating droplets in a gas flow. The droplets exchange momentum with the surrounding fluid through the rapid expansion occurring on the surface of the droplet. The mixture momentum source from surface tension is the second term in equation 1.3 and is important when the Gibbs free energy per unit surface area between the phases is large. This is typically important for liquid and gas flows with large area to volume ratios. The third term is the drag force between the phases. This term is important when the velocity difference between the phases is large, which is typical for the size and density ratios of particles in sediment transport. The virtual mass is the fourth term and is the force required to accelerate the fluid around the particle during relative velocity changes between the phases. This term is important when a particle

experiences a rapid response and the density of the carrier fluid is large. The next term is the Basset history force. This term accounts for the effects of acceleration on the viscous drag and the transient boundary layer development around the particle. This term is significant when the time scale of the forcing oscillations are smaller then the time scale of the particle. The sixth term is the lift force, which is the force normal to the relative velocity of the phases. This term is important when the velocity distribution around a particle is very non-uniform. An example of this is the lift force experienced by particles in shear and rotating flows. The last term is the lift force on a particle near solid walls from the non-uniform fluid velocity near a wall. For the current work we are interested in studying the evolution and transport of suspended sediment. For these conditions, the particles are not evaporating, and surface tension between the particle and fluid is very small, removing the first two terms from equation 1.3. In addition, the time scale of the fluid is much larger then the particle timescale, relegating the Bassett term to a higher order effect. Finally, the scale of the particle size to the fluid velocity is uniform, and the particle velocity will not be evaluated close enough to walls for the wall lift force to be significant. These assumptions make the drag force the dominant interfacial transfer term in equation 1.3 at least to first order. Therefore, at least to first order, we can close the interfacial transport between the phases using a relationship for the drag on a particle. However, detailed information about the slip velocity between the fluid and particles is still required in order to appropriately close the equations. One of the goals of this work is to provide detailed simultaneous measurements of both the carrier phase fluid and the sediment particle velocities to understand how interfacial

transport of momentum plays a role in the governing equations, so that the equations can be properly closed. This work will two-phase PIV to measure the velocity of both phases simultaneously and develope a particle detection extension to two-phase PIV to obtain measurements of the volume fraction as well.

Chapter 2

Literature review

2.1 Previous work

Sediment bed geometry strongly influences the structure and turbulence near the sediment bed. In general, the bed geometry can be classified into two regimes, ripple bed conditions and sheet flow. Ripple beds are where small ripple structures form in the sediment bed, the ripples themselves form and interact with flow structures significantly modifying the flow. Sheet flow is where the sediment bed becomes a dense moving granular flow near the surface. Most early research on coastal sediment transport was focused on characterizing the geometry of the sediment bed under various oscillating conditions. While no one has been completely successful at predicting ripple geometry as a function of flow parameters, various ripple geometries have be observed naturally and in the laboratory, (see figure 2.1 [2]). From an initially planer bed subjected to wave motion in the ripple bed regime, rolling grain ripples are the first to form [3]. Initially, these ripples have a small height (η) to wavelength (λ) ratio ($\eta/\lambda < 0.1$), such that the streamlines of the flow follow the contours of the bed and no flow separation occurs. Rolling grain ripples are not typically a stable bed form. As the rolling grain ripples continue to grow in amplitude, they eventually reach the point where separation of the flow from the ripple crest begins. This marks the onset of the vortex ripple regime, where the accumulated

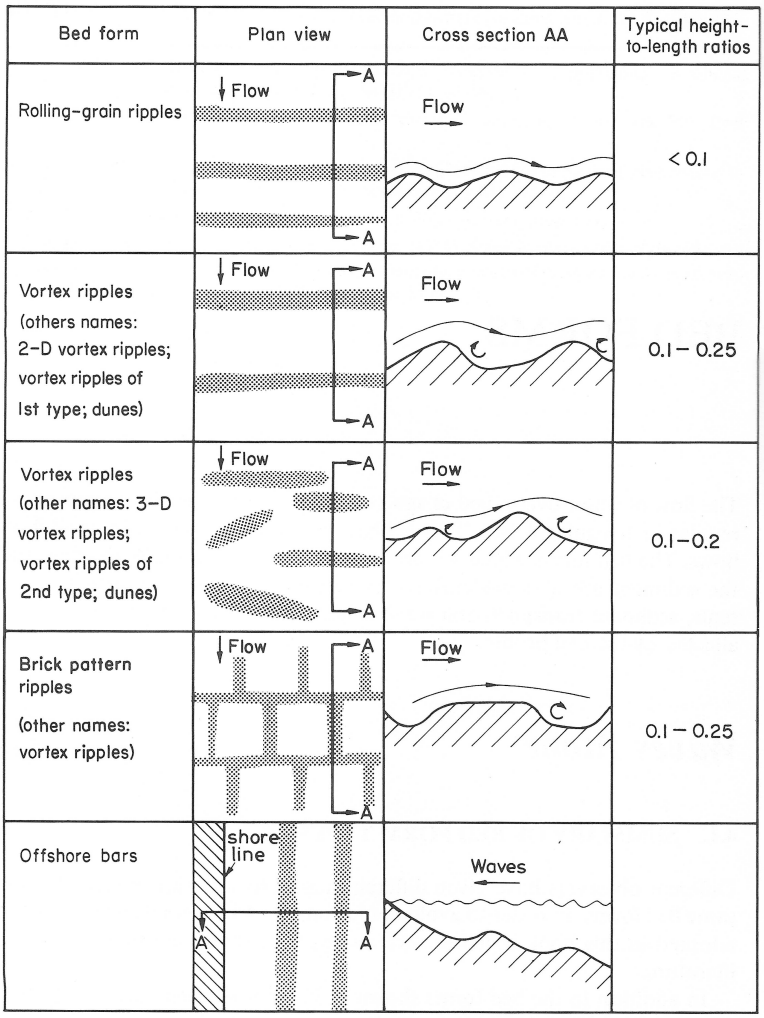

Figure 2.1: *Rippled bed forms observed in oscillatory flow [2]*

vorticity in the separation region is ejected into the flow at every half-cycle, which forces a particular ripple wavelength to form. Vortex ripples are typically classified as two-dimensional or three-dimensional and the process of their transition is a topic of current study. A theoretical study by Anderson (2001) found that rolling grain ripples always form into vortex ripples, however the transition time can be very long if the forcing conditions are close to the minimum forcing required to mobilize the sediment grains. Faraci and Foti (2002) concluded that rolling grain ripples never appear as a stable condition, but only as a transient stage towards the vortex regime.

Close to the ripple-bed-to-sheet-flow transition, brick pattern ripples can form, and on a much larger scale, off shore bars are also classified as large ripples. Because two-dimensional vortex ripples are the bed form most often found in nature [2], the focus of this work will be in that regime.

Mogridge and Kamphuis suggested that ripple geometry was determined by four dimensionless groups [6]:

$$\frac{(\rho_s - \rho)gD^3}{\rho\nu^2}, \frac{\rho D}{(\rho_s - \rho)g\tau^2}, \frac{a}{\lambda}, \frac{\rho_s}{\rho} \tag{2.1}$$

where ρ_s is the density of the sediment, ρ is the density of the fluid, D is the mean diameter of the sediment, τ is the period of the wave oscillation, a is the free stream orbital amplitude, g is the acceleration of gravity, and ν is the kinematic viscosity. The second term is the wave period parameter and determines the maximum ripple wavelength which is dependant on the period, the third term is the ratio of orbital amplitude to ripple wavelength, and the last term is the density ratio between the sediment and the fluid. Sleath completed a regression analysis of previous data and found that for the wave period parameter $\frac{\rho D}{(\rho_s-\rho)g\tau^2} < 5x10^{-5}$, a/λ followed a single curve (see figure 2.2 [2]). Figure 2.2 suggests that for small values of $\frac{\rho D}{(\rho_s-\rho)g\tau^2}$, the wavelength of the sediment is determined by $\frac{\rho D}{(\rho_s-\rho)g\tau^2}$ and a. Prediction of the geometry of the sediment bed is important, as it has an impact on the bed load, sediment flux, and bed stress, which in turn affect the prediction of bottom boundary layer. In fact, most early work was concentrated on predicting the ripple geometry. By studying experimental laboratory and field data, Nielsen (1981) developed two sets of ripple predictor relationships, one for regular waves as found in the laboratory

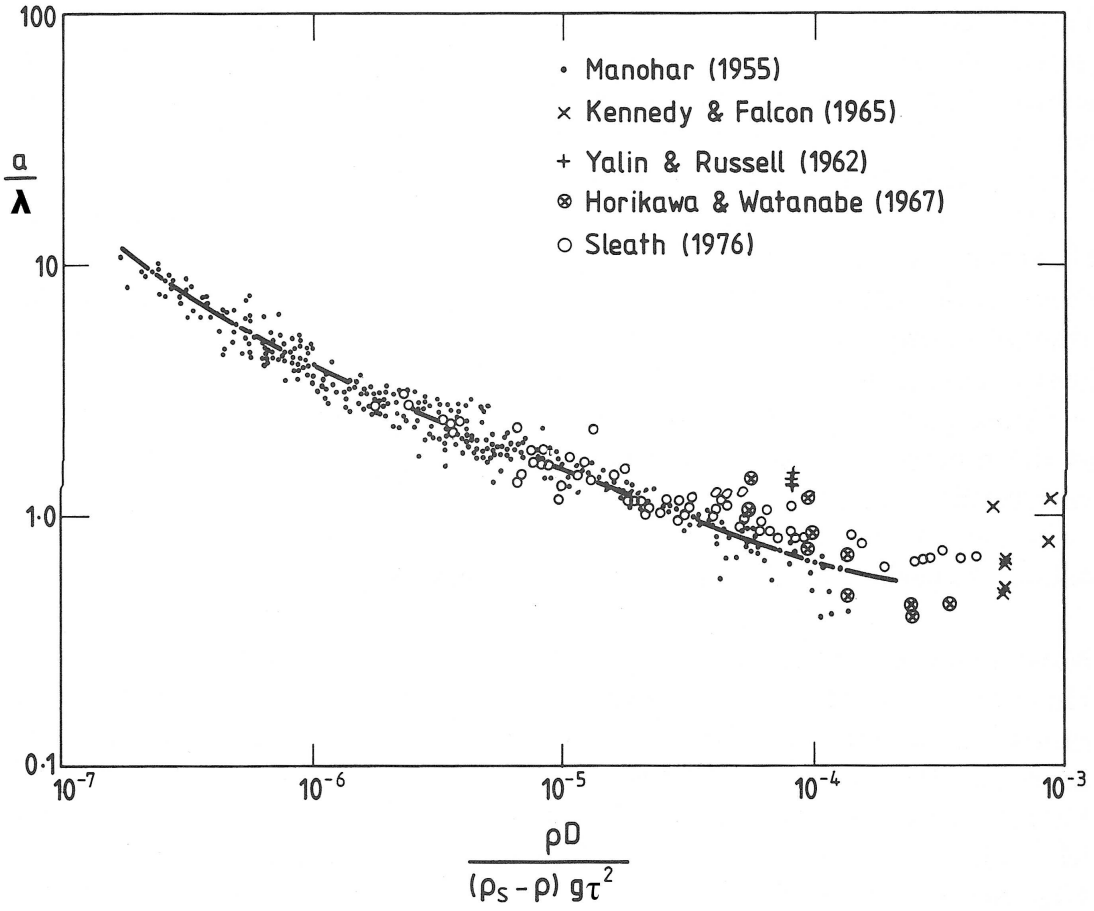

Figure 2.2: *Experiments showing collapse of* $\frac{a}{\lambda}$ *on a single line for* $\frac{\rho D}{(\rho_s-\rho)g\tau^2} < 5x10^{-5}$ *[2]*

and another for irregular waves found in field measurements [7]. For regular waves [7]:

$$\frac{\lambda}{a} = 2.2 - 0.345\Phi^{0.34} \quad for\ 2 < \Phi < 230 \tag{2.2}$$

$$\frac{\eta}{a} = 0.275 - 0.022\Phi^{0.5} \quad for\ \Phi < 156\ and\ 0\ for\ \Phi > 156 \tag{2.3}$$

$$\frac{\eta}{\lambda} = 0.182 - 0.24\Theta_s^{1.5} \quad for\ \Theta_s < 0.83 \tag{2.4}$$

and for irregular waves [7]:

$$\frac{\lambda}{a} = exp(\frac{693 - 0.37ln^8\Phi}{1000 + 0.75ln^7\Phi}) \tag{2.5}$$

$$\frac{\eta}{a} = 12\Phi^{-1.85} \quad for\ \Phi > 10 \tag{2.6}$$

$$\frac{\eta}{\lambda} = 0.342 - 0.34\Theta_s^{0.25} \tag{2.7}$$

where λ is the ripple wavelength, η is the ripple height, Φ is the mobility number and is defined as $\Phi = \frac{.5(a\omega)^2}{(\frac{\rho_s - \rho_f}{\rho_f})gD}$, ρ_s is the density of the sediment, ρ_f is the density of the fluid, and Θ_g is grain roughness Shields parameter ($\Theta_g = 0.5 * f * \Phi$ where $f = exp[5.213(\frac{2.5*D}{a})^{0.194} - 5.977]$). Mogridge et al. (1994) found that he could reduce a set of curves describing the ripple geometries to a single curve using the wave period parameter ($\frac{\rho D}{(\rho_s - \rho)g\tau^2}$). O'Donoghue and Clubb (2001) compared the performance of the ripple predictors proposed by Nielsen (1981), Mogridge et al. (1994), Wiberg and Harris (1994), and Vongviseeomjai (1984). It was found that the predictors proposed by Nielsen (1981) and Mogridge et al. (1994) worked well over the majority of flow parameters studied. However, Nielsen's method over predicted the steepness of the ripples at high mobility numbers. Wiberg and Harris (1994) along with Vongviseeomjai (1984) methods were only reasonable over a small region of the wave period parameter. O'Donoghue and Clubb (2001) commented that all four methods were only applicable to 2-D vortex ripples and fail to predict 3-D vortex ripples. They also noted that at low mobility numbers, the bed form took in excess of 20 hours to reach equilibrium and therefore caution must be taken in analyzing field results where the flow conditions are ever changing.

The majority of research on sediment transport over ripple beds has been focused on understanding how the interaction of the bottom boundary layer with the ripple bed affects sediment transport. Flow separation of the fluid from the ripple

crest causes vortical structures that dominate the sediment transport near the bed. The observance of vortical structures can be traced back to Vincent (1957) who observed jets of fluid being ejected away from the sediment bed during flow reversal using dye dispersed in an oscillating water flume. Analytical solutions to sinusoidal oscillating flow over small height to length ratio under the restrictions of small-amplitude wave theory by Lyne (1971) [13], suggested that long time rotational cells are present in the fluid. However, these solutions are restricted to bed geometries not often found in nature. Point measurements using hot-wire anemometry by Nakato (1977) over the ripple crest and ripple trough, reveled that the time averaged velocity was indeed non-zero almost everywhere studied.

A considerable portion of coastal sediment transport is due to sediment suspended in the flow near the bed. Therefore, it is important to measure suspended sediment concentrations and develop concentration distribution models. Early concentration models were constructed on the basis of gradient diffusion, which rely on the fact that the mixing length is small compared to overall scale. This approach assumes that the upward sediment flux, created from random turbulent mixing, is balanced by the isolated settling velocity of the particles, and models each process using a balanced diffusive flux equation:

$$w_o\widetilde{c} + \epsilon_s \frac{d\widetilde{c}}{dy} = 0 \tag{2.8}$$

where $\epsilon_s = \frac{l_m^2}{t}$ is the effective sediment diffusivity, w_o is the still water particle settling velocity, $\widetilde{c}$ is the time average concentration profile, z is the vertical distance from the bed, l_m is the sediment diffusion mixing length, and t is time. Coleman

(1970) showed that ϵ_s must be a strong function of the relative setting velocity for regions far away from the ripple crest, outside of the influence of vortical structures shed from the bed. Knowing that solving equation 2.8 with a constant ϵ_s results in an exponential curve for the concentration profile, Nieslen (1986) suggested an exponential formulation for the time averaged volume fraction over the ripple crest as:

$$\tilde{c}(y) = C_o * e^{-y/L_s} \tag{2.9}$$

$$C_o = 0.005 * \Theta_p^3 \tag{2.10}$$

$$\Theta_p = \frac{\Theta_g}{(1 - \pi\eta/\lambda)^2} \tag{2.11}$$

$$\Theta_g = \frac{.5 f \rho_s (a\omega)^2}{\rho_s (s-1) g D} \tag{2.12}$$

$$f = e^{5.213(\frac{2.5D}{a})^{0.194} - 5.977} \tag{2.13}$$

$$L_s = 0.075 \frac{a\omega}{w_o}\eta \; for \; \frac{a\omega}{w_o} < 18 \; or \; L_s = 1.4\eta \; for \; \frac{a\omega}{w_o} > 18 \tag{2.14}$$

where Θ_p is a modified Shields parameter to account for the increased velocity near the ripple crest, Θ_g is the grain roughness Shields parameter, f is the grain roughness friction factor, ρ_s is the density of sediment, s is the specific gravity of the sediment, and w_o is the still water settling velocity of the sediment. This model has been shown to predict the time averaged concentration decay length over the ripple crest within a factor of 2, for concentration profiles within $y < 1.5\eta$ from the ripple crest for 89% of experiments tested [16]. Data from Nielsen (1983) and McFetridge and Nielsen (1985) also show that the distribution of $\epsilon_s(z)$ is significantly different for different grain sizes. Also, data from Nakato (1977) and Sleath (1982) of sediment

concentration measurement over ripple beds show that the sediment concentration is a strong function of spatial position as well as time, which such a simple one-dimensional diffusive model doesn't capture.

Nielsen (1983) and McFetridge and Nielsen (1985) examined concentration profiles for various sediment sizes under the same forcing conditions. Figure 2.3

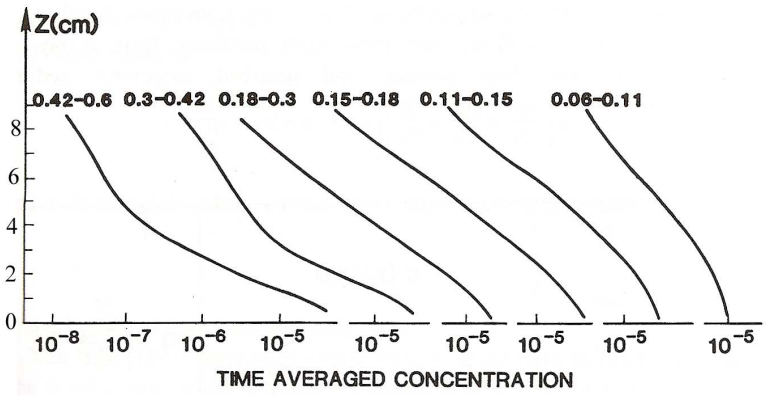

Figure 2.3: *Hand-drawn concentration profiles. The curves show a continuous transition from upward convex for fine sand to upward concave for course sand. The numbers on the curves indicate the grain size interval in millimeters [19]*

shows hand-drawn concentration curves for various sediment sizes above the ripple crest. By comparing the shape of the time averaged concentration profiles above the ripple crest, information about the mechanism for sediment suspension can be investigated. McFetridge and Nielsen (1985) showed that for sediment sizes less than approximately 300 μm, the shape of time averaged concentrations profiles near the bed can be predicted reasonably by gradient diffusion. When the mixing length, l_m, is small compared to the length scale of the sediment concentration distribution, gradient diffusion is more likely to describe the sediment concentration [19]. This is the case for the smallest sediment sizes in figure 2.3. However, when l_m is large as

compared to the length scale of the sediment concentration distribution, then the concentration profile can be described by a convective flux equation [19]:

$$\frac{\partial c}{\partial t} = w_o \frac{\partial c}{\partial y} - \frac{\partial q_c}{\partial y} \tag{2.15}$$

where q_c is the convective flux of sediment and is described using pickup functions to capture the time dependant nature of the concentration. Since large scale vortices are responsible for the ejection of sediment into the flow and flow reversal, the convective flux itself must be a function of height from the bed and time. This lead Lee and Hanes (1996) to use a combined convection-diffusion equation written in the form [20]:

$$\omega_o c + \frac{\partial(\epsilon_s c)}{\partial y} - \omega_o c_0 F(y) = 0 \tag{2.16}$$

where c_0 is a reference concentration and $F(y)$ is a function describing the probability of a particle to reach a height y above the bed.

Thorne, Williams, and Davies, (2002) measured suspended sediment concentration in an oscillation water flume under regular and irregular waves. An acoustic ripple profiler was used to obtain detailed measurements of the bed morphology while the acoustic backscatter system provided single point concentration measurements. Thorne et.al (2002) found that in the region near the bed dominated by vortex formation (less than two ripple heights), the pure diffusion model provides a good representation of the concentration profiles [21]. Above this region, the combined convection-diffusion relation works better for describing the sediment concentration profiles [21].

Earnshaw and Greated (1998) investigated the dynamics of vortices produced

from a fixed styrofoam ripple bed, using PIV to capture the fluid velocity. At flow reversal the vortices begin grow, reaching their maximum circulation strength at maximum flow rate. As the flow decelerates, the vortices begin to dissipate [22]. The size of the vortex reaches a maximum of approximately one ripple height just after maximum flowrate at the same time as maximum circulation[22].

Sleath and Wallbridge (2002) investigated the ejection of sediment from the bed into the flow using Laser Doppler Anemometry (LDA) and a video camera in an oscillating water flume. LDA captured the sediment velocity while the video camera recorded the profile of the sediment along the test section wall. By recording the sediment profile as a function of time, the erosion of sand from the profile is convected outward into the flow and vise versa. Sleath and Wallbridge found two local maxima in the entrainment rate of sediment over the half-cycle: one at flow reversal from the lee vortex and a second associate with maximum flow rate [23]. However, because the sediment profile was measured at the wall, the effects of the side-wall boundary layer on modifying the bed stress, and therefore erosion rates, are unknown.

Sumer, et al. (2003) examined the influence of turbulence in the outer flow of bed load sediment transport in an open channel flow over flat and ripple beds using 0.22 mm particles. External turbulence was created three different ways, using vortices shed from a pipe, short series of grids, and a long series of grids. By using different lengths of grids, different turbulence levels could be obtained. The flow using the turbulence generator was adjusted so that the mean bed shear stress was the same as without the turbulence generator. A sediment trap was located

in the flume to capture sediment suspended in the flow, while LDA was used to measure flow velocities, RMS turbulence, and Reynolds stress profiles at various points. Sumer, et al. observed that the sediment transport rate increased with increasing levels of turbulence. For the ripple bed cases, the sediment transport rate could be increased by as much as 600% with only a 20% increase in turbulence level, showing the strong influence of turbulence to hinder particle settling.

Van der Werf, et al. (2006) measured full field sediment velocity using PIV and sediment concentration using a series of suction probes in an oscillating water flume. The goal of this research was to compare several sediment transport models under regular and irregular wave motion by obtaining highly accurate sediment velocity and concentration as a function of time [16]. Van der Werf, et al. confirmed that in the near-bed region ($y < 2\eta$), the time and bed averaged concentration profiles are best described with a diffusive model. Comparisons in the experimental concentration profile and the concentration decay length proposed by Nielsen (1988) were in good agreement. However, a new reference concentration formula is proposed based on grain-size influence proposed by Bosman and Steetzel (1986) [16].

While there have been a fair number of experimental studies of oscillating sediment transport, the majority of these studies measured either the fluid or the particle velocity [(Dick and Sleath, 1991), (Ribberink and Al-Salem, 1995), (Flores and Sleath, 1998), (Earnshaw and Greated, 1998), (Ahmed and Sato, 2001),(Thorne, Williams, and Davies, 2002), (Sleath and Wallbridge, 2002), (Dohmen-Janssen, Hassan, and Ribberink, 2002), (Sumer, et al. 2003), and (van der Werf, et al.,2006)], but not both simultaneously. Experiments that measured turbulence levels in the fluid,

where done over fixed beds. Horikawa and Mizutani (1992) found that the radius of curvature of the fixed bed ripple crests had a strong influence on both the strength and size of vortices shed at flow reversal. Phase resolved point measurements of the sediment concentration by Bosman (1986), showed that the vortices have an influence of the time dependant sediment concentration. All of these measurements have provided important details about the bulk characteristics of sediment transport. However, to understand the momentum exchange between the two phases, it is necessary to simultaneously measure the carrier and dispersed phase velocities, as well as the phase resolved concentration over a naturally occurring ripple bed.

Most of the numerical modeling for oscillatory sediment transport has been focused on developing an expression for the turbulent eddy diffusivity to be used with the Reynolds Averaged Navier-Stokes equation. Numerical simulations of smooth wall oscillating channel flows has shown that commonly used RANS models (κ-ϵ, κ-ω, etc.) show large errors in predicting the turbulent kinetic energy and Reynolds stress [32]. Scotti and Piomelli postulated that the fundamental assumption that the turbulence is near equilibrium is violated in pulsating flows. Since fluctuations at all scales need to be modeled, RANS models are sensitive to large scale driving conditions in the flow and misrepresent key turbulent quantities in unsteady boundary layers[33].

One of the main problems with modeling the Reynolds stress based on gradient transport and the normal stresses based on equilibrium is that analysis and simulation results show that the Boussinesq approximation is not satisfactory [34]. Simonin, Deutsch, and Boivin (1995) showed that in gas-solid flows, the particle

stress tensor anisotropy increases with the particle relaxation time. These intricate features lead to the development of a higher order equation governing the transport of the particle kinetic stresses derived from the particle equation of motion yielding [35]:

$$\begin{aligned}
&\frac{\partial}{\partial t}+\overline{u_{m,s}}\frac{\partial}{\partial x_m}\langle u'_{i,s}u'_{j,s}\rangle = P_{ij,s}+D_{ij,s}+\Pi_{ij,s}\\
&P_{ij,s}=\langle -u'_{i,s}u'_{m,s}\rangle\frac{\partial\overline{u_{j,s}}}{\partial x_m}-\langle u'_{j,s}u'_{m,s}\rangle\frac{\partial\overline{u_{i,s}}}{\partial x_m}\\
&D_{ij,s}=-\frac{1}{\alpha_s}\frac{\partial}{\partial x_m}[\alpha_s\langle u'_{i,s}u'_{j,s}u'_{m,s}\rangle]\\
&\Pi_{ij,2}=-\langle\frac{\rho_f}{\rho_s}\frac{3}{4}\frac{C_D}{d}S_r[\nu_{i,r}u'_{j,s}+\nu_{j,r}u'_{i,2}]\rangle
\end{aligned} \tag{2.17}$$

where the subscript "f" refers to the carrier phase and the subscript "s" refers to the dispersed phase, $\overline{u_{i,s}}$ is the mean velocity of the dispersed phase, C_D is the coefficient of drag for a single dispersed phase particle, d is the particle diameter, S_r is the magnitude of the apparent slip velocity between the phases, and $v_{i,r}$ is the relative velocity between the particle and fluid. The first term on the right hand side $P_{ij,s}$ is the production by the mean gradient of the particle velocity, while the second term $D_{ij,s}$ represents the transport by the particle velocity fluctuations. The last term $\Pi_{ij,s}$ can be either a production or destruction term depending on the relative magnitude of the particle stress.

Chang and Scotti (2006) investigated sediment transport over vortex ripples using Large Eddy Simulation (LES) while the motion of individual particles was calculated using a modified version of the Maxey and Riley equation [36]. They found that vertical velocity fluctuations were strongest at flow reversal which causes the sediment to remain suspended in the flow [36]. Also, during maximum flow rate,

horizontally aligned vortices retard the settling of the sediment particles near the bed.

Several aspects of the sediment-bottom boundary layer interaction must be better understood to be able to accurately model and predict the effects of sediment transport. Unfortunately, we still lack a comprehensive understanding of the physics involved in oscillatory sediment transport. In fact, most models used to quantify sediment transport are a simple extension of techniques developed from studying steady flows. The lack of detailed experiments measuring the phase resolved sediment flux has made comparison difficult.

Chapter 3

Experimental Goals, facility, and measurement devepment

3.1 Goals

The primary goals of the experiment are to:

1. Simultaneously measure the fluid and dispersed phase motion, so that the interfacial transport terms can be measured, reported, and compared to numerical simulations.

2. Quantify fluid motion responsible for the suspension of particles

3. Examine terms in constitutive equations focusing on momentum transfer between the phases.

3.2 Experimental facility

To reproduce the oscillatory boundary layer observed on the continental shelf, the UMD oscillating water channel has been constructed (see figure 3.1). The test section for the UMD oscillating water channel has interior dimensions of 30 cm wide x 375 cm long x 45 cm tall, with 15 cm of the height occupied by sediment bed. The oscillatory motion is controlled by a user programmable 7.6 hp feedback controlled piston. This allows for maximum sinusoidal velocities of 2 m/s at a period (τ) of 2 seconds. Longer periods at slower velocities are achievable depending on the stroke

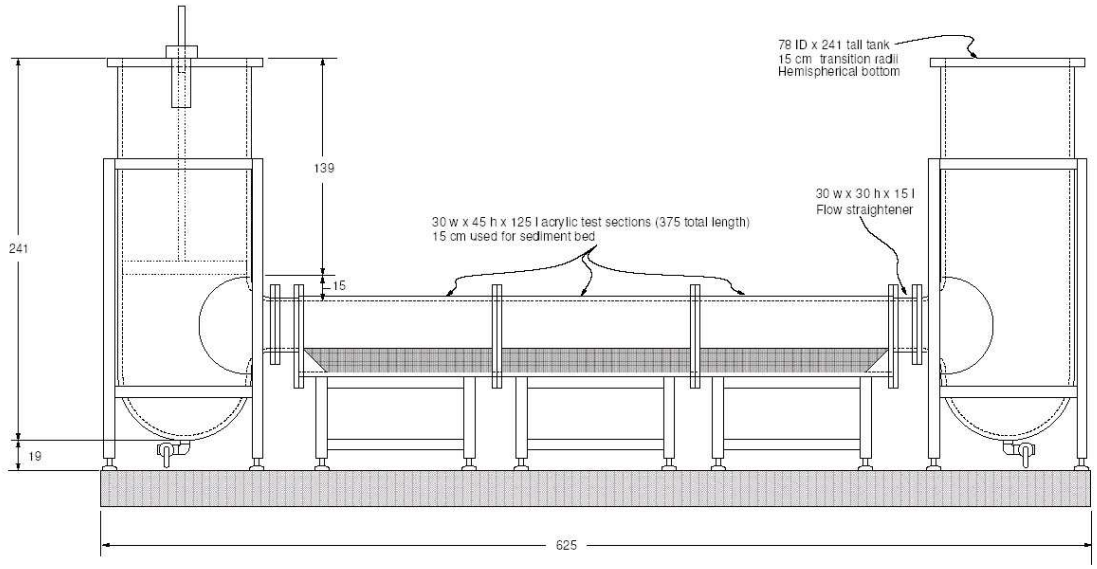

Figure 3.1: *Drawing of UMD oscillating water channel (all dimensions in mm)*

required.

Figure 3.2 shows a sketch of the test section measurement environment. The sediment bed was composed of a 15cm thick mobile layer of 240μm soda lime glass spheres (sieved between 218μm and 268μm) with a specific gravity of 2.5, while the continuous phase water (300 mm thick) was seeded with hollow silver-coated glass spheres with a mean diameter of 15 μm. A 5W Spectra Physics Nd:YAG PIV laser operating at 15 Hz provided illumination for the measurement volume, which consisted of a 40 mm thick region near the sediment bed. The light sheet was formed by a 1000 mm focal length spherical lens located 1190 mm from the sediment bed and a -25 mm focal length cylindrical lens located 755 mm from the sediment bed. Due to constraints in the placement of the laser, an additional 2500 mm spherical lens was needed to propagate the beam to the sheet forming optics, resulting in the sheet waist forming approximately 1500 mm from the last spherical

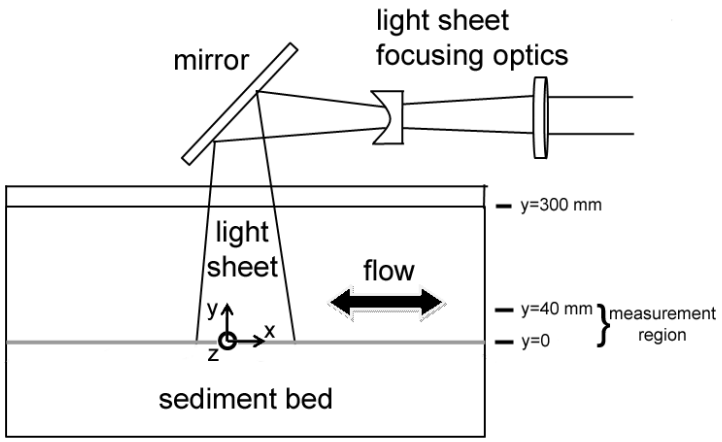

Figure 3.2: *Sketch of experimental environment*

lens element. An 8-bit Kodak ES1.0 camera with 1008x1018 pixel CCD using a 200 mm focal length lens and doubling tube positioned 1320 mm from the measurement volume acquired single exposure image pairs, which were post processed to obtain the velocity and concentration of each phase.

3.2.1 qualification of facility

To qualify and evaluate the performance of the UMD oscillating water channel in the free-stream turbulence level and side wall boundary layer thickness, a series of smooth-wall channel flow measurements were taken and compared to analytical solutions. A false floor was placed inside the test section to mimic the geometry of a channel flow in the test section, see figure 3.3. A series of different free stream sinusoidal velocity profiles and periods were used to examine the boundary layer properties of the channel flow. The velocity in the test section was measured using Laser Doppler Anemometry at various positions along the height of the channel. Figure 3.4 shows the mean stream-wise velocity and RMS velocity in the test section

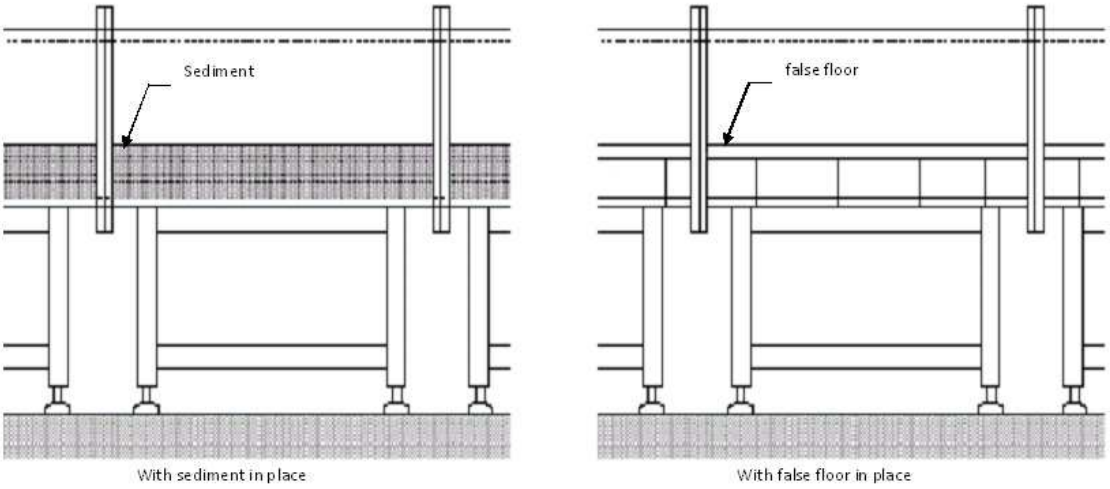

Figure 3.3: *Schematic showing test section with sediment and false floor used to qualify oscillating sediment tunnel performance by examining boundary layer characteristics.*

for a sinusoidal oscillation with maximum velocity of 0.30 m/s and a period of 8 seconds. The Reynolds number based on Stokes length is 452, putting the boundary layer slightly past the laminar regime into the transitional regime. However, the theoretical velocity profiles calculated from Stokes oscillating plate solution agree well with the measured velocity profiles. The RMS in the free stream is 1% of the maximum velocity, indicating that while there is no significant turbulent motion in the center of the channel, it is still a disturbed laminar flow. Also the plot of the span-wise variation of stream-wise velocity was sampled to verify that the flow inside the test section was 2D. The constant velocity profile across the channel indicates that the flow is in fact 2D with no perceptible boundary layer within 5 mm of the wall. Figure 3.5 shows the mean stream-wise velocity and RMS velocity for a maximum free stream velocity of 1.47 m/s and a period of 7 seconds, which

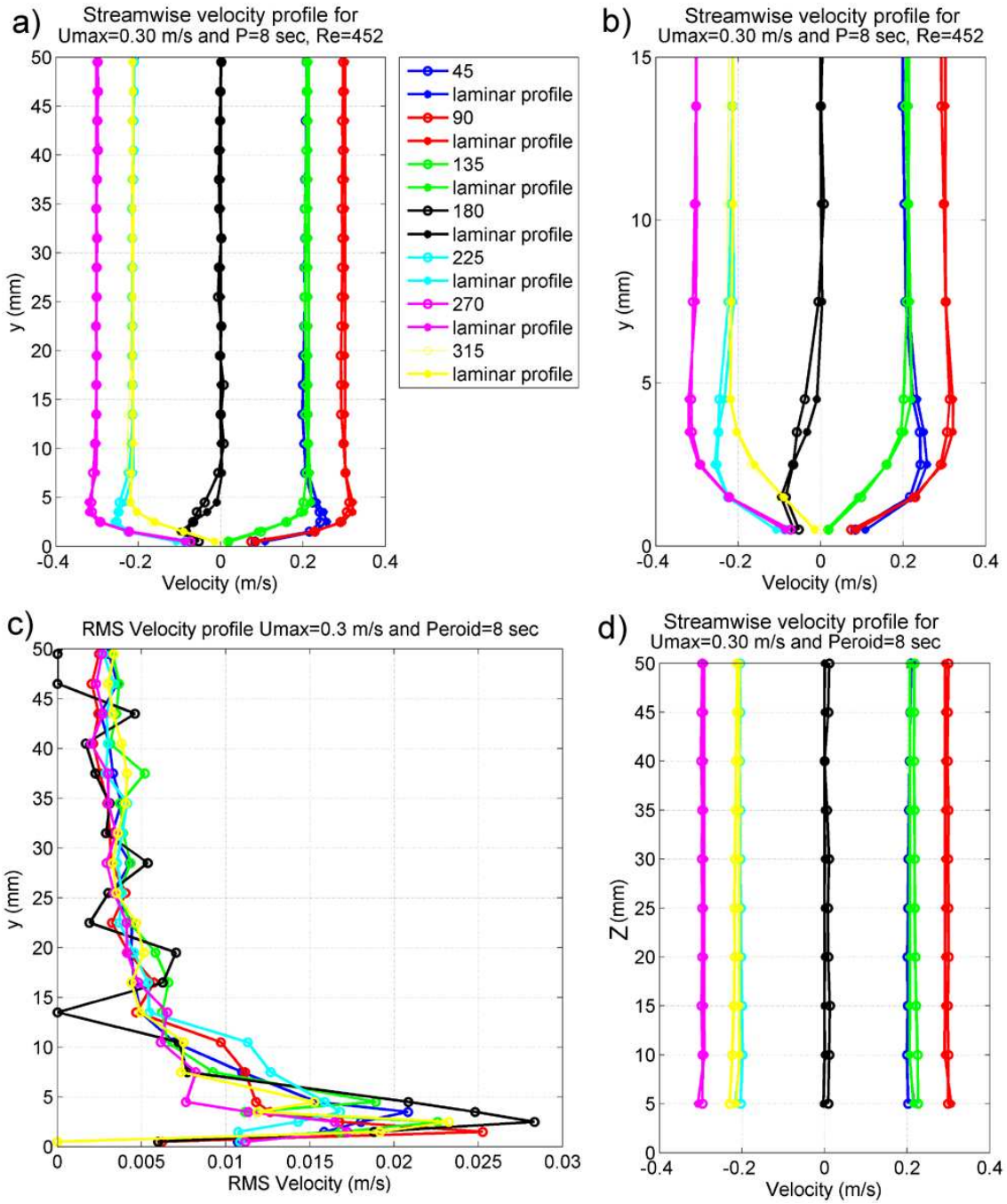

Figure 3.4: *All plots are for sinusoidal oscillations with* $U_{max} = 0.30$ *m/s and period=8 sec. a) wall normal variation of stream-wise velocity plotted with the analytical Stokes oscillating plate solution, b) same as a) but smaller region depicted to show near-wall behavior, c) wall normal variation of stream-wise RMS velocity, and d) span-wise variation of the stream-wise velocity.*

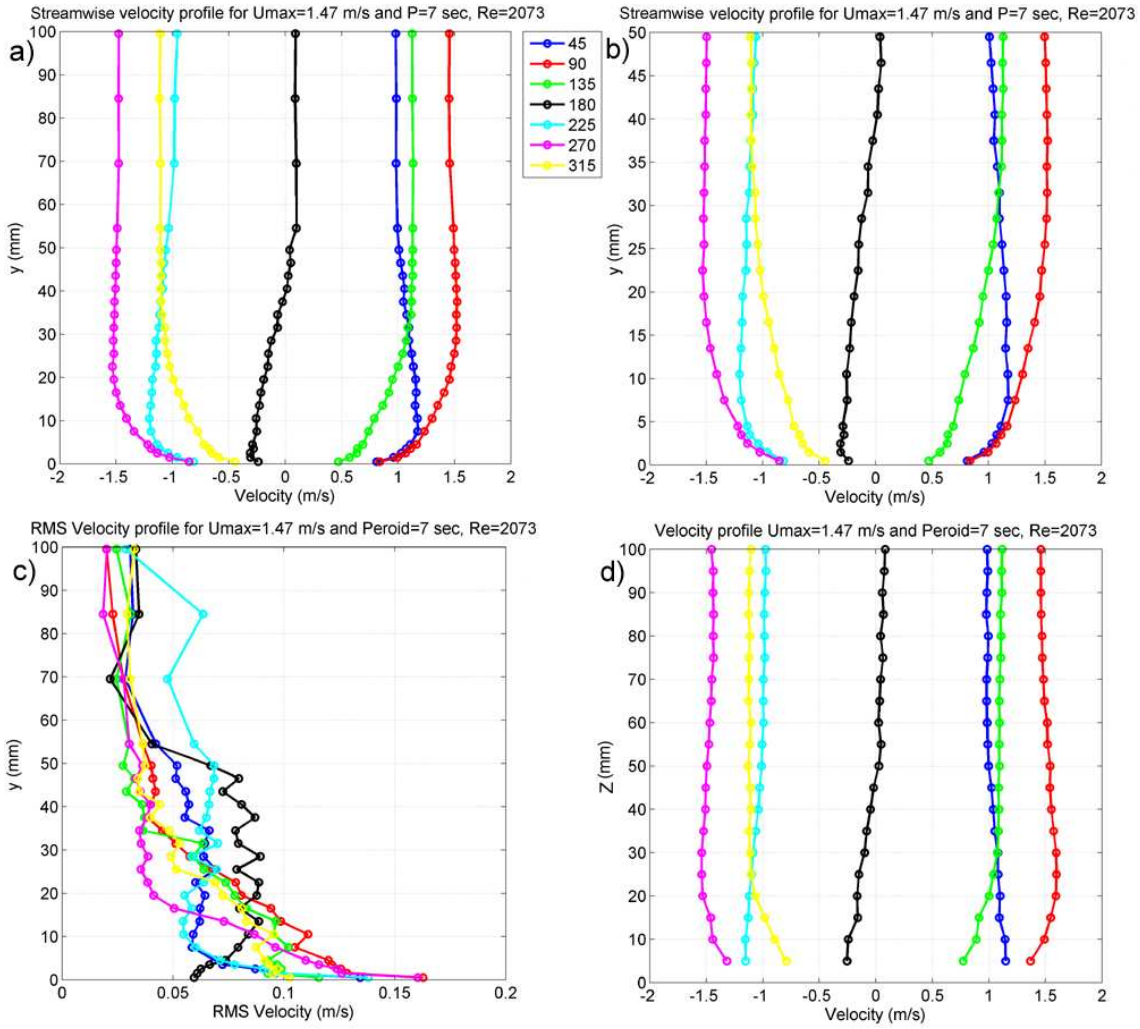

Figure 3.5: *All plots are for sinusoidal oscillations with $U_{max} = 1.47$ m/s and period=7 sec. a) wall normal variation of stream-wise velocity plotted with the analytical Stokes oscillating plate solution, b) same as a) but smaller region depicted to show near-wall behavior, c) wall normal variation of stream-wise RMS velocity, and d) span-wise variation of the stream-wise velocity.*

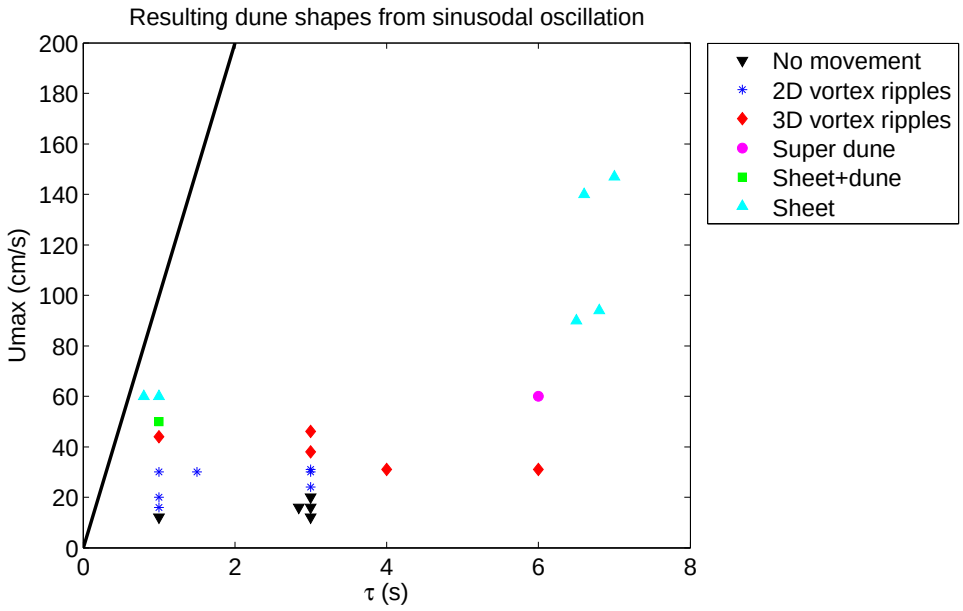

Figure 3.6: *Regime map for UMD oscillating water channel where U_{max} is the maximum velocity for the sinusoidal velocity forcing and τ is the period. The solid black line indicates the regimes possible in the UMD oscillating water channel*

corresponds to a Reynolds number based on Stokes length of 2073. This was the highest Reynolds number case preformed in the test section and resulted in the thickest boundary layers. This case was far into the turbulent boundary layer regime. The velocity outside of the boundary layer is constant in the wall normal and span-wise directions, indicating that the flow is 2D. The thickness of the wall boundary layer is much higher, however, extending approximately 50 mm into the flow.

The false floor was removed and the 240 μm sediment was placed in the test section. The UMD oscillating water tunnel was then programmed to produced sinusoidal oscillations with various maximum free stream velocities.

Figure 3.6 shows the resulting bed conditions for sinusoidal flow oscillation in the UMD oscillating water channel. Each of the cases were started with an initially

planar bed. For the ripple bed cases, the flow was oscillated for several hours to ensure the bed had reached a steady state condition. For $U_{max} = 50$ cm/s and $\tau = 1.0$ second, the bed is transitional between the ripple bed and sheet flow regime. Ripples formed on the sediment bed, but the peaks of the ripples were removed from the sheet like flow near maximum velocity. $U_{max} = 60$ cm/s and $\tau = 6.0$ seconds resulted in a ripple geometry with a wavelength that was greater than twice the width of the tunnel. The tunnel size itself is too small for this condition, which may very likely be due to a strong interaction with the tunnel walls.

To obtain the condition used in the current study, the oscillating water tunnel was programmed to produce sinusoidal oscillations with a maximum free stream velocity of 0.30 m/s and a period (τ) of 3 seconds. Once the ripple profile reached

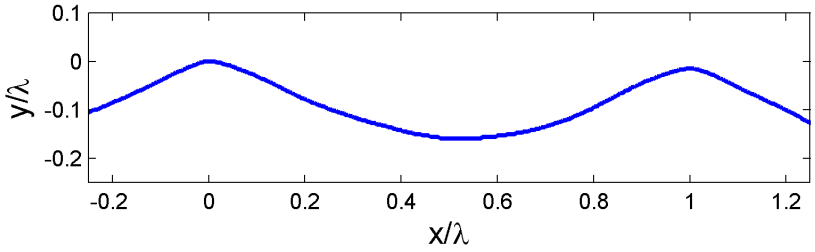

Figure 3.7: *Ripple profile non-dimensionalized by the ripple wavelength (λ)*

steady state, a digital image of the profile was acquired to record the ripple shape (see figure 3.7). In order to validate the geometric sediment ripple shapes that resulted from the sinusoidal oscillations, the resulting ripple wavelength was plotted against previous experiments (see figure 3.8). The oscillating water tunnel sediment bed was leveled flat prior to the experiment. The flow was oscillated for at least 6 hours prior to data acquisition to allow the ripples to form in the tunnel and reach

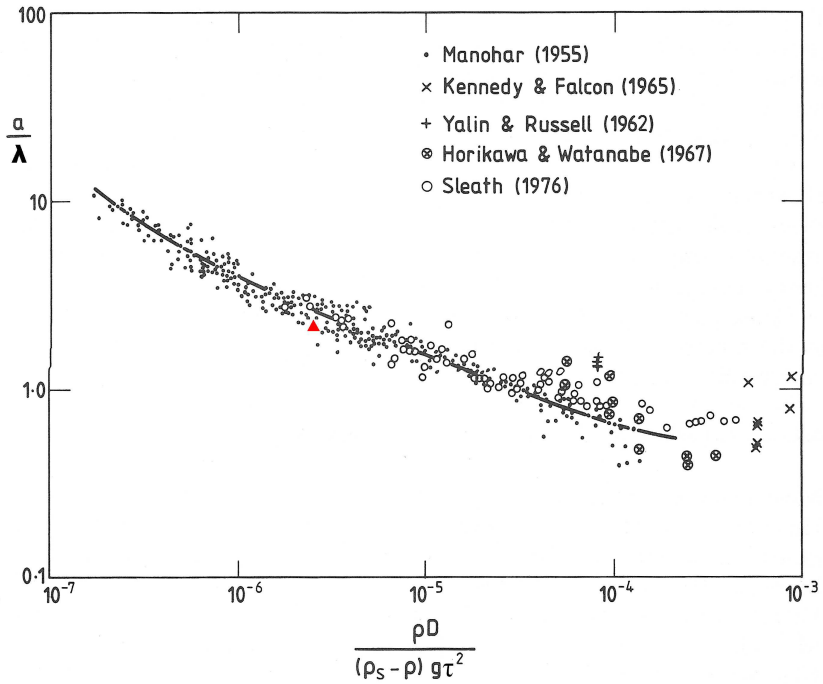

Figure 3.8: *Ripple wavelength (red) plotted with previous experiments in the literature [2]*

a steady state profile. Our observed sediment bed wavelength is in good agreement with previous observed sediment ripple shape geometries.

A single Kodak MegaPlus model ES 1.0 high speed camera with a Spectra-Physics PIV YAG laser were used to measure the two-phase flow field. The maximum sampling rate of the flow field is constrained by the 15 Hz repetition rate of the pulsed YAG laser. The dispersed phase water was seeded with hollow silver-coated glass spheres with a mean diameter of 15 μm, while the sediment bed was composed of 240 μm soda lime glass spheres with a specific gravity of 2.5. Test conditions are shown in Table 3.1.

Using the maximum sampling rate of 15 Hz with a flow oscillation period of 3 seconds allowed capture of 45 different phase angles within the cycle. 500 images

Experimental Test Conditions	
Free stream oscillation amplitude	30 cm/s
Oscillation period (τ)	3 seconds
Reynolds number ($\frac{U_{bulk}^2}{\nu\omega}$)	38,400
Resulting ripple wavelength (λ)	14.5 cm
Resulting ripple height (η)	2.2 cm
Specific gravity of dispersed phase	2.5
Mean Dispersed phase particle sieve size	240 μm
Free stream orbital amplitude to ripple wavelength ratio	2.2

Table 3.1: *Test conditions*

per phase angle were acquired resulting in 22,500 images per location. To minimize the sub-pixel interpolation error of correlating the fluid motion, the optimum tracer particle optical size should be roughly 2 pixels for single-exposer double-frame images using a three point gaussian peak aproximator [37]. This constraint, along with the size of the camera CCD, restricted the maximum field of view of the camera to 2 cm. To capture the entire flow field, experimental data was taken at various locations and joined together to obtain continuous data over most of the ripple wavelength. Figure 3.9 shows the approximate locations of regions sampled by the camera indicated by the red regions. Because the flow is symmetric in time, data located 180 degrees out of phase can be used to obtain the flow field on the opposite side of the valley at locations indicated by the green regions by mirroring the data and changing the

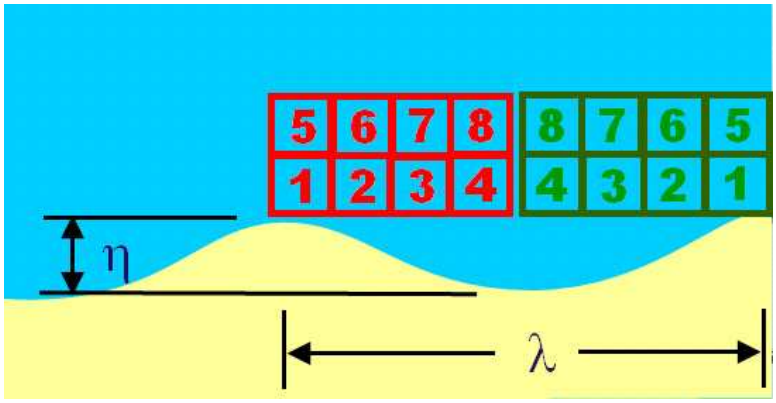

Figure 3.9: *Approximate Graphical representation of imaged two-phase PIV regions in red and regions that can be obtain using symmetry of the flow in green.*

sign of the stream wise velocity.

Due to the fact that the ripples are formed by the flow from the sediment, they are free to move and migrate slightly during data acquisition. Although nominally steady conditions are reached for the test conditions, some small ripple migration during the experiment is uncontrollable, which poses a difficulty for acquiring constant and repeatable data. To minimize this problem, PIV images were obtained at a fixed location during a 5 minute interval. If ripple migration was larger than ± 4 mm (approximately 3% of the ripple wavelength) over 5 minutes, the data set was rejected and acquired again. The measurement location was taken as the average between the the position at the beginning of data acquisition and the end of each set.

3.3 Introduction to Experimental technique

In many multi-phase flows, the concentration and transport of a dispersed phase can play a important role in the flow. Typically the governing equations

describing conservation of mass, momentum, and energy for these types of flows are formulated on a unit volume basis, which requires an accurate measure of the concentration of each phase. In addition, momentum transport between phases in dispersed multi-phase flows is an important topic in many industrial and environmental processes, such as pneumatic transport of granular material and sediment transport on the continental shelf. These type of flows are often described using a coupled Eularian-Eularian two-fluid model, where each phase is treated as a coexisting fluid represented with its own governing equation while interfacial transport terms are used to describe mass, momentum, and energy exchanges between the phases. These types of flows are often difficult to simulate and require models to accurately represent the complex interaction between the phases. To experimentally investigate the terms in the these governing equations requires a technique that can simultaneously measure the concentration and velocity of each phase.

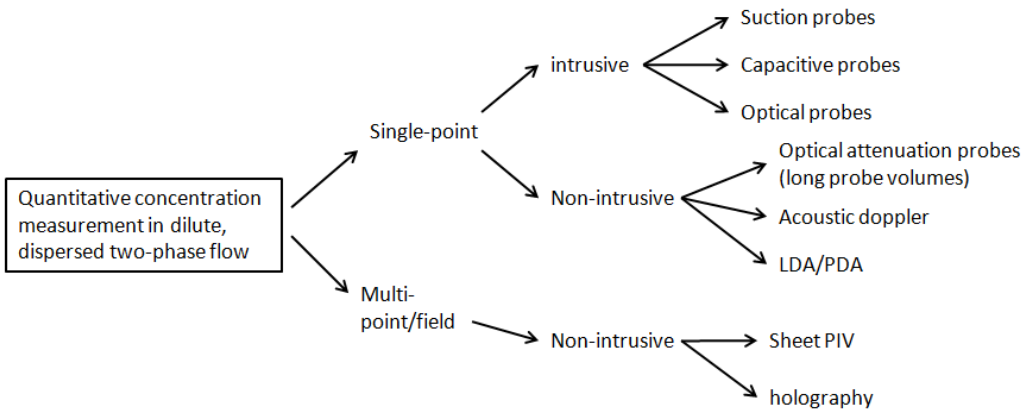

Figure 3.10: *Schematic of experimental measurement techniques used in dilute flow*

To put the current work in context, a brief overview of existing techniques is warranted. In general, particle concentration measurement techniques for dilute multi-phase flows can be categorized as either single-point or multi-point (whole field) methods, and further divided into intrusive or non-intrusive measurements, (see figure 3.10). Intrusive single-point measurements include methods such as suction probes, capacitive probes, and optical probes, all of which require a physical probe to be inserted into the local proximity of the sampling volume. While the probes can be optimized to be minimally invasive, some disturbance to the flow will always remain. Suction probes operate by extracting a known volume of fluid from the flow and physically measuring the volume or mass of each phase. The difficulty with suction probes is that the collection efficiency (and hence the effective sampling volume) is a function of the velocity difference between the ambient flow and the suction orifice as well as the physical properties of the particles, such as size, shape and density. To cause minimal disturbance to the flow, the abient velocity is matched to the suction velocity of the probe. Even for very closely matched velocities, suction probes often have an 80% collection efficiency [19], which is sensitive to velocity matching. In unsteady flows it is often difficult to maintain a similar suction velocity to the surrounding fluid, which can introduce significant measurement bias. Bosman et al. (1987) found that the collection efficiency becomes only a function of grain size when the suction velocity is three times larger than the flow velocity. However the flow is more significantly disturbed in the measurement region, making simultaneous velocity measurements of each phase difficult. Capacitance probes obtain the concentration by measuring the capacitance of a local region and

comparing to a reference calibration. The challenge with this method is that the capacitance of the volume is a function of temperature, moisture, humidity, material bulk density, particle size, and the electrostatic charge of the particles [39]. Optical probes rely on measuring the transmissive, reflective or refractive properties of the measurement volume and comparing to a know calibration to determine the concentration [40]. Probes can be used in a forward or backscatter mode depending on the optical properties of the material being measured and if the separation distance between the transmitter and receiver is large, the probe can be non-intrusive [41]. The relationship between the light scattering and concentration must be obtained through careful calibration to relate the light attenuation to the concentration [42]. For optical probes, the size of the probe volume can be non-consistent and difficult to know directly from complex scattering in the volume [41].

Non-intrusive concentration measurement techniques such as acoustic doppler, laser doppler (LDA), and phase doppler (PDA) have the advantage of obtaining velocity as well was concentration measurements at a single point. Acoustic probes measure the backscatter of acoustic waves from the measurement region. Detailed understanding of how acoustic waves interact with sediment is required and has been investigated by Sheng and Hey (1988) [43] and Thorne and Campbell (1992) [44]. One difficulty in using acoustic probes is the probe is sensitive to both concentration and particle size. However, success was made at separating the effects of concentration and particle size, but at the expense of accuracy [45]. LDA and PDA techniques work on the principle of the single particle counting within a optical sampling volume [46] [47]. However, they also require careful correction as the

effective sampling volume is a strong function of the particle size [48] [49]. While single point measurements, such as laser doppler, phase doppler, and acoustic doppler anemometry provide important detailed information about mean and fluctuation quantities of the flow, they cannot provide full field instantaneous velocity measurements of each phase. For many experiments, a full field measurement technique is preferred because it allows the researcher to observe the instantaneous structure of the flow. Quantitative imaging techniques such as sheet PIV and holographic PIV are multi-point measurement techniques that allow for simultaneous velocity and concentration measurements while being non-intrusive to the flow and reducing the difficulty associated with interpreting flow structure from point measurements. The difficulty with measuring concentration using imaging methods, is in determining the effective measurement volume.

Single phase PIV is a relatively simple technique and the basics of the technique are discussed in detail in Westerweel [50] and Adrian [51], but the extension of PIV to multi-phase flows requires careful attention. In traditional single-phase PIV, a cross-correlation is performed on the images to obtain the mean displacement of particles within a small sampling region. When a cross-correlation is performed on a two-phase image, the cross-correlation in the region of the dispersed phase particles is contaminated by the displacement information of the dispersed phase (referred to as cross-talk), making extraction of the carrier phase velocity non-trivial. Therefore to obtain carrier phase information in the region of the dispersed phase particles and eliminate biased velocity measurements due to the presence of another phase, the two phases must be distinguished during the sampling and evaluation procedure.

Phase separation has been carried out using several different approaches. One of the first two-phase PIV techniques used two cameras with fluorescent tracers marking a single phase [52] [53]. Through the use of optical wavelength filters, one camera captures the continuous phase, while the other records the dispersed phase. This technique works well, but requires large illumination intensity, multiple cameras, and possibly expensive fluorescent particles. Delnoij et al. [54] developed a single camera technique that relies on significant velocity differences between the phases to produce a bi-model correlation map. *A-priori* knowledge of the flow may be required to reliably identify which correlation peak belongs to a given phase. Researchers have also used image processing filters to discriminate phases during post processing when a significant difference exist between the phases [55]. Kiger and Pan (2000) developed a single camera two-phase PIV technique that artificially separates the phases using a post processing technique and applied it to study a turbulent channel flow [56]. Khalitov and Longmire (2002) developed phase discrimination criteria based on the size and brightness of objects which was used to identified and separate the phases in the experimental images [55]. Lindken and Merzkirch (2002) combined sheet PIV with fluorescent tracer particles, shadowgraphy, and a digital masking technique to simultaneously measure the velocity of each phase with only a single camera [57]. This thesis will present a hybrid of the technique used by Kiger and Pan (2000) along with the phase discrimination techniques developed by Khalitov and Longmire (2002) and quantification of the local detection volume used in the presence of reflective sediment beds, which adds significant complexities to the optical measurement.

There are several considerations that must be examined to understand how the measurement of concentration is affected by the measurement environment. Properties of the light sheet such as variable sheet width due to focusing, the profile of the light sheet, attenuation of the sheet from tracer particles, and scattered light from the measurement environment can influence the light scattered and collected from the dispersed phase particles, which can ultimately play a role in determining the effective measurement volume. Each of these influences on the measurement must be understood to properly employ two-phase PIV with a high level of accuracy and to be aware of the limitations and situations where this technique is no longer reliable. Identification and counting of dispersed phase sediment particles is relatively simple, however determining the effective measurement volume is not always straightforward. In this context, a description of our specific method to separate and identify the dispersed phase will first be given, as this is relevant to understand how the effective sampling volume is determined, followed by a more general discussion of the source of errors that occur in sheet illumination methods. This is finally summarized with a method to correct for the discussed bias errors to provide a quantifiable estimate of the concentration.

3.4 Image processing and dispersed phase identification

The phases must be separated before the cross-correlation is performed to obtain carrier phase information in the region of the dispersed phase particles and eliminate velocity measurement cross talk between the phases. If there is a rel-

atively large disparity in size between the dispersed phase and the carrier phase tracer particles, the phase images can be separated by using an appropriately sized median filter [56]. Figure 3.11 displays an overview of the phase separation and velocity measurement process. The process starts with the application of the median

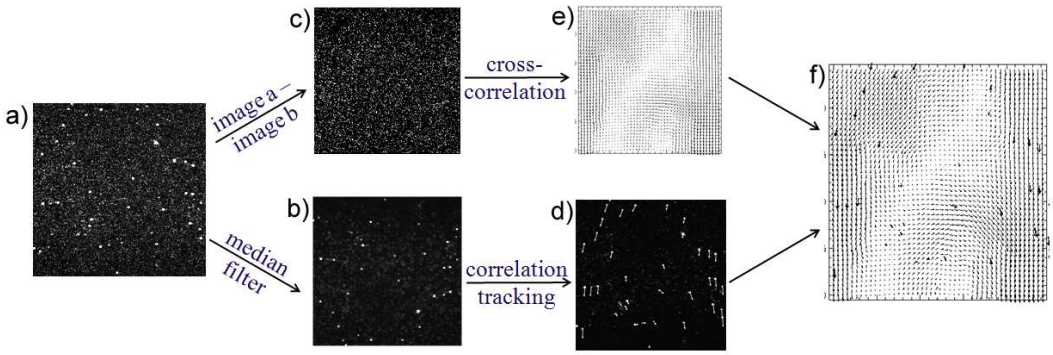

Figure 3.11: *Schematic of image processing: (a) the original 2 phase PIV image, (b) dispersed phase only image constructed from applying median filter to original image, (c) carrier phase tracer particles only image constructed from subtracting image b from image a, (d) velocity field for dispersed phase, (e) velocity field for carrier phase, (f)*

filter, which results in an image containing only the large dispersed phase particles, figure 3.11b. The dispersed phase image is subtracted from the original two-phase image to obtain a carrier phase tracer particle image, (see figure 3.11c). Once the phases are separated, the carrier phase images are suitable for velocity measurement. For dilute flows, the carrier phase images are of sufficient image density to allow reliable processing using a cross-correlation routine to extract fluid tracer particle displacements. In contrast, the relatively low volume fraction of the dispersed phase particles requires that each dispersed phase particle be accurately identified so

that the dispersed phase velocity is extracted only where dispersed phase particles are present via a discrete particle tracking method. Once a dispersed phase particle is identified, a cross-correlation is applied to extract each particles displacement. A three point gaussian is fit to the correlation map to obtain sub-pixel displacement information for each particle.

3.4.1 Dispersed Phase particle identification

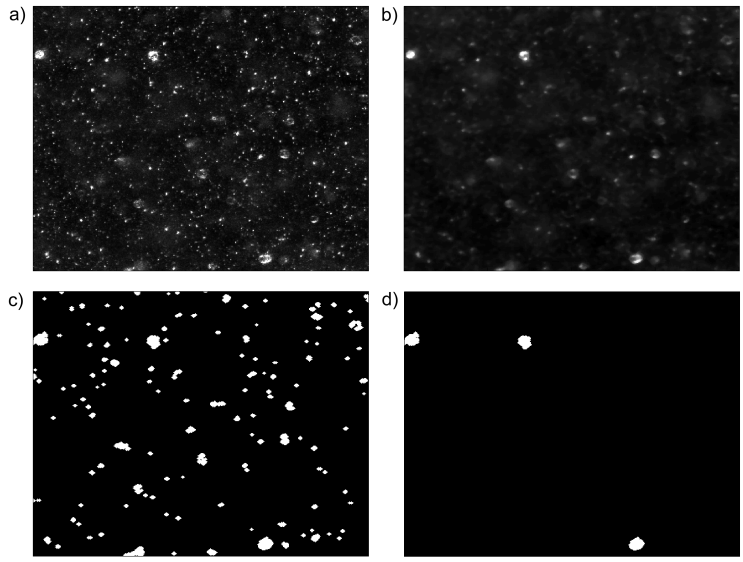

Figure 3.12: *Particle discrimination sequence from a 10mmx10mm region of a single image. (a) Unmodified two-phase PIV image, (b) image after the median filter is applied, (c) all continuous objects identified, and (d) objects identified as particles based on size and brightness*

Figure 3.12 shows the particle identification process in sequence. Once the images are median filtered, only dispersed phase particles remain in the image (figure 3.12b). Khalitov and Longmire (2002) developed a flexible and robust phase discrimination algorithm that uses second order intensity gradients to identify objects

with a subsequent size and brightness criteria specified to discriminate the dispersed phase objects. A threshold is applied to the image which marks any pixel below the threshold as the image background. After the threshold is applied, pixels that obey the following criteria are marked [55]:

$$\frac{\partial^2(ln(I_p))}{\partial x_i^2} < 0 \; or \; I > I_{saturated} \tag{3.1}$$

where where I_p is the pixel intensity and $I_{saturated}$ is the effective saturation threshold, (taken for our conditions to be $I_{saturated} = 230$). Contiguous pixels that obey the criteria in equation 3.1 are then identified as a single particle and marked in a binary pixel identification matrix. Because the median filter removes the outer edges of the dispersed phase particles, the binary pixel identification matrix id dilated by half the size of the median filter. A contiguous blob identifying algorithm is then applied to mark contiguous pixels above the noise threshold as a single identified particle. However, not all particles identified in the image are suitable for accurate velocity measurements. Figure 3.13 shows a sample of various objects identified from a near-bed two-phase PIV image. Particles on the edges of the light sheet (normal the the sheet) and particles weakly illuminated by diffusively scattered light outside of the light sheet are not reliable for obtaining velocity and concentration information. In order to prevent validation of spurious objects, a discrimination algorithm must be used to identify particles that can be tracked with large certainty and reject other unqualified objects. Nominally, discrimination of tracer or dispersed phase can be readily distinguished by clear values of size and brightness (as done by [55]), but quantification of the effective detection volume for a single particle requires more

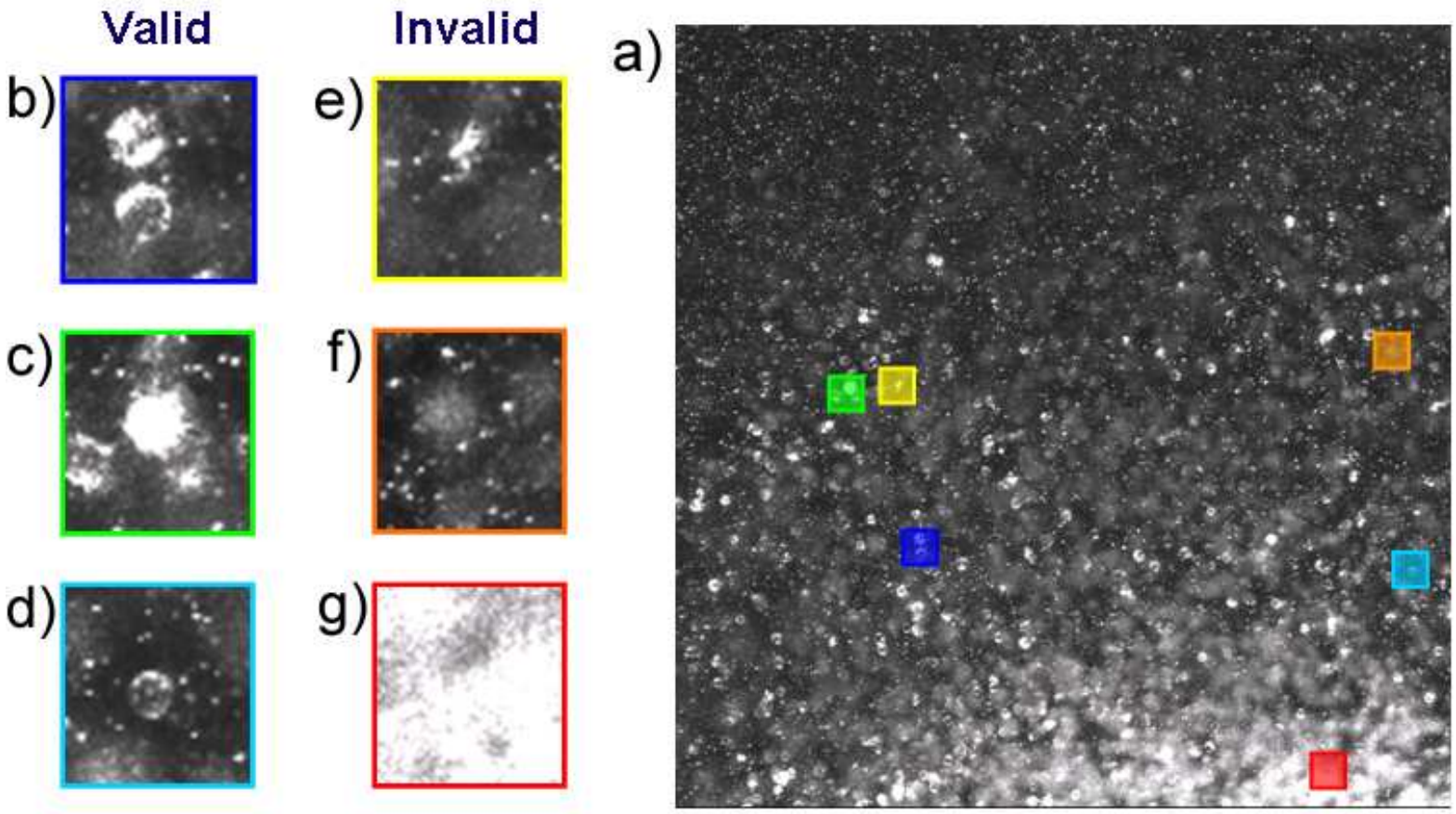

Figure 3.13: *Two-phase PIV image showing particles that should be identified as valid and invalid samples of dispersed phase. (a) raw image, (b)(c)(d) valid images, invalid due to (e) blocked particle image, (f) particle outside of light sheet but illuminated by bed reflections, and (g) excessive particle concentration preventing identification of discrete objects.*

careful consideration, as discussed in the next section.

3.5 Quantification of measurement errors

The uncertainty in determining the tracer particle velocity for single-exposure double-frame PIV images is well characterized. Detailed studies have shown that using the optimal particle image diameter of 2 pixels for single-exposure double-frame images with a 32 by 32 pixel window and three point gaussian sub-pixel interpolation results in an idealized uncertainty of ± 0.025 pixels or ± 0.11 cm/s [37]. Other factors such as seeding density, characteristics of the camera CCD/electronics, optical considerations such as diffraction limits ,etc. can also play a role in the uncertainty of the measurement not captured in an idealized analysis. Typical practical uncertainty values are taken to be ± 0.05 pixels or ± 0.22 cm/s for this experiment.

To determine the uncertainty in the dispersed phase velocity, images of particles in the flow were artificially offset a known distance and the uncertainty in the displacement estimation was obtained by comparing the displacement algorithm output and the known displacement. To complete this estimate, an ensemble of particle images were extracted from the experimental test data. A second shift image of the same particle was artificially created using bilinear interpolation to obtain a known sub-pixel offset displacement. This process was performed with 1000 random shifts between a 0 and 1 pixel offset, and the resulting error in displacement was recorded. Figure 3.14 shows the sub-pixel interpolation error from the 50,000

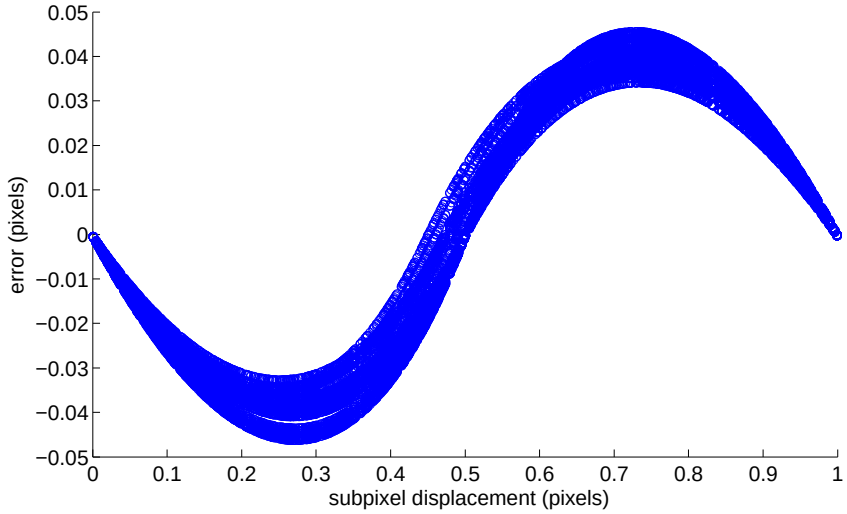

Figure 3.14: *Dispersed phase sub-pixel interpolation error from artificially displacing 50 particles shifted 1000 times between a 0 and 1 pixel offset. Each of the 50,000 data points is represented by blue circle.*

artificial displacements. The rms uncertainty in the dispersed phase displacement will be taken to be ±0.04 pixels or ±0.18 cm/s. This does not account for any change in appearance from particle movement normal to the sheet, so this estimate is a lower bound for the particle displacement error.

Through detailed analysis described in chapter 4, the uncertainty in measuring the concentration of dispersed phase volume fraction was determined to be ±12%

Chapter 4

Using light sheet technque for concentration measurements

4.1 Single particle light scattering

In order to understand how to reliably identify the sediment particles, we must first understand how environmental factors such as light sheet attenuation from tracer particles, illumination from multiple scattering, and the presence of a reflective sediment bed affects the light scattering characteristics of sediment particles and how sensitive these effects are to measuring the concentration of sediment particles. Assuming spherical scatting particles, the total light incident upon a particle can be formulated as a sum of 3 sources:

$$I_{detector} = \frac{1}{r_d^2}[\int I_l(\theta_l)d\theta_l + \int I_s(\theta_s)d\theta_s + \int I_r(\theta_r)d\theta_r] \tag{4.1}$$

where $I_{detector}$ is the total amount of incident light received by the detector from a particle, d is the diameter of the particle, r_d is the distance from the particle to the detector, I_l is the amount of incident light directly from the light sheet, I_s is the amount of incident light upon a particle scattered from tracer and dispersed particles in the flow, I_r is the amount of light illuminating a particle that was scattered from the wall boundary (or sediment bed in our example), s is the scattering coefficient of the dispersed phase, θ_l is the angle between the incident light sheet illumination and the detector, θ_s is the angle between the incident light scattered from tracer

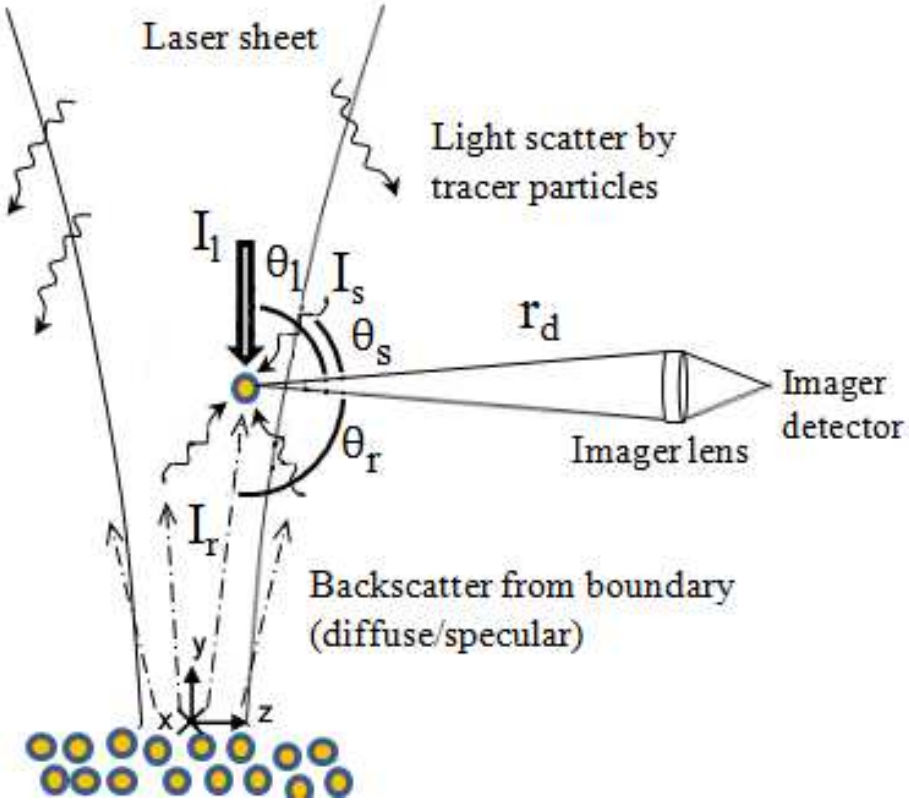

Figure 4.1: *Incident light source on a particle*

particles and the detector, and θ_r is the angle between the incident light from the sediment bed and the detector. For non-spherical particles, expression 4.1 would also depend on the particle orientation, which is not considered in the current discussion. Particles in the measurement volume not detected because of multiple scattering from other dispersed phase particles should be rare for the relatively dilute volume fractions considered and the small observation depth (10 cm) where other particles are present.

The amount of incident light on a single particle directly from the light sheet, I_l, is dependent on the optics used to form the sheet, the beam profile of the light sheet, and any reduction in intensity due to light scattering before the sheet is incident upon the particle. In our specific example, the changes in I_l as a function of beam propagation distance (see figure 3.2 for coordinate system) was directly measured by the beam profile camera at discrete locations along its length. Measurement were made using four different concentrations of tracer particles mixed with water in a test chamber (denoted by C_i, with i=0, 1, 2, 3). The clean water case, C_0, consisted of tap water filtered to less then 1 micron, while C_3 corresponded to a concentration of tracer particles found to be suitable for PIV under our conditions. The intermediate cases of C_1 and C_2 correspond to concentration of $0.25C_3$ and $0.5C_3$ respectfully.

For quantification of the light sheet profiles, a beam profile camera was used. Images of the profile were obtained by reflecting the sheet outside the tank at different positions along its length, with the camera placed against the tank wall. This still necessitated a propagation of approximately 50 mm in open air to reach the

camera's detector. The effective position of the profile camera was calculated based on its equivalent propagation in water alone, although the difference in scattering the last 50 mm was not accounted for. Figure 4.2 a) and f) show filled contour plots of the normalized laser sheet intensity for C_0 and C_3 cases as a function of propagation direction (y) and cross-sheet position (z). Note that the light sheet enters the scattering medium at y=300mm, and only the final 120mm prior to the sediment bed are shown. The green and red lines mark the $1/e$ and $1/(e^2)$ sheet widths respectively (based on the mean of the sheet intensity in the center top hat portion of the sheet). The profiles shown in figure 4.2b) through d) and g) through i) are the intensity profiles at the locations y=0, 60, and 120mm, respectfully (indicated by the black lines in figure 4.2 a) and f)) normalized by the mean sheet intensity in the top hat portion of the sheet at 120 mm (I_{mC0} and I_{mC3} respectfully). Finally, the profiles in figure 4.2 e) and j) are the same profiles normalized by their local mean intensity and $1/e$ sheet width. From figure 4.2f, it is readily apparent that the tracer particles strongly scatter light throughout the region, causing the intensity of the light sheet to decrease even as its being focused. In the absence of particles (figure 4.2b)), however, the largest intensity is closest to the focal point, as expected. In figure 4.2b) at 120 mm above the sediment bed, outside of the $1/(e)$ light sheet width the light, the measured light intensity is negligible. However, the increased light scattering from the tracer particles in figure 4.2g at the same location, causes the intensity outside of the $1/(e)$ light sheet width to remain significantly above zero (20-25% of the mean light sheet intensity) which is above the $1/(e^2)$ intensity and therefore is not a good indicator of the sheet width. For the sake of discussion, we

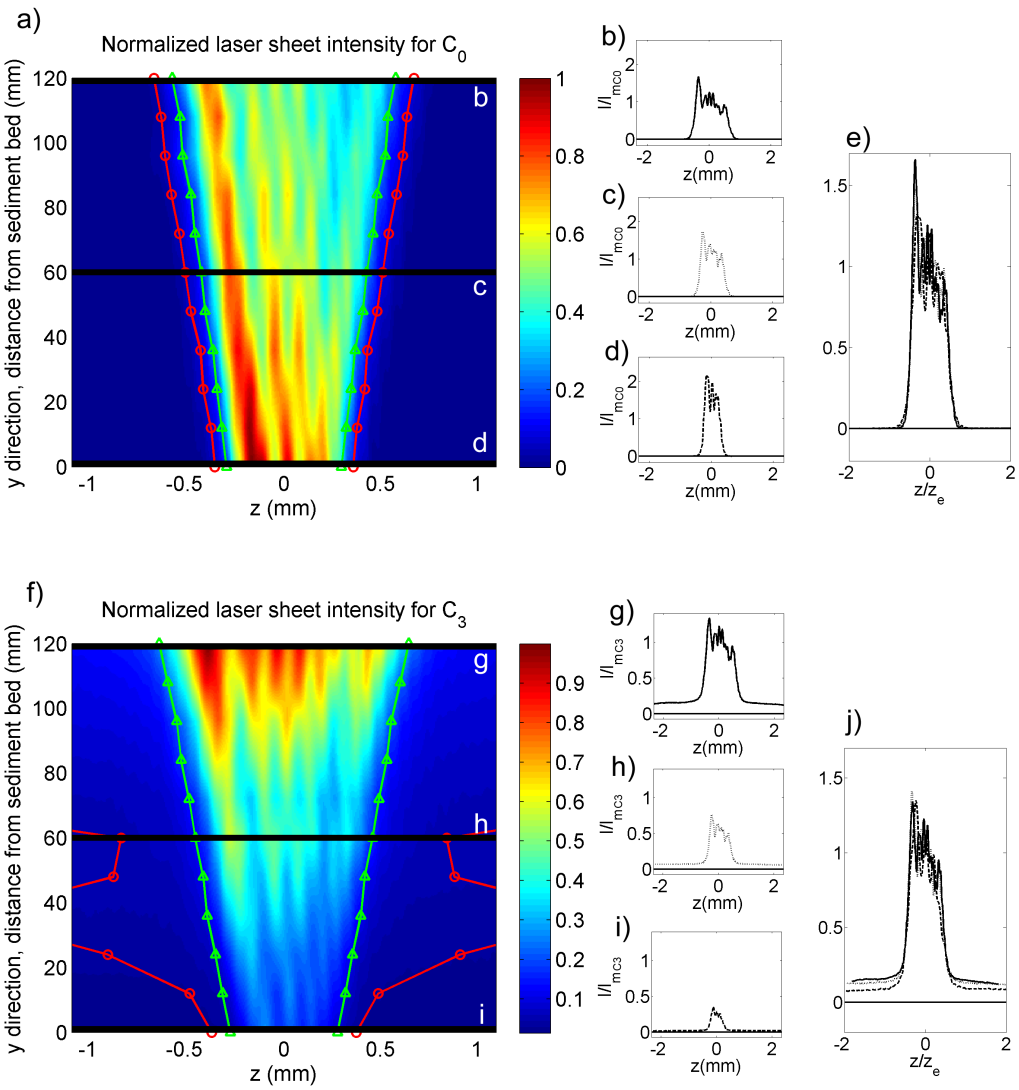

Figure 4.2: *Normalized laser sheet intensity for a) concentration C_0 and f) concentration C_3. $1/e$ sheet width (green lines with triangles) and $1/(e^2)$ (red lines with circles) based on the mean sheet intensity in the center/top hat portion of the sheet. Profiles b) through d) and g) through i) are intensity profile plots at 120 mm, 60 mm, and 0 mm respectfully from a) and f). The profiles in e) are the intensity profiles in b) through d) normalized by the mean intensity in the center of the sheet and the $1/e$ sheet width. The profiles in j) are the intensity profiles in g) through i) normalized by by the mean intensity in the center of the sheet and the $1/e$ sheet width.*

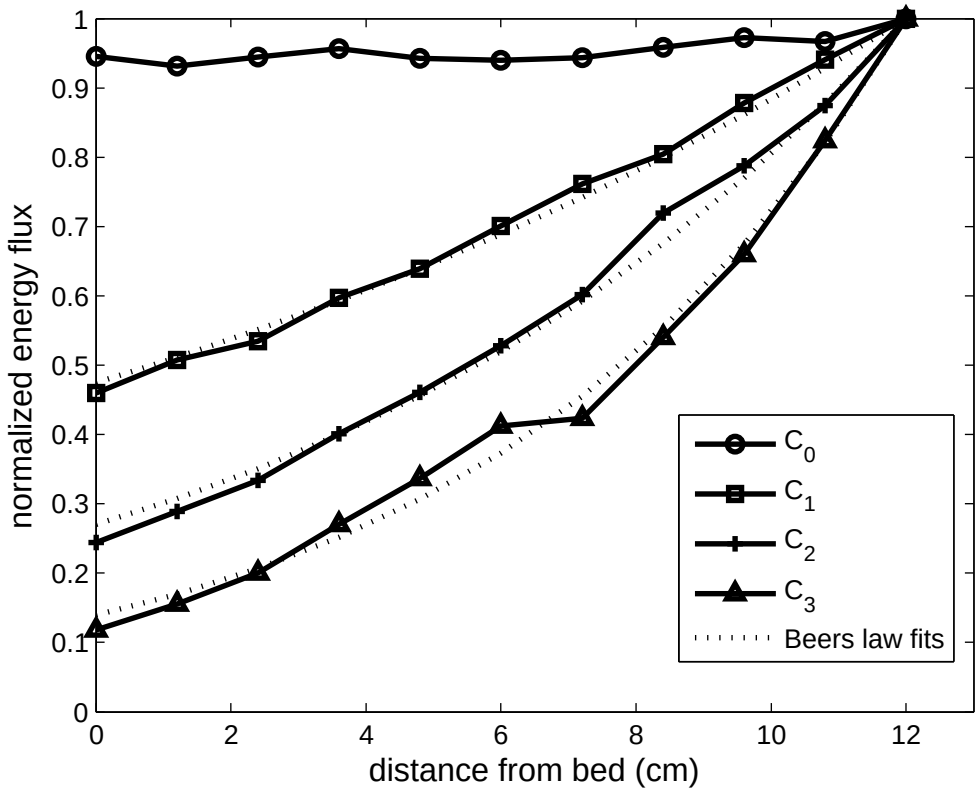

Figure 4.3: *Normalized energy flux vs distance from the sediment bed for* $C_0, C_1, C_2,$ *and* C_3 *concentrations of tracer particles, and Beers law fits to the energy flux curves*

will take the light within the $1/(e)$ region to be the light sheet, and that outside of this region to be scattered light, even though in reality a significant fraction of the light within the "sheet" is composed of scattered light. Comparing the sheet width measurements between the two cases reveals that the light scattered from the tracer particles increases the effective width of the light sheet.

Figure 4.3 shows the laser intensity profiles integrated across the $1/(e)$ sheet width and normalized by the energy flux at 120 mm above the bed for $C_0, C_1, C_2,$ and C_3. For dilute scattering, the laser sheet profile is expected to follow Beer's law

$(c\sigma)_1$	$.0062\frac{1}{mm}$
$(c\sigma)_2$	$.0109\frac{1}{mm}$
$(c\sigma)_3$	$.0164\frac{1}{mm}$

Table 4.1: *concentration multiplied by the absorption coefficient for Beer's law of $C_1, C_2,$ and C_3 respectively*

and least squared fits to energy flux as a function of y are shown for C_1, C_2, and C_3 in figure 4.3. Beer's law is described by:

$$\frac{I}{I_0} = exp(-c\sigma L) \tag{4.2}$$

where I in the normalized energy flux and location y, I_0 is the energy flux into the domain, c is the concentration of scattering particles, σ is the absorption coefficient, and L is the length of propagation. The absorption coefficients for figure 4.3 are summarized in table 4.1. The lack of proportionality of the effect attenuation coefficients to the concentration is most likely due to the finite aperture of the beam profile camera, and hence the measured "beam" contains a significant fraction of scattered light as mentioned above.

The importance of this figures 4.2 and 4.3 are that they illustrate the potential influence scattering can have, depending on the size of the measurement region and the concentration of the tracer particles. If the measurement region is large enough, such that the attenuation is significant and the domain is considered optically thick, then the intensity of light incident upon the sediment particles from the light sheet (I_l) will be a function of their distance along the beam path. If this spatial vari-

ability is not properly accounted for, it can introduce a bias in the detectability of the dispersed phase, by virtue of the fact that nearly all dispersed phase imaging methods rely on a threshold operation to discriminate the dispersed phase from the background at some point in the process. For example, if the measurement region consisted of the region $0 < y < 120$ mm, even the lowest concentration would present a significant bias as the light intensity changes by 200% over this region. On the other hand, a significantly small region ($\delta y < 10$ mm) at the highest concentration would result in only a 15% change in illumination intensity over the measurement region, which may not be readily noticed.

The second source term in equation 4.2 represents the amount of incident light that is re-scattered from other particles in the flow. As seen previously in figure 4.2b at 120 mm above the sediment bed, the light scattered from tracer particles can produce a measurable illumination outside the nominal $1/(e)$ sheet width. Since this illumination results directly from the light removed from the sheet by scattering, it will be important for optically thick systems ($c\sigma L \sim O[1]$). Light scattering from other dispersed particles can be significant when suspended in large concentrations, however, the ability to optically identify individual particles becomes difficult before multiple scattering from dispersed phase particles becomes significant.

The last term in equation 4.2, I_r, is the amount of light illuminating a particle that was scattered from the sediment bed. When the laser light from the sheet strikes the sediment bed, it undergoes multiple scattering in an optically dense media and is reflected back into the measurement volume as "coherent backscatter", which can be treated as a secondary illumination source. The reflected light from the sediment

bed is not simply specular or purely diffuse reflection, but a complex arrangement that is challenging to characterize [58]. The reflected light, I_r, can be significant near the sediment bed, illuminating particles outside of the light sheet and making characterization of the measurement volume more difficult. Direct characterization of these last two features was not possible in our experiment, instead we will examine their net combined influence through a calibration procedure discussed in the next section.

4.2 Calibration procedure for effective detection volume

In order to directly examine the effect of light scattered from the sediment bed on the sediment particles suspended in the flow, sediment particles at known concentrations were placed in a dense hydro-polymer gel (Johnson & Johnson, Purell Instant hand sanitizer) which kept the particle fixed in suspension. The specific hydro-polymer gel was chosen because it has a similar index of refraction (n=1.35) to the carrier phase fluid (water, 1.33), which is commonly used in many solid-liquid experiments. Sediment particles were mixed in the hydro-polymer gel in various volume fractions [.0001, .0003, .0005, and .0008] and placed in a rectangular glass test cell (75 mm x 25 mm x 25 mm). Uncertainly in "known" concentration due to non-uniform mixing and inability to make measurement near the walls of the test cell were estimated to influence the concentration by $\pm 10\%$. To quantify how light scattering from particles changes as a function of position in the light sheet, the mixtures were traversed through the depth of the light sheet in 100 micron increments while

imaged with the light sheet and imaging camera kept fixed. To keep the scattering light conditions similar, the test cell was immersed in a tank maintained with the typical tracer particle concentration used $(c\sigma)_3$, and positioned such that the sheet propagated though the same distance as in the experiments. Using these images in combination with the dispersed phase discrimination procedure, provides a direct measure of how the effective measurement volume is related to the position in the light sheet. This detailed information provides the effective measurement volume for various particle identification parameters and allows validation of the concentration measurements. Particle images were acquired by first traversing the test cell over the sediment bed, then traversed a second time with a light absorbing media placed between the test cell and the sediment bed. Any changes in light scattering are a direct result of the incident light upon a particle from the reflective sediment bed, I_r. Figure 4.4 plots iso-contours of a particle brightness as a function of z for a typical particle without the reflective sediment bed. As expected, the particle has the largest brightness in the center of the light sheet (z=0). The particle appears as two bright spots, one spot on the top of the particle and one on the bottom of the particle. Similar results were found by [56] in a turbulent two-phase channel flow. The top spot is due to reflections off of the particles top surface as well as scattering from optical inhomogeneities within the particle, and the bottom spot is most likely due to second order refraction and the strongly non-uniform illumination for these size particles. In the center of the light sheet $z = 0$ mm, light scattered from the center of the particle is visible on the detector along with the two bright spots. However, when $(\mid z_o \mid > 1$ mm where z_o is the location of a particle, the intensity of light scat-

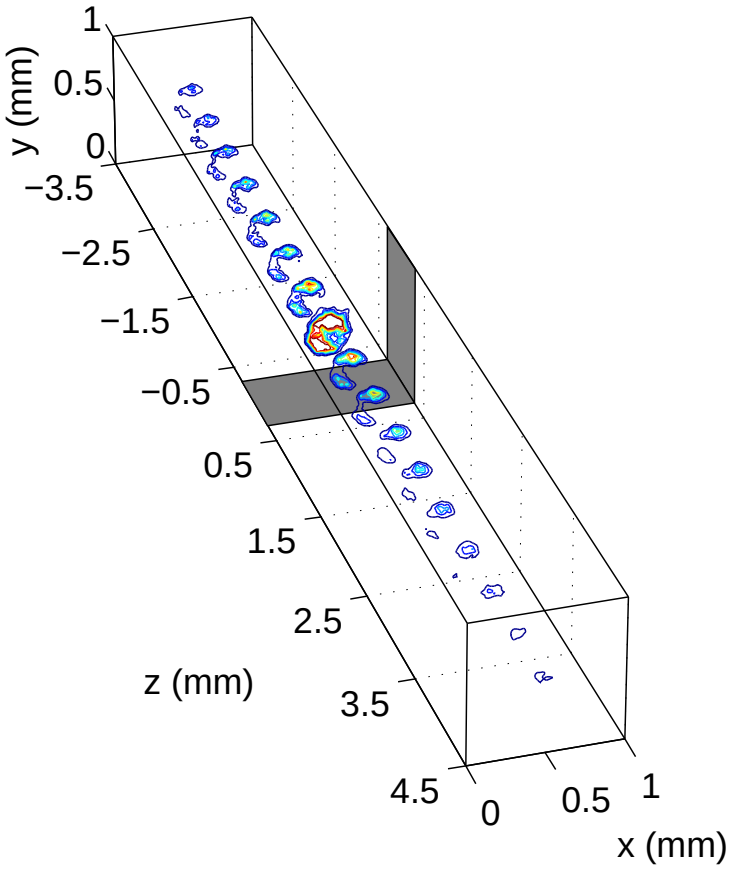

Figure 4.4: *Iso-contours of particle brightness vs z for a typical single particle. Nominal light sheet position and* $1/e$ *thickness denoted by the grey band*

tered from the particle diminishes and only the two bright spots remain. Care must be taken to identify these smaller bright spots as a single particle if particles are to be identified in this region. The qualitative features of the scattered light pattern shown in figure 4.4 does not change appreciably with the presence of the reflective sediment bed. However, other key quantifiable characteristics such as apparent size and brightness as a function of cross-sheet position, do change significantly, which will explored in the next section.

Khalitov and Longmire (2002) suggested using size and brightness criteria to discriminate between various particles and their locations in the light sheet. In a similar manner, we define the size of a particle, a, by the total number of pixels marked using 3.1, and the average brightness as:

$$B = \frac{\sum_{i=1}^{n} I_p(i)}{a} \tag{4.3}$$

where B is the average brightness of a particle, $I_p(i)$ is the intensity of the ith pixel in the original unfiltered image that makes up the particle. Figure 4.5 shows the average brightness and size of three sediment particles vs distance from the center of the laser sheet, one close to the bed (6 mm), one farther away (17 mm), and one very far away (34 mm) from the sediment bed. For all particles, regardless of reflective wall condition, the average brightness and size are the largest in the center of the light sheet and decrease as the particle moves away from the center of the light sheet. Within the first few centimeters of the wall (figures 4.5a and b), particles show an increase in average brightness with the reflective sediment bed in place. In figure (figure 4.5b) at z=-0.8, there is a local maxima of particle

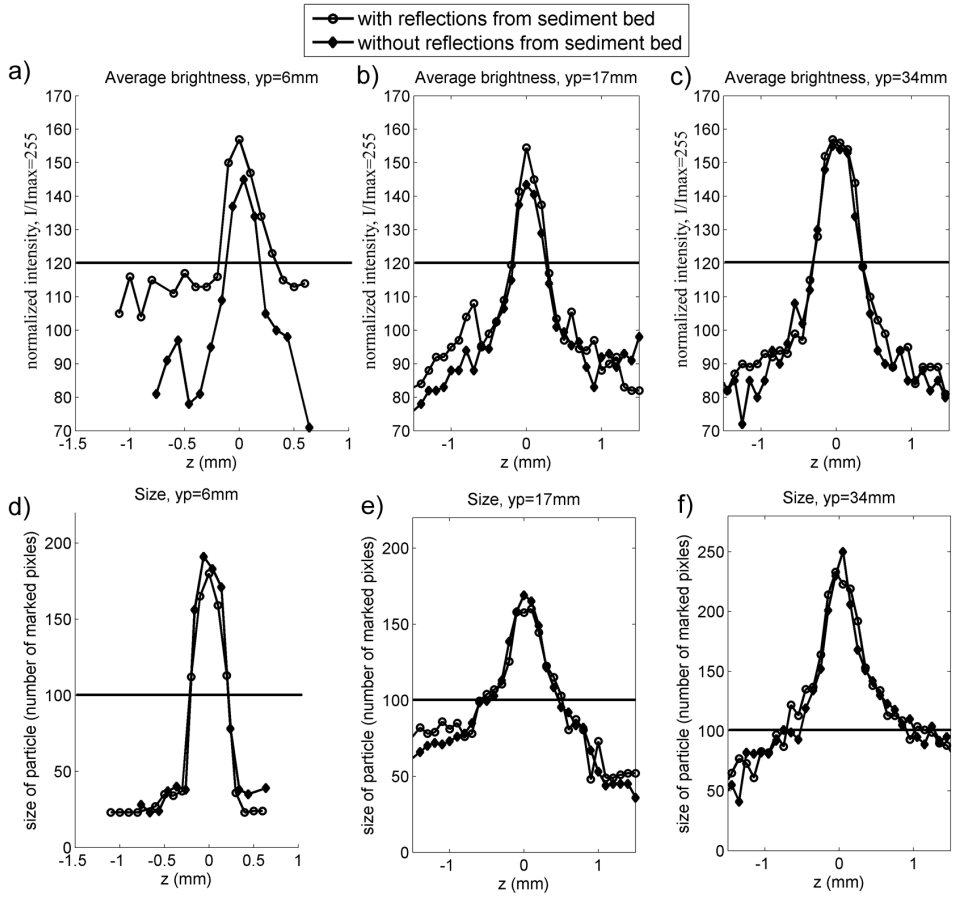

Figure 4.5: *Average particle brightness vs distance from the center of the light sheet for particles at a) y=6 mm, b) y=17 mm, and c) y=34 mm, with and without the reflective bed. Particle size vs distance from the center of the light sheet for particles at d) y=6 mm, e) y=17 mm, and f) y=34 mm, with and without the reflective bed.*

brightness close to 110. This local maximum is where the particle transitions from a large single particle to smaller bright spots as shown in figure 4.4. The sudden decrease in size causes a increase in the average brightness. By 34 mm from the bed, the particle is far enough away such that the effect of the reflection on the average particle brightness and size is not noticeable, except well outside the nominal light sheet (figure 4.5c). The size of the particles, however, is relatively insensitive to the sediment bed reflections (figures 4.5d and e). Outside of the light sheet close to the bed, the light scattered from the bed causes the average particle brightness to remain relatively constant around an average value of 110 for ($\mid z - z_o \mid > 0.3$ mm). Because we are interested in measuring the concentration of sediment particles as well as the velocity, we need to select an average brightness and size criteria that reliably identify particles within a quantifiable volume of the light sheet. Therefore we must only use particles with a brightness and size that is larger than the noise floor created from both bed reflections and scattered illumination, which from our experiment data in the current example, suggests the average brightness must be at least 120 or larger. While the brightness is the primary indicator of a particles location in the light sheet as is most useful for particle discrimination, it must be coupled with an appropriate size criteria to eliminate very small, bright dust or debris which could be above the brightness criteria, but smaller than a dispersed phase particle. To eliminate events that could exceed an average brightness of 120 such as in figure (figure 4.5b) at z=-0.8, we will consider a particle valid and in the light sheet if it has a particle size larger then 100 pixels. This size requirement will also help discriminate against possible spikes in average brightness for particles

close to the sediment bed (figures 4.5a and d) for ($\mid z - z_o \mid > 0.3$ mm), which is considered outside of the effective light sheet.

4.2.1 Concentration validation

The ensemble average particle volume fraction is calculated using:

$$\langle \frac{V_p}{V} \rangle = \frac{\frac{1}{N_f} \sum_{i=1}^{N_f} n_i * V_{sp}}{(\delta x * \delta y * \delta z)} \tag{4.4}$$

where N_f is the number of ensembles, n_i is the number of particles in the ith ensemble, V_{sp} is the volume of a single sediment particle, δx is the in-plane length of the measurement volume, δy is the in-plane height of the measurement volume, and δz is the depth of the measurement volume normal to the sheet. Because the average particle brightness and particle size are functions of the position of the particle in the depth of the light sheet, the identification criteria will determine the effective depth of the measurement volume. The lower the average brightness criteria, the more particles will be included from the outer edges of the light sheet, therefore making the effective measurement depth of the light sheet thicker. Since the size and brightness criteria affect both n_i and δz for calculating the ensemble average particle volume fraction, we need to understand how sensitive the measurement of the ensemble average particle volume fraction is to the size/brightness criteria selected for a given experiment.

Using an average brightness of 120 and a size of 100 pixels, the effective measurement depth can be obtained from individual particles traversed through the light sheet. Figure 4.6 shows the effective measurement depth of individual particles at

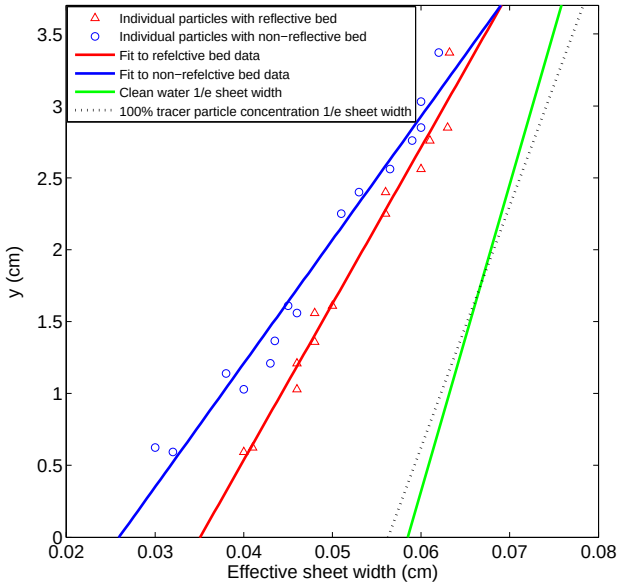

Figure 4.6: *Effective measurement depth in the light sheet of individual particles with and without a reflective sediment bed along with 1/e sheet width measurements with and without tracer particles. Fit lines are a least squares fit to the individual particles*

various distances from the bed. For each bed condition, a linear least squares fit was constructed and used as the effective measurement depth. From figure 4.6, it can be seen that the reflective sediment bed increases the effective detection distance for the sediment particles in the light sheet. Using the direct calibration above, the effective δz is now known. From figure 4.5, reasonable criteria were selected for both the reflective and non-reflective case, and as shown in figure 4.7, using the proper ∂z from the calibration yields the same concentration for the reflective and non-reflective beds. Applying the effective measurement depth fits to known concentrations of particles suspended in a dense hydro-polymer gel yields agreement of $\pm 17\%$ from the actual volume fraction for volume fraction of $1x10^{-4}$ and $\pm 12\%$

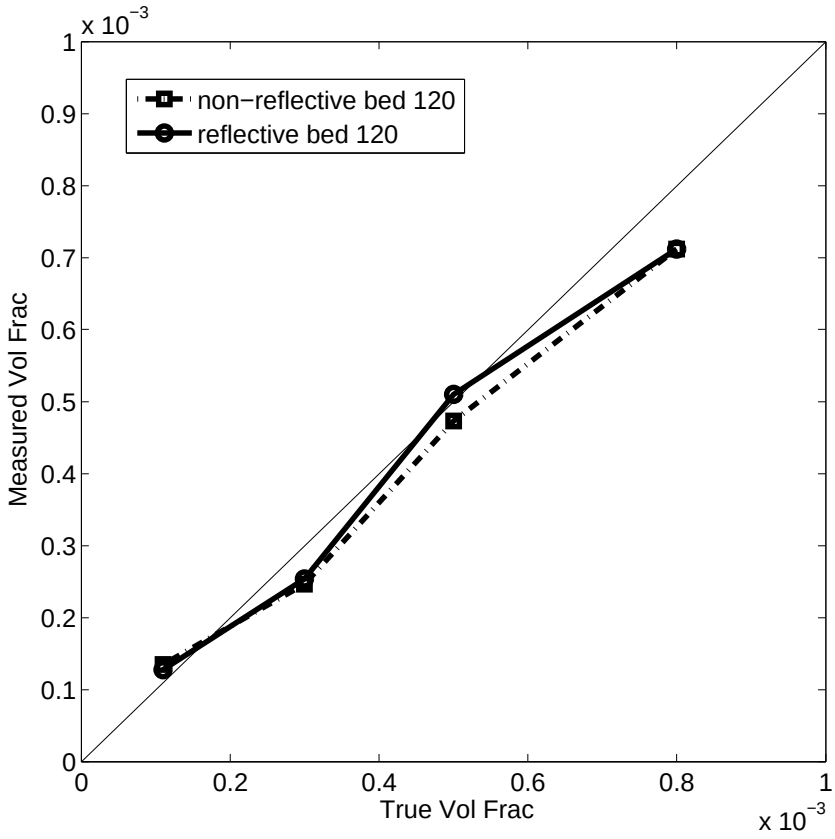

Figure 4.7: *Measured vs actual sediment particle volume fraction for various average brightness identification criteria*

for volume fractions larger than $1x10^{-4}$ for a reflective and non-reflective bed, see figure 4.7.

Without prior knowledge of the complex effects of particle illumination generalized in equation 4.1, using the $1/e$ sheet width seems like a reasonable value for δz in equation 4.4. Figure 4.8 shows the particle concentration using $1/e$ sheet width in comparison to the concentration calculated using sheet width obtained by calibration via traversing particles through the light sheet. Using the $1/e$ sheet width yields a clear bias from the actual value typically on the order of 50%, while

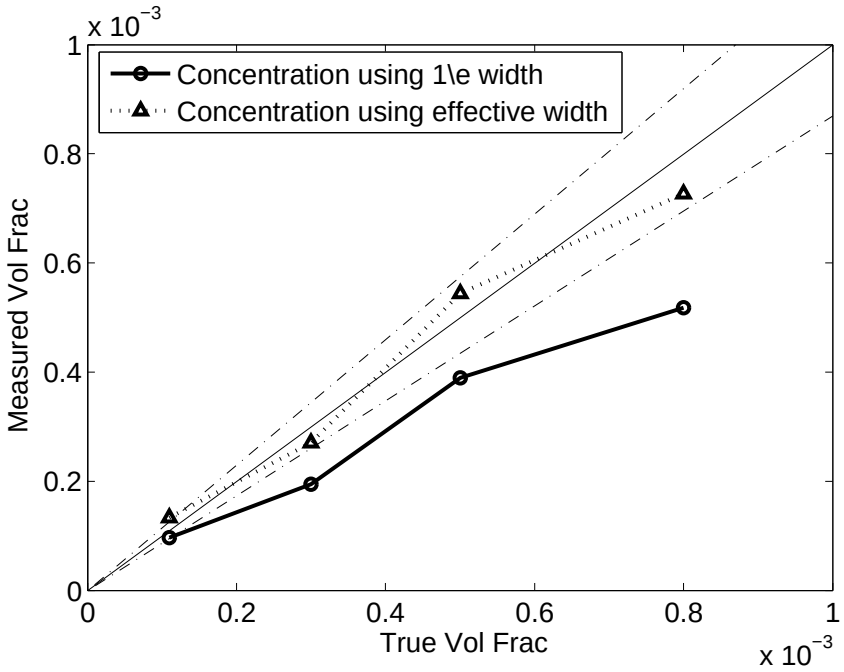

Figure 4.8: *Particle concentration using* $1/e$ *sheet width and particle concentration using sheet width obtain directly from traversing particles through the light sheet. Dash-dot lines are* $\pm 15\%$ *error bounds.*

using the effective sheet width obtained directly from traversing particles through the light sheet yields the volume fraction nominally within $\pm 15\%$ from the actual volume fraction.

Figure 4.9 shows the measured volume fraction vs actual volume fraction of sediment for various average brightness criteria. There is a systematic variation between the actual measured concentration and the average brightness criteria. However, all of the criteria tested yielded a volume fraction within $\pm 25\%$ of the actual volume fraction of the entire mixture. Brightness values above 140 yielded unacceptable results, because the measurement volume becomes very thin and the brightness criteria is too close to the maximum brightness of the particles, which

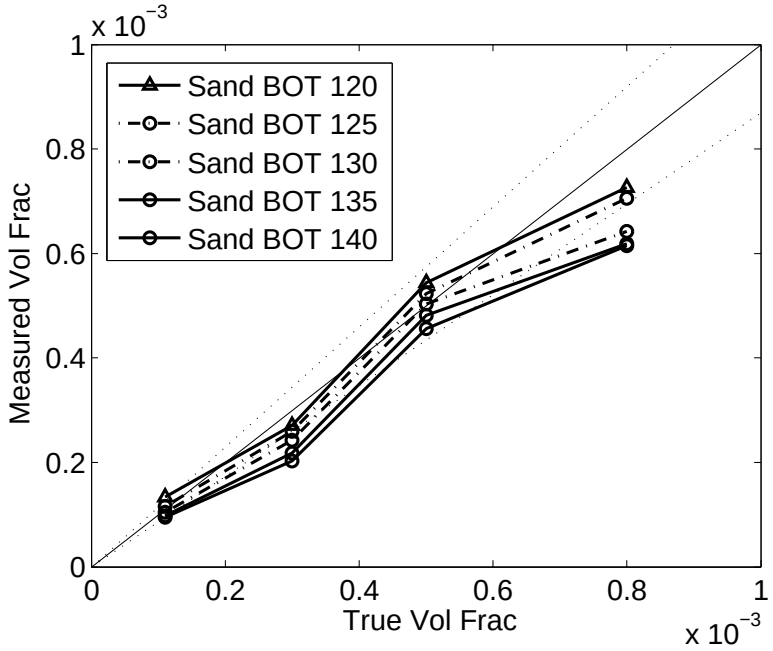

Figure 4.9: *Measured vs actual sediment particle volume fraction for various average brightness identification criteria. Dotted lines are* $\pm 15\%$ *error bounds.*

varied between values of 144 and 158.

If the entire measurement region is large enough that attenuation from the tracer particles is significant, the particle brightness will change based on the vertical location of the particle. Mie scattering theory is an analytical solution to Maxwell's equations for the scattering of light from spherical particles. For particles of the same size, with monochromatic incident light, the intensity of light scattered from a particle reduces to a function only of the scattering angle. For a constant viewing angle, the intensity of light reflected by a particle is directly proportional to the intensity of incident radiation upon the particle. For a statistical large sample of uniformly distributed particles, the mean brightness of a statistical sample can be used as a measure of the mean incident light upon the particles. The particle images can be scaled to produce images where the mean brightness of the statistical sample

is no longer a function of position. This allows the particle images to remove the effect of light attenuation from the tracer particles which gives uniform detectability to the particles.

Figure 4.10 shows the uncorrected and corrected ensemble averaged particle volume fraction of a sediment cloud traversing over a ripple bed with ripple crest located at the origin and ripple wavelength (λ). Due to constants of the experiment, the entire flow field could not be captured simultaneously, the black lines indicate each of the individual measurement regions that make up the 500 images in the ensemble. The uncorrected volume fraction uses the 1/e sheet width at the sediment bed for the entire domain identifying particles with an average brightness of 120 or greater and a size greater than 100 pixels. The corrected volume fraction uses the effective sheet width obtained from figure 4.6, using the average brightness of the ensemble of particles to correct for differences in incident illumination flux on the particles from light sheet attenuation over the measurement domain and variations in particle illumination due to small variations in tracer particle seeding density. Accounting for these variations removes the volume fraction bias from light sheet attenuation and improperly determining the measurement volume, while removing the discontinuities along the measurement boundaries from illumination variations due to small variations in seeding density/light sheet attenuation.

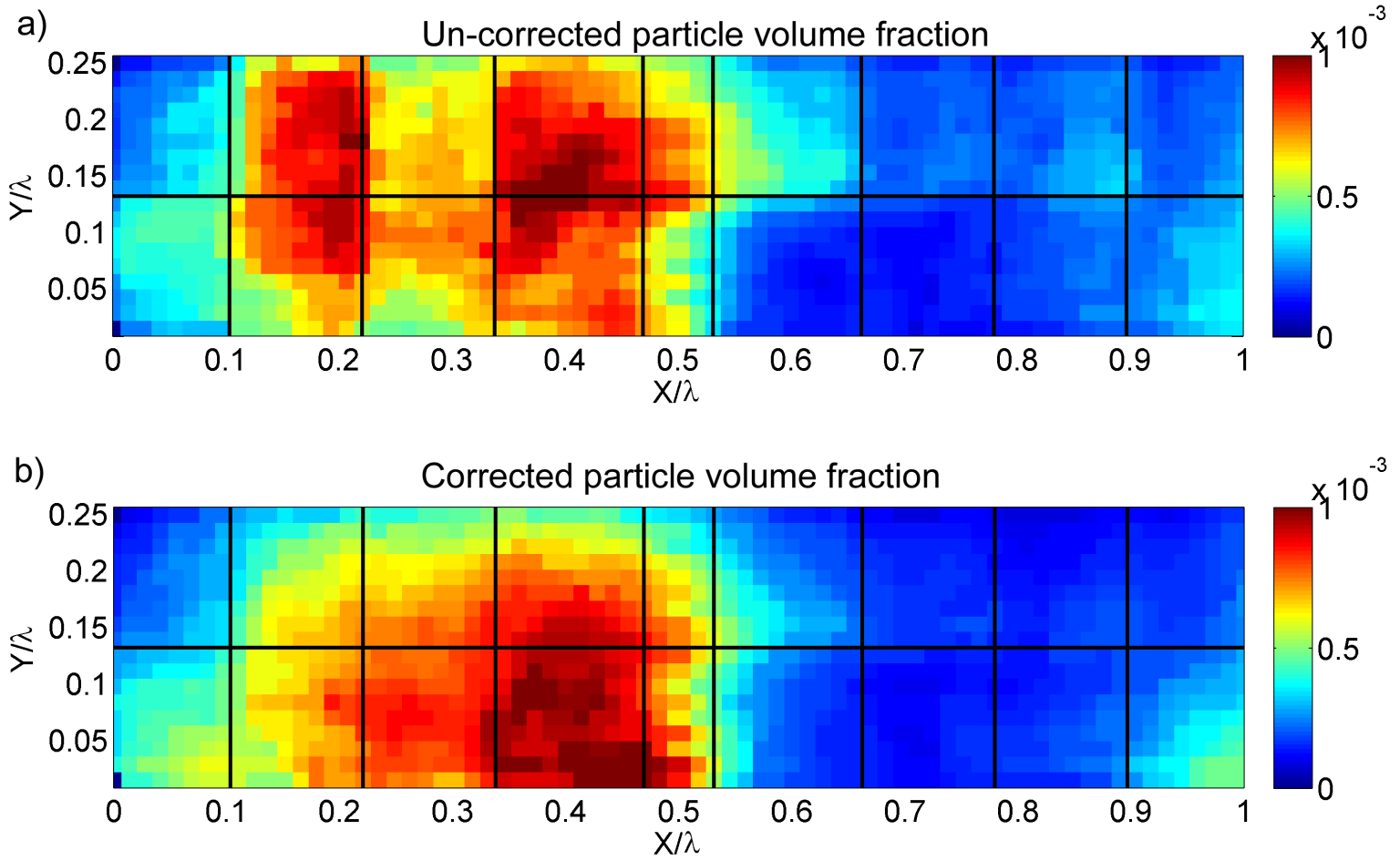

Figure 4.10: *Uncorrected and corrected ensemble averaged particle volume fraction of a sediment cloud traversing over a ripple bed with ripple crest located at the origin and ripple wavelength (λ)*

Chapter 5

Results and discussion

5.1 Description of the flow

Figure 5.1 shows the fluid stream lines with background colored by velocity magnitude at t/τ=0.00, 0.09, 0.16, 0.27, 0.33, 0.38, 0.44, and 0.49 with the origin located at the tip of the ripple crest and flow reversal occurring at $t/\tau = 0.00$ and 0.50. At flow reversal, a large vortex is present, centered at $x/\lambda = 0.28$ and $y/\lambda = 0.00$. As time progress, the vortex moves outward into the flow and the flow accelerates from right to left until the flow reaches maximum velocity at $t/\tau = 0.25$. When the flow is decelerating with an adverse pressure gradient, $0.25 < t/\tau < 0.50$, the boundary layer separates as it flows over the ripple crest. Given the measurement domain of the current experiments, the region of separated flow is not directly observed. Indirectly, however, this can be observed as a region where the flow streamlines transition from following the contours of the bed topography (as typified by $x/\lambda \approx 0.8$, $t/\tau = 0.16$) to a flow pattern where they extend horizontally from the lee crest with little curvature ($x/\lambda \approx 0.8$, $t/\tau = 0.33$). From numerical simulations and experimental measurements [59], it is known that the separated flow creates the large region of vorticity on the lee side of the ripple, which is subsequently ejected into the outer region at flow reversal, consistent with the current flow. Figure 5.2 shows the 2D turbulent kinetic energy ($q = 1/2(\langle u'^2_f \rangle + \langle v'^2_f \rangle)$) of the fluid at

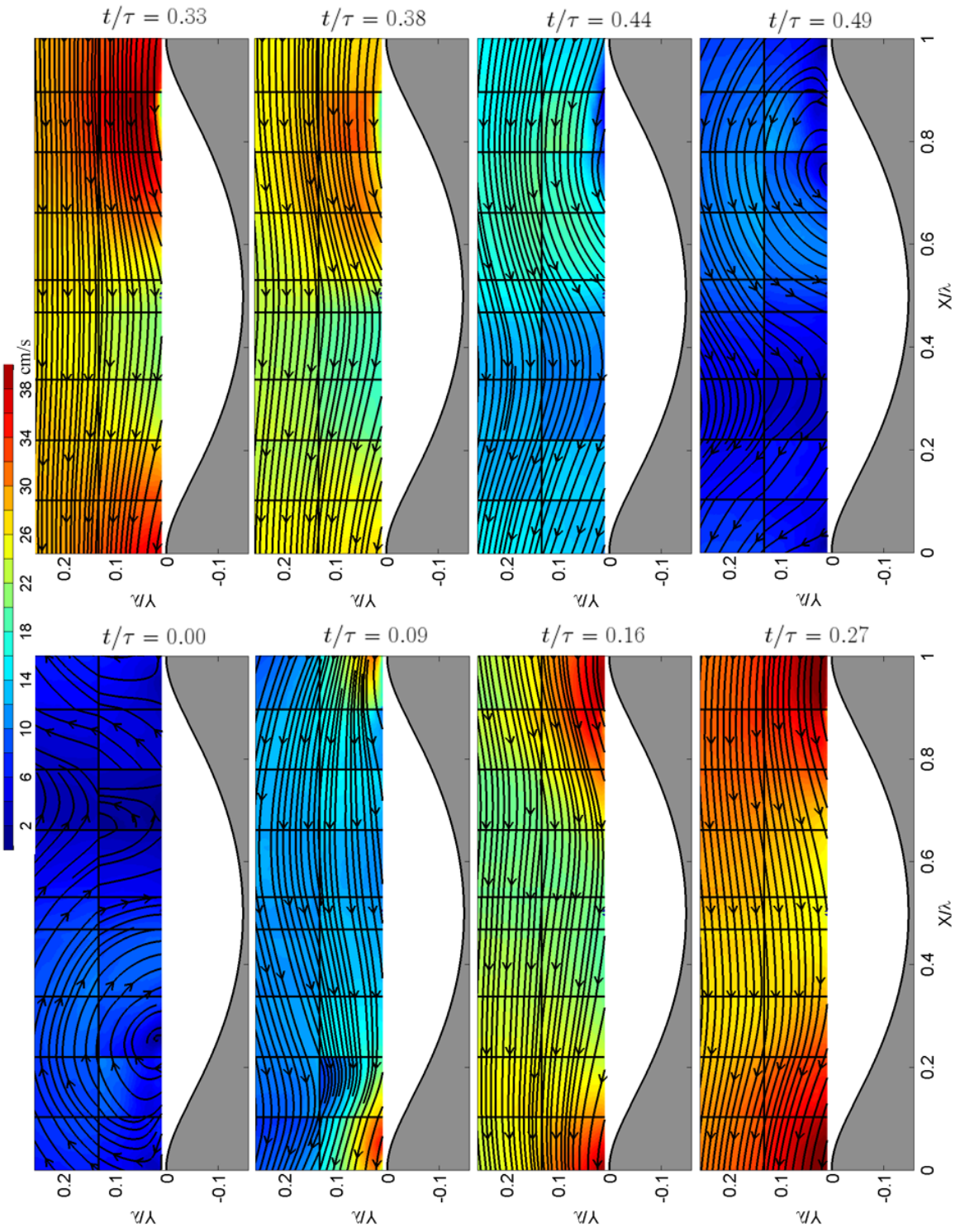

Figure 5.1: *Fluid stream lines with the background colored by fluid velocity magnitude at t/τ=0.00, 0.09, 0.16, 0.27, 0.33, 0.38, 0.44, and 0.49*

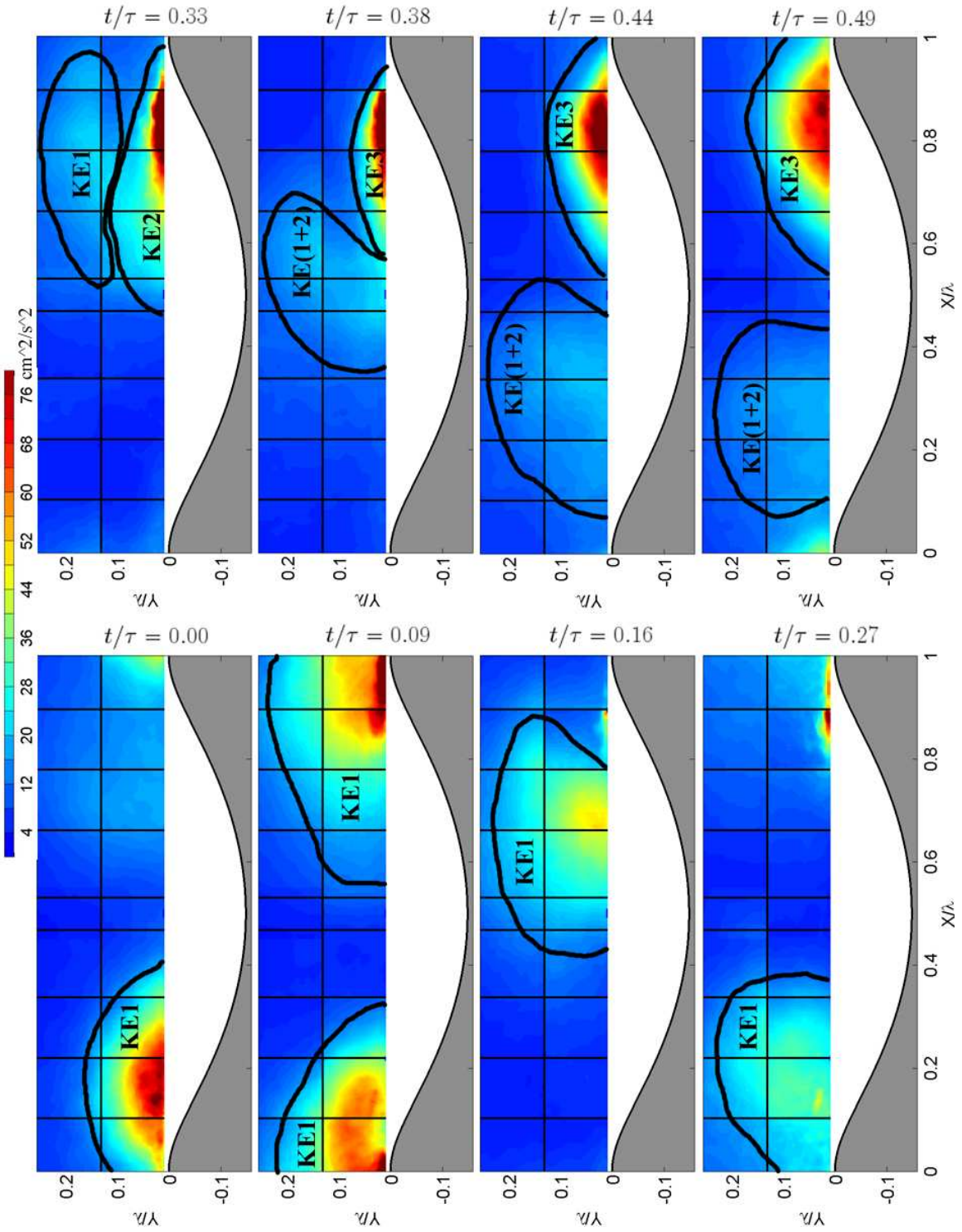

Figure 5.2: *Turbulent kinetic energy of the fluid at t/τ=0.00, 0.09, 0.16, 0.27, 0.33, 0.38, 0.44, and 0.49*

t/τ=0.00, 0.09, 0.16, 0.27, 0.33, 0.38, 0.44, and 0.49. At flow reversal there is a large region of turbulent kinetic energy (indicated by the region marked "KE1") that was created from the flow separation around the ripple crest. As time progresses to t/τ=0.09, the flow convects the turbulence over the ripple and down the lee side of the ripple. Once the region of turbulence moves over the ripple crest, it diminishes significantly in size and decays in strength by approximately 40%. From t/τ=0.16 to t/τ=0.27, the turbulent structure slowly decays and diffuses as it's convected through the measurement volume until t/τ=0.33 where it begins to combine with another structure being created by the separation from the ripple crest (indicated by the region marked "KE2"). At t/τ=0.38, a small part of the KE2 combines with the weaker KE1, while separation from the ripple crest causes turbulence behind the crest to grow indicated by region KE3. Until the next flow reversal at t/τ=0.50, the turbulent structure KE1+2 decays slowly but is still present at flow reversal, while KE3 continues to grow until it is convected over the ripple in symmetry with the formation of KE1. Figure 5.3 shows the fluid Reynolds stress throughout the first half of the flow cycle. Flow separating from the ripple crest at flow reversal, t/τ=0.00, creates a large region of negative Reynolds stress as indicated by the region marked "RS1", which corresponds roughly to the similar marked region in the turbulent kinetic energy shown in figure 5.2. At t/τ=0.09, the large region of negative Reynolds stress is moving over the ripple crest and a small positive region of Reynolds stress (region "RS2") forms just below RS1 on the lee side of the ripple. By t/τ=0.16, RS1 has greatly diminished in strength and is hardly observable while RS2 detaches from the ripple and is being advected in the flow. Comparing the

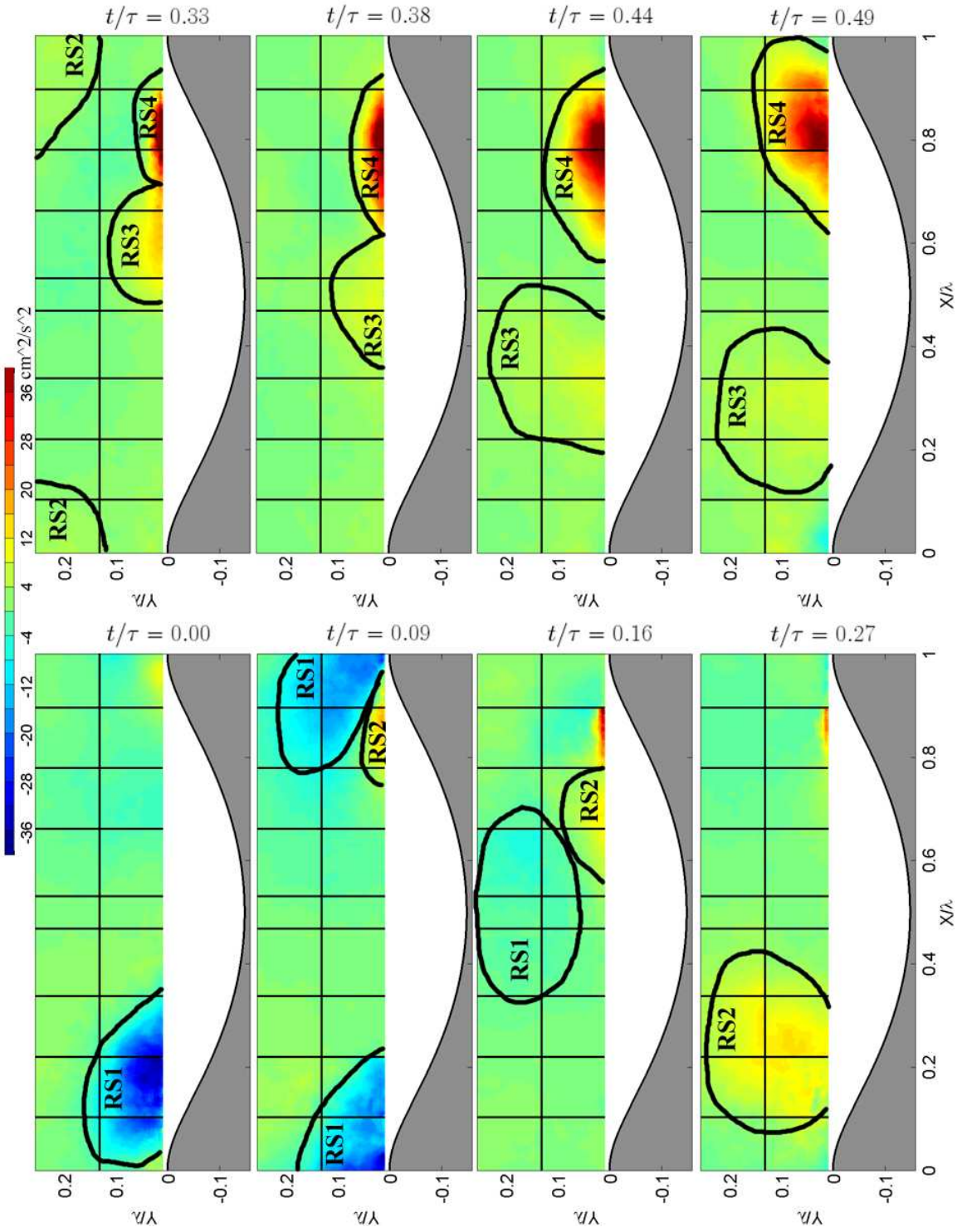

Figure 5.3: *Fluid Reynolds stress at t/τ=0.00, 0.09, 0.16, 0.27, 0.33, 0.38, 0.44, and 0.49*

Reynolds stress and turbulent kinetic energy at t/τ=0.16 reveals that the region of turbulent kinetic energy KE1, roughly corresponds to the Reynolds Stress structure RS2. At t/τ=0.27, the structure is moving through the measurement region until t/τ=0.33, where RS2 is diminished in strength and moving out of the measurement volume though the upper boundry. At that same instant in time, flow separation from the adverse pressure gradient is creating another region positive Reynolds stress (region "RS3") near the ripple crest for $y/\lambda < 0.075$ and $0.48 < x/\lambda < 0.70$. It is interesting to note that at t/τ=0.33, the diminished turbulent kinetic energy of KE2, is between RS2 and RS3 in the Reynolds Stress where the Reynolds stress is small, but slightly negative. This means that although the fluctuations in this region are measurable, as indicated by the turbulent kinetic energy, they are predominantly uncorrelated in the stream-wise and wall normal directions. As time progresses from t/τ=0.38 to t/τ=0.49, RS3 breaks away from the ripple crest, being transported by the weak flow near flow reversal, while RS4 grows and begins to move over the ripple crest.

Figure 5.4 shows the particle stream lines with background colored by particle volume fraction throughout the first half of the flow cycle. At flow reversal, the vortical structure created by separation from the ripple crest ejects sediment from the bed into the flow (the approximate suspended sediment/particulate cloud indicated by P1). As the flow accelerates, the cloud diffuses, growing larger as is moves over the ripple crest. As time progresses, the sediment cloud moves over the valley between the ripples and at $t/\tau = 0.27$, and begins to merge with another sediment cloud (P2). At $t/\tau = 0.27$, the boundary layer over the ripple crest has separated,

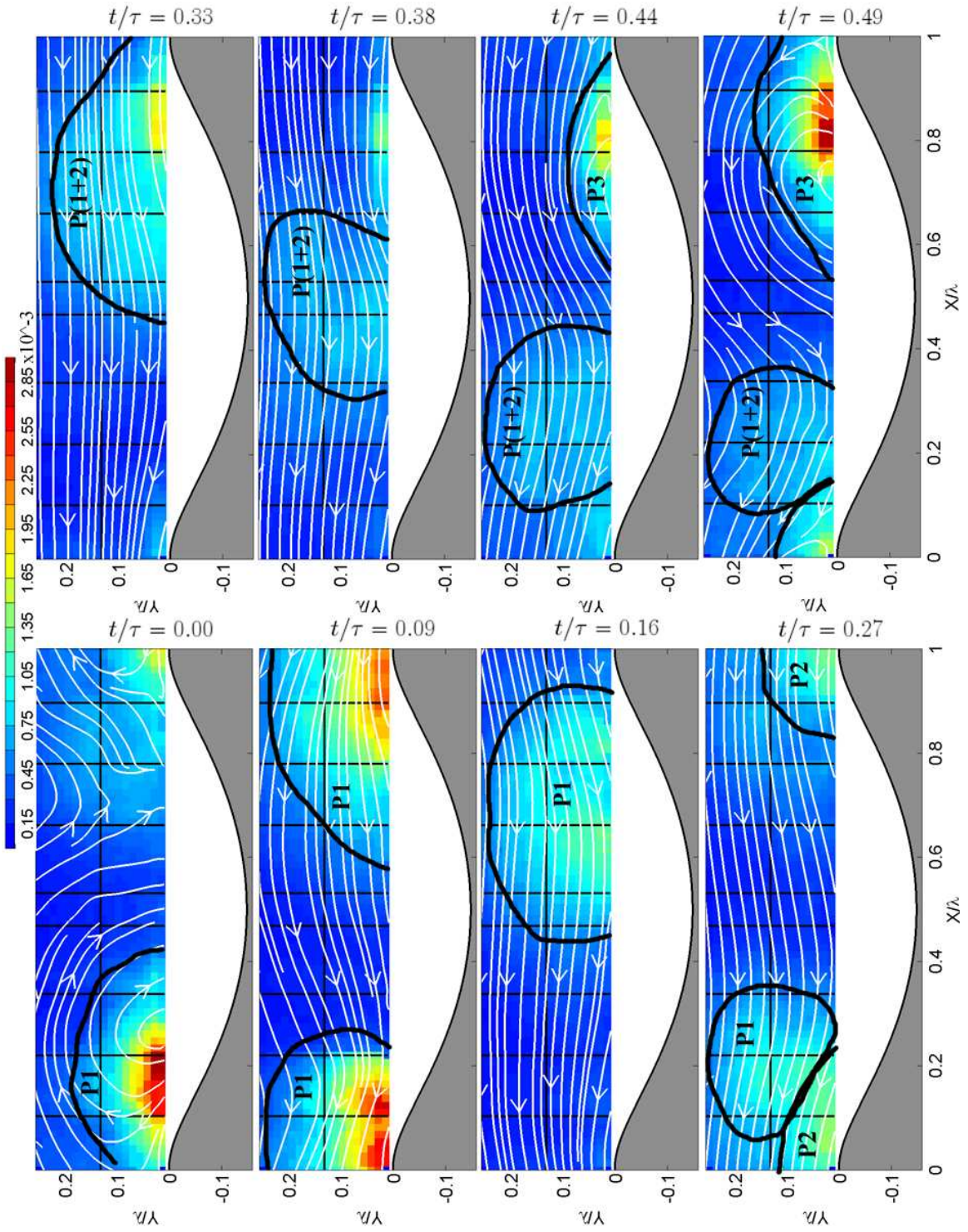

Figure 5.4: *Particle stream lines with the background colored by particle volume fraction at t/τ=0.00, 0.09, 0.16, 0.27, 0.33, 0.38, 0.44, and 0.49*

causing a high shear region which ejects sediment from the bed into the flow as seen by the increase in volume fraction near the ripple crest. By $t/\tau = 0.333$, this cloud of suspended particles has moved more then one wavelength and a cloud produced from an adjacent ripple under the same conditions, enters the measurement volume. The cloud suspended from flow reversal (P1) and the sediment cloud suspended from maximum velocity (P2) have merged as indicated by region P(1+2). As the flow continues to decelerate approaching flow reversal, the sediment cloud concentration diminishes as particles diffuse and settle. However, a significant suspension of particles is still observed a $t/\tau = 0.489$ at $x/\lambda = 0.276$ just immediately before next sediment cloud (P3) is ejected at the subsequent flow reversal.

To understand how the fluid turbulence plays a role in the particle suspension, figures 5.5 and 5.6 show the magnitude of fluid Reynolds stress with contour lines of particle volume fraction and the difference between fluid Reynolds stress and particle Reynolds stress on the right ($\langle u'_f v'_f \rangle - \langle u'_p v'_p \rangle$) at several points in the flow cycle. At $t/\tau = 0.000$, $0.00 < x/\lambda < 0.30$, and $0.00 < y/\lambda < 0.10$, a large region of fluid turbulence and high concentration of sediment particles is present from the large vortical structure ejecting sediment from the bed at flow reversal. The smaller concentration region at $0.65 < x/\lambda < 0.9$ and $0.00 < y/\lambda < 0.20$ is a diminished sediment cloud that was created one period prior. At $t/\tau = 0.09$, the sediment cloud is moving over the ripple crest in conjunction with the large region of negative fluid Reynolds stress, while a small region of positive stress is created on the lee side of the ripple. As time progresses, the sediment and turbulence cloud moves down the lee side of the crest. At $t/\tau = 0.33$, the turbulent structure seen at

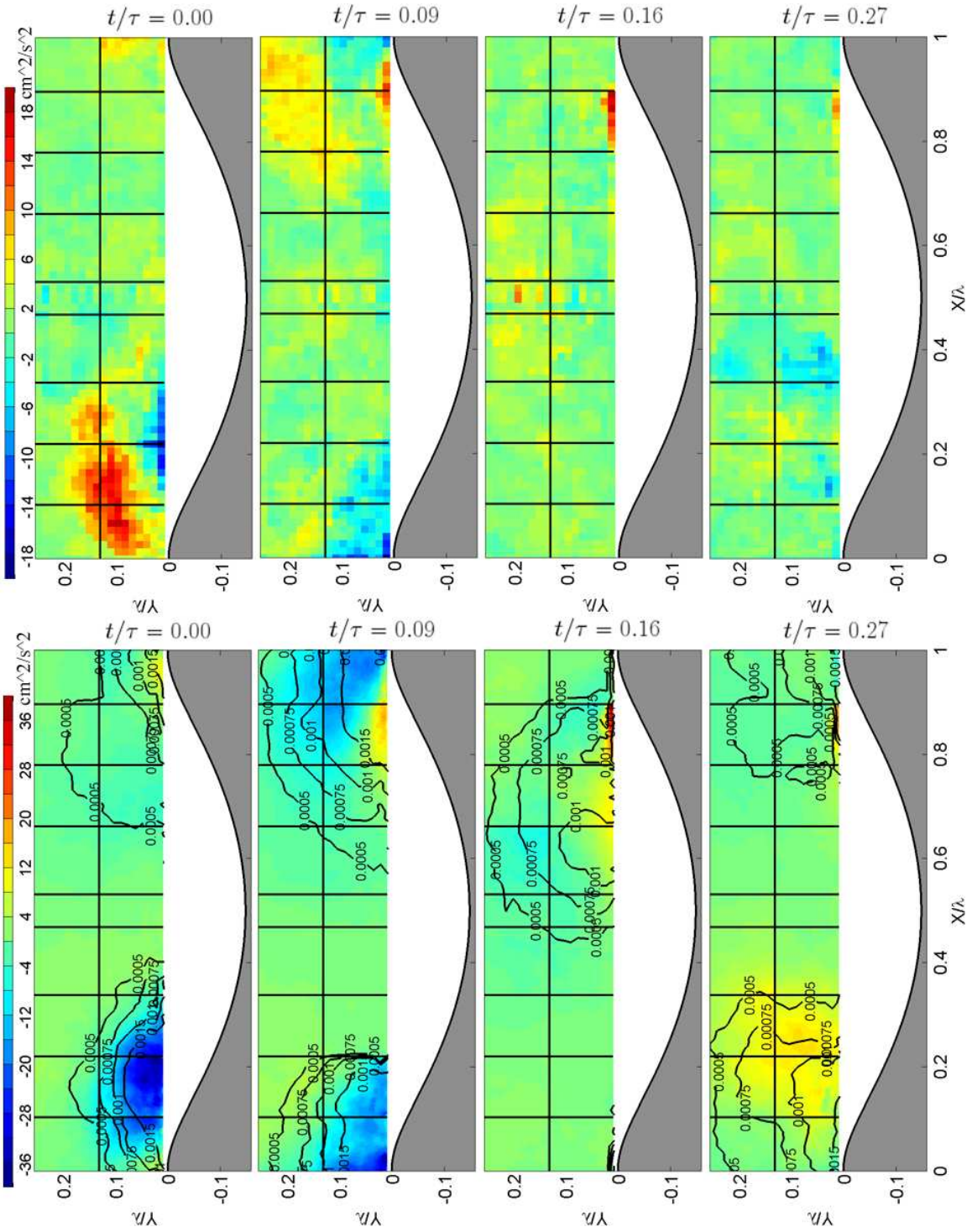

Figure 5.5: *Filled contour plots of fluid Reynolds stress with contour lines of particle volume fraction on the left and filled contour plots of the difference between fluid Reynolds stress and particle Reynolds stress on the right* $\langle u'_f v'_f \rangle - \langle u'_p v'_p \rangle$ *at* t/τ*=0.00, 0.09, 0.16, and 0.27 with the origin located at the tip of the ripple crest*

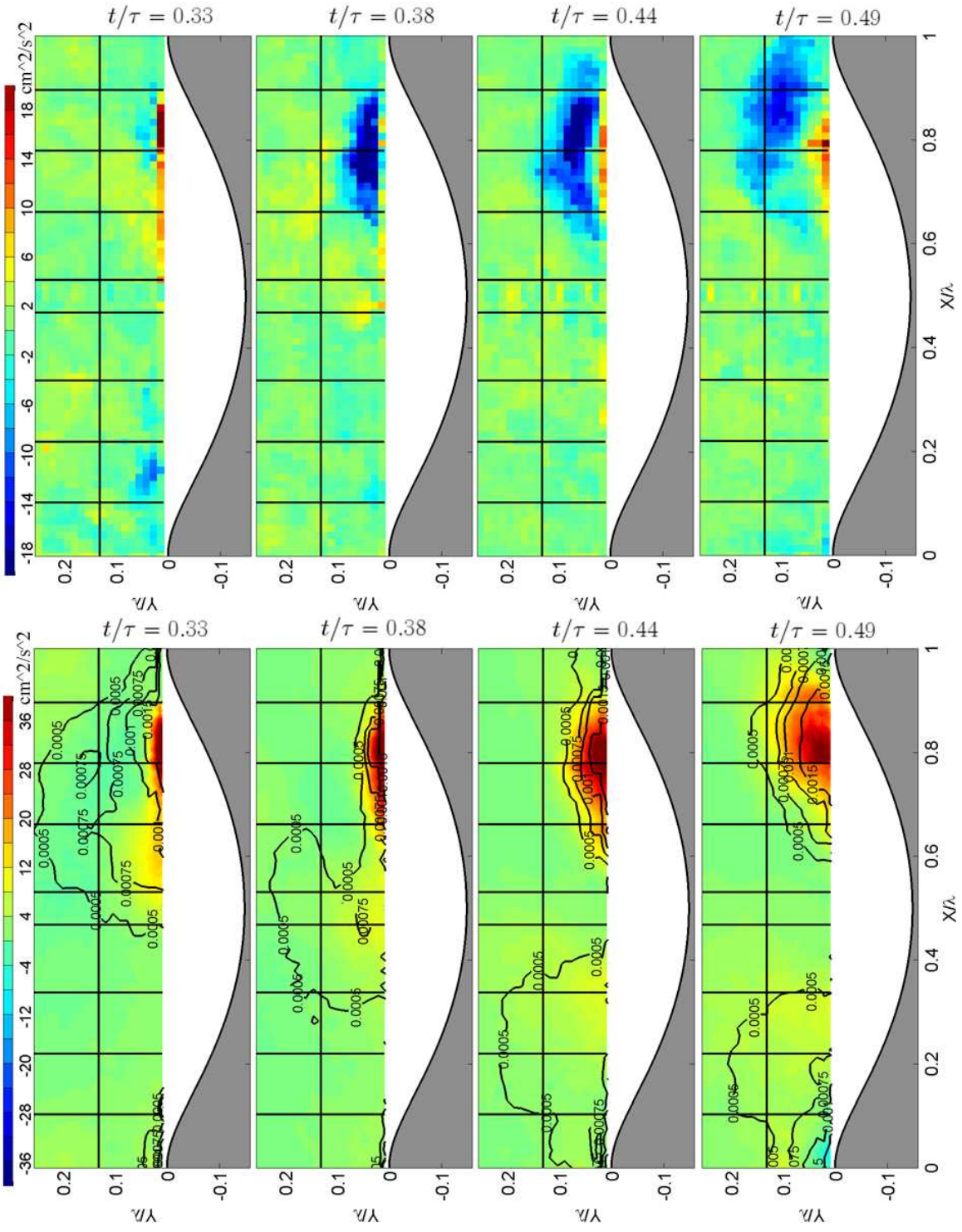

Figure 5.6: *Filled contour plots of fluid Reynolds stress with contour lines of particle volume fraction on the left and filled contour plots of the difference between fluid Reynolds stress and particle Reynolds stress on the right* $\langle u'_f v'_f \rangle - \langle u'_p v'_p \rangle$ *at* t/τ*=0.33, 0.38, 0.44, and 0.49 with the origin located at the tip of the ripple crest*

$t/\tau = 0.27$ has moved over and above the ripple crest at $y/\lambda > 0.15$, while another turbulent structure is created from the crest. From $0.38 < t/\tau < 0.49$, the sediment cloud moves over the valley and diminishes slowly around the region of decaying turbulence. At all points in the cycle, the particle Reynolds stress has a qualitatively similar structure and magnitude to the fluid Reynolds stress. In order to facilitate a more meaningful comparison, the difference $(\langle u'_f u'_f \rangle - \langle u'_p v'_p \rangle)$ is plotted on the right sides in figures 5.5 and 5.6. The primary differences happen at flow reversal $t/\tau = 0.00$ and $t/\tau = 0.50$, where the particle Reynolds stress appears to lead the fluid, in that the particle have a greater magnitude further into the vertical domain than the fluid. At the moment, it is not currently understood what is causing this, although one can speculate it may have something to do with the strong coherent motion encountered in the initially well-organized vortex.

Examining the traditional (time-averaged) Reynolds averaged Navier-Stokes equation for the fluid, the fluid stress can be decomposed into the sum of two terms: a coherent part $\langle u_f \rangle \langle v_f \rangle$ and a turbulent part $\langle u'_f v'_f \rangle$. Figure 5.7 shows the coherent and turbulent stress, integrated over the ripple wavelength λ, at $y/\lambda = 0.03$ or 5 mm above the ripple crest. At flow reversal, the coherent part and the turbulent part are similar in magnitude, however, the coherent part is significantly larger for the rest of the cycle. This indicates that a larger portion of the momentum transport is contained in the mean flow than in the turbulent fluctuations. Note that due to the symmetry of the flow, the time average of the wavelength-mean stress must be zero. The profiles shown in figure 5.7 do indeed average to zero well within the uncertainty of the measurement or 0.5% of the peak coherent stress.

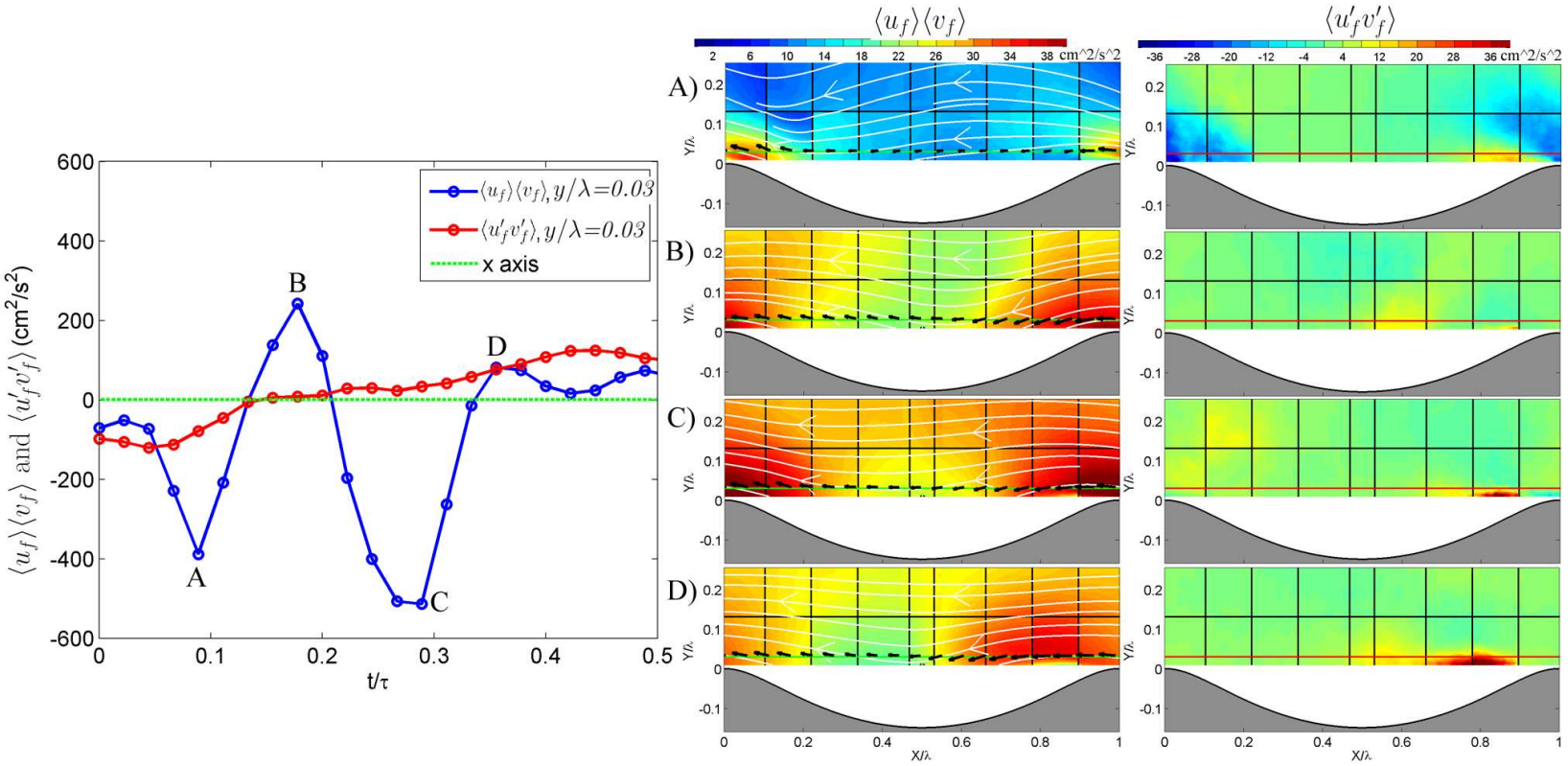

Figure 5.7: *$\langle u_f \rangle \langle v_f \rangle$ and $\langle u'_f v'_f \rangle$ integrated over the entire ripple wavelength in the stream wise direction versus time. Plots in the middle are instantaneous realizations of velocity magnitude at local maxima of the coherent stress with fluid stream lines in white and the integral path line in green. Plots on the right are instantaneous realizations of fluid Reynolds stress at local maxima with the red line indicating the integral path.*

Since the coherent stress results from the ensemble mean convection, the four peaks located at $t/\tau = 0.09, 0.18, 0.29$, and 0.36 can be qualitatively understood by examining the fluid streamlines. At $t/\tau = 0.09$, the steamlines from $0.00 < x/\lambda < 0.27$, are still disturbed from the vortical structure released at flow reversal. This causes the the stream lines to point in the negative x and positive y directions over most of the domain, giving raise to a negative integrated coherent stress. At $t/\tau = 0.18$, the streamlines on the lee side of the ripple at $x/\lambda = 0.90$ curve downward in the negative x and negative y directions sharper than the streamlines moving up on the stoss slope of the ripple, which contributes to the net positive stress. At this time, separation is beginning to occur off of the ripple crest located at $x/\lambda = 0.97$ because at $t/\tau = 0.25$ the pressure gradient switches from favorable to unfavorable causing the flow to separate. Initially the growth of the separated region (not visible) produces a more symmetric flow over the ripple crest, causing the coherent stress to move toward zero (see $t/\tau = 0.29$ or local maxima "C"). Since the pressure gradient is favorable, the fluid near the bed will follow the contour of the ripples. As a possible contributing factor, it is speculated that the asymmetry in the flow at this period may also result from transient asymmetries in ripple profile. As time progresses from $0.18 < t/\tau < 0.29$, the ripple undergoes a reorientation by the erosion from the stoss slope. As the fluid velocity increases, the fluid pushes the top of the ripple closer to the lee side, reorienting the ripple profile from the blue profile to the red profile as illustrated in figure 5.8. It is speculated that this shift in bed geometry causes the coherent stress falls from its maximum positive value at $t/\tau = 0.18$ to its maximum negative value at $t/\tau = 0.29$. The relative maximum

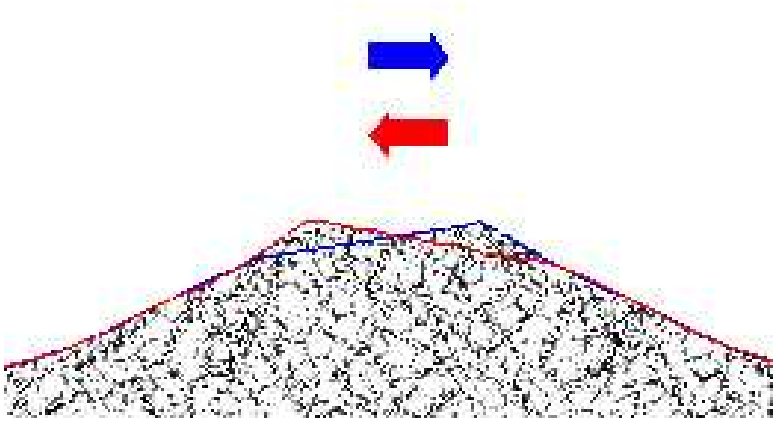

Figure 5.8: *Qualitative illustration of ripple shape morphology. Colored arrows indicate direction of flow for the corresponding colored ripple profile.*

in the coherent stress at $t/\tau = 0.36$ arises because following the negative peak, the flow separation causes the fluid streamlines to cease from following the contours of the bed. Growth of the separation region causes the fluid streamlines to flatten with respect to the wall normal direction, which reduces the coherent stress.

With regard to the turbulent contribution to the stress, it can be seen in figure 5.7 that just above the crest elevation is largest at flow reversal and decays until the flow decelerates, at which time it changes sign. Figure 5.3 shows a plot of the phase and spatially resolved turbulent Reynolds stress for various times. The turbulent Reynolds stress is a maximum just after flow reversal when the turbulence created from the boundary layer separation convects upwards out of the ripple valley.

5.2 Particle momentum equation development

In the context of oscillatory sediment transport, the problem is further complicated by the periodic forcing, which provides for an unsteady ensemble cyclic

average in addition the the traditional time average. The contribution of the cyclic component relative to the stochastic contribution is significant, and hence presents a useful construct for analysis. To farther dissect the contributions of the long time mean, cyclic mean motion, and ensemble fluctuations on the equations of motion, we propose using a triple de-composition of equation 1.2. By using a triple de-composition, some of the complex interactions present in the mean terms can be more simply modeled and physically understood. However, the number of terms present in the equations significantly increases. The notation for general decomposition of the velocity and density is:

$$u = \overline{u} + u' = \tilde{u} + \widehat{u} + u' \tag{5.1}$$

and

$$\alpha = \overline{\alpha} + \alpha' = \tilde{\alpha} + \widehat{\alpha} + \alpha' \tag{5.2}$$

where (-) is the ensemble mean from a typical double decomposition, ($\tilde{}$) is the long time mean of the quantity, ($\widehat{}$) is the mean cyclic component of the quantity, and ($'$) is the fluctuation about the ensemble mean. Researchers that perform regional type simulations of sediment transport require sub-grid scale models that correctly parameterize sediment transport. In order to examine the relative role of the coherent and stochastic flow to sediment transport, one can examine the triple decomposed time-averaged conservation of mass for the sediment:

$$\underbrace{\partial_x \rho_p \widetilde{\alpha_p} \widetilde{u_p}}_{1} + \underbrace{\partial_y \rho_p \widetilde{\alpha_p} \widetilde{v_p}}_{2} + \underbrace{\partial_x \rho_p \widetilde{\widehat{\alpha_p} \widehat{u_p}}}_{3} + \underbrace{\partial_y \rho_p \widetilde{\widehat{\alpha_p} \widehat{v_p}}}_{4} + \underbrace{\partial_x \rho_p \widetilde{\alpha_p' u_p'}}_{5} + \underbrace{\partial_y \rho_p \widetilde{\alpha_p' v_p'}}_{6} = 0 \tag{5.3}$$

where u_p is the particle velocity in the x direction and v_p is the particle velocity in the y direction. Terms 1 and 2 are the long time average particle mass terms, 3 and

4 are the cyclic contribution to the time-averaged conservation of mass, and 5 and 6 are the contribution from the stochastic fluctuations relative to the ensemble mean mass transport. The results of these terms will be compared in the next section. Note that terms 1 and 3 and 2 and 4 can be replaced by $\partial_x(\rho_p\widetilde{\overline{\alpha_p}\overline{u_p}})$ and $\partial_y(\rho_p\widetilde{\overline{\alpha_p}\overline{V_p}})$ respectfully.

Because the flow near the sediment bed is unsteady, the sediment transport community has shifted to using unsteady closures in an effort to capture some of the time dependant behavior responsible for sediment transport. Since the flow is two-way coupled in regions near the sediment bed, the interfacial transport terms can be important. DNS simulations by Armenio and Fiorotto (2001) have shown that over a wide range of turbulence to particle time scales and density ratio's of 2.6 and above, the particle drag is roughly an order of magnitude larger than the Bassett history force and three orders of magnitude larger than the added mass [67]. So the interfacial transfer between phases ($M_{i,k}$) will be approximated to first order using the particle drag to close the equation.

There are several correlations for the drag on a spherical particle depending on the magnitude of the particle Reynolds number (Re_p). Since the particle Reynolds number is typically on the order of 100 or less for the current study (and most sediment flows involving fine sand), the modified Stokes drag proposed by Schiller and Naumann (1933) [66] is a commonly used correlation that can be used to extend the Stokes drag relation to larger Reynolds numbers. Using the Schiller-Naumann

correction to the Stokes drag yields:

$$Drag = -3\pi\mu D(\langle S_i * n + .15\frac{D * S_i}{\nu} * S_i * n\rangle) \tag{5.4}$$

where μ_f is the dynamic viscosity of the fluid, D is the diameter of the sediment, S_i is the slip velocity in the i_{th} direction ($S_i = u_{p,i} - u_{f,i}$), n is the number of particles per unit volume, and ν is the kinematic viscosity of the fluid. Using the same triple decomposition as above to decompose the slip velocity and number of particles per unit volume, the interfacial transport term becomes:

$$\begin{aligned}
M_{y,p} = -3\pi\mu D(&\underbrace{\tilde{n}\tilde{S}_y}_{1} + \underbrace{\tilde{n}\widehat{S_y}}_{2} + \underbrace{\widehat{n}\tilde{S}_y}_{3} + \underbrace{\widehat{n}\widehat{S_y}}_{4} + \underbrace{\langle n' S'_y\rangle}_{5} + \underbrace{0.15 * \frac{D}{\nu}\tilde{n}\tilde{S}_y|\widetilde{S_y^{0.687}}|}_{6} \\
&+ \underbrace{0.15 * \frac{D}{\nu}\widehat{n}\tilde{S}_y|\widetilde{S_y^{0.687}}|}_{7} + \underbrace{0.15 * \frac{D}{\nu}\tilde{n}|\widehat{S_y^{0.687}}|\widetilde{S_y}}_{8} + \underbrace{0.15 * \frac{D}{\nu}\widehat{n}|\widehat{S_y^{0.687}}|\widetilde{S_y}}_{9} \\
&+ \underbrace{0.15 * \frac{D}{\nu}\tilde{S}_y\langle n'|S_y'^{0.687}|\rangle}_{10} + \underbrace{0.15 * \frac{D}{\nu}\tilde{n}\widehat{S_y}|\tilde{S}_y^{\,0.687}|}_{11} + \underbrace{0.15 * \frac{D}{\nu}\widehat{n}\widehat{S_y}|\widetilde{S_y^{0.687}}|}_{12} \\
&+ \underbrace{0.15 * \frac{D}{\nu}\tilde{n}\widehat{S_y}|\widehat{S_y^{0.687}}|}_{13} + \underbrace{0.15 * \frac{D}{\nu}\widehat{n}\widehat{S_y}|\widehat{S_y^{0.687}}|}_{14} + \underbrace{0.15 * \frac{D}{\nu}\widehat{S_y}\langle n'|S_y'^{0.687}|\rangle}_{15} \\
&+ \underbrace{0.15 * \frac{D}{\nu}|\tilde{S}_y^{\,0.687}|\langle n' S'_y\rangle}_{16} + \underbrace{0.15 * \frac{D}{\nu}|\widehat{S_y^{0.687}}|\langle n' S'_y\rangle}_{17} + \underbrace{0.15 * \frac{D}{\nu}\tilde{n}\langle S'_y|S_y'^{0.687}|\rangle}_{18} \\
&+ \underbrace{0.15 * \frac{D}{\nu}\widehat{n}\langle S'_y|S_y'^{0.687}|\rangle}_{19} + \underbrace{0.15 * \frac{D}{\nu}\langle n' S'_y|S_y'^{0.687}|\rangle}_{20})
\end{aligned} \tag{5.5}$$

Note that terms that are identically zero were removed from equation 5.5. Terms 1 through 4 are the mean momentum transport terms in the Stokes drag, while term 5 is the contribution to the Stokes drag from coherent fluctuations in number of particles and slip velocity. Terms 6 through 20 arise from the Schiller-Naumann

correction to the Stokes drag. Terms 9, 15, 16, 17, and 20 involve the ensemble average of correlation between fluctuations in particle density and fluctuations in slip velocity. When no particles are present in the averaging volume, n' is its maximum negative value, while S'_y is undefined (because slip velocity is a conditional averaged term, only calculated when a dispersed phase particle is present), therefore these terms can not be calculated directly. To circumvent this ambiguity, these terms are calculated using the identity:

$$\langle A'B' \rangle = \langle A * B \rangle - \langle A \rangle \langle B \rangle \tag{5.6}$$

The identity in equation 5.6 allows calculation of the term $\langle A'B' \rangle$ because when the terms on the right hand side of the identity are calculated, when no particles are present, the quantity is zero and not undefined. The particle velocity is obtained through a cross correlation region centered around the location of a particle. Therefore, the resulting particle velocity is obtained at the location of the particle. However, the fluid velocity is obtain by correlation fixed regions in space and may not be located specifically at a particles location. So, the fluid velocity from surrounding points is interpolated onto the location of the particle.

Using the same decomposition for the convection terms in the ensemble aver-

aged particle momentum equation yields:

$$
\begin{aligned}
\langle \partial_j(\rho_p \alpha_p u_j u_i)\rangle = {} & \underbrace{\partial_x(\rho_p \tilde{\alpha_p} \tilde{u_p} \tilde{v_p})}_{1} + \underbrace{\partial_y(\rho_p \tilde{\alpha_p} \tilde{v_p} \tilde{v_p})}_{2} + \underbrace{\partial_x(\rho_p \widehat{\alpha_p} \tilde{u_p} \tilde{v_p})}_{3} + \underbrace{\partial_y(\rho_p \widehat{\alpha_p} \tilde{v_p} \tilde{v_p})}_{4} \\
& + \underbrace{\partial_x(\rho_p \tilde{\alpha_p} \tilde{u_p} \widehat{v_p})}_{5} + \underbrace{\partial_y(\rho_p \tilde{\alpha_p} \tilde{v_p} \widehat{v_p})}_{6} + \underbrace{\partial_x(\rho_p \widehat{\alpha_p} \tilde{u_p} \widehat{v_p})}_{7} + \underbrace{\partial_y(\rho_p \widehat{\alpha_p} \tilde{v_p} \widehat{v_p})}_{8} \\
& + \underbrace{\partial_x(\rho_p \tilde{u_p} \langle \alpha_p' v_p' \rangle)}_{9} + \underbrace{\partial_y(\rho_p \tilde{v_p} \langle \alpha_p' v_p' \rangle)}_{10} + \underbrace{\partial_x(\rho_p \tilde{\alpha_p} \widehat{u_p} \tilde{v_p})}_{11} + \underbrace{\partial_y(\rho_p \tilde{\alpha_p} \widehat{v_p} \tilde{v_p})}_{12} \\
& + \underbrace{\partial_x(\rho_p \widehat{\alpha_p} \widehat{u_p} \tilde{v_p})}_{13} + \underbrace{\partial_y(\rho_p \widehat{\alpha_p} \widehat{v_p} \tilde{v_p})}_{14} + \underbrace{\partial_x(\rho_p \tilde{\alpha_p} \widehat{u_p} \widehat{v_p})}_{15} + \underbrace{\partial_y(\rho_p \tilde{\alpha_p} \widehat{v_p} \widehat{v_p})}_{16} \\
& + \underbrace{\partial_x(\rho_p \widehat{\alpha_p} \widehat{u_p} \widehat{v_p})}_{17} + \underbrace{\partial_y(\rho_p \widehat{\alpha_p} \widehat{v_p} \widehat{v_p})}_{18} + \underbrace{\partial_x(\rho_p \widehat{u_p} \langle \alpha_p' v_p' \rangle)}_{19} + \underbrace{\partial_y(\rho_p \widehat{v_p} \langle \alpha_p' v_p' \rangle)}_{20} \\
& + \underbrace{\partial_x(\rho_p \tilde{v_p} \langle \alpha_p' u_p' \rangle)}_{21} + \underbrace{\partial_y(\rho_p \tilde{v_p} \langle \alpha_p' v_p' \rangle)}_{22} + \underbrace{\partial_x(\rho_p \widehat{v_p} \langle \alpha_p' u_p' \rangle)}_{23} \\
& + \underbrace{\partial_y(\rho_p \widehat{v_p} \langle \alpha_p' v_p' \rangle)}_{24} + \underbrace{\partial_x(\rho_p \tilde{\alpha_p} \langle v_p' u_p' \rangle)}_{25} + \underbrace{\partial_y(\rho_p \tilde{\alpha_p} \langle v_p' v_p' \rangle)}_{26} \\
& + \underbrace{\partial_x(\rho_p \widehat{\alpha_p} \langle v_p' u_p' \rangle)}_{27} + \underbrace{\partial_y(\rho_p \widehat{\alpha_p} \langle v_p' v_p' \rangle)}_{28} + \underbrace{\partial_x(\rho_p \langle \alpha_p' v_p' u_p' \rangle)}_{29} \\
& + \underbrace{\partial_y(\rho_p \langle \alpha_p' v_p' v_p' \rangle)}_{30}
\end{aligned}
\tag{5.7}
$$

Terms 1 through 8 and 11 through 18 are the 16 mean particle convection terms that together form the double decomposed mean term$\partial_j(\rho_p \overline{\alpha_p}\ \overline{u_j}\ \overline{u_i})$. Terms 9, 10, and 19 through 27, are combinations of the convection of momentum that results from combinations of the mean and fluctuating components. Terms 28 through 30 combine to form the particle Reynolds stress. In the next section the contribution of these terms to momentum transport will be examined.

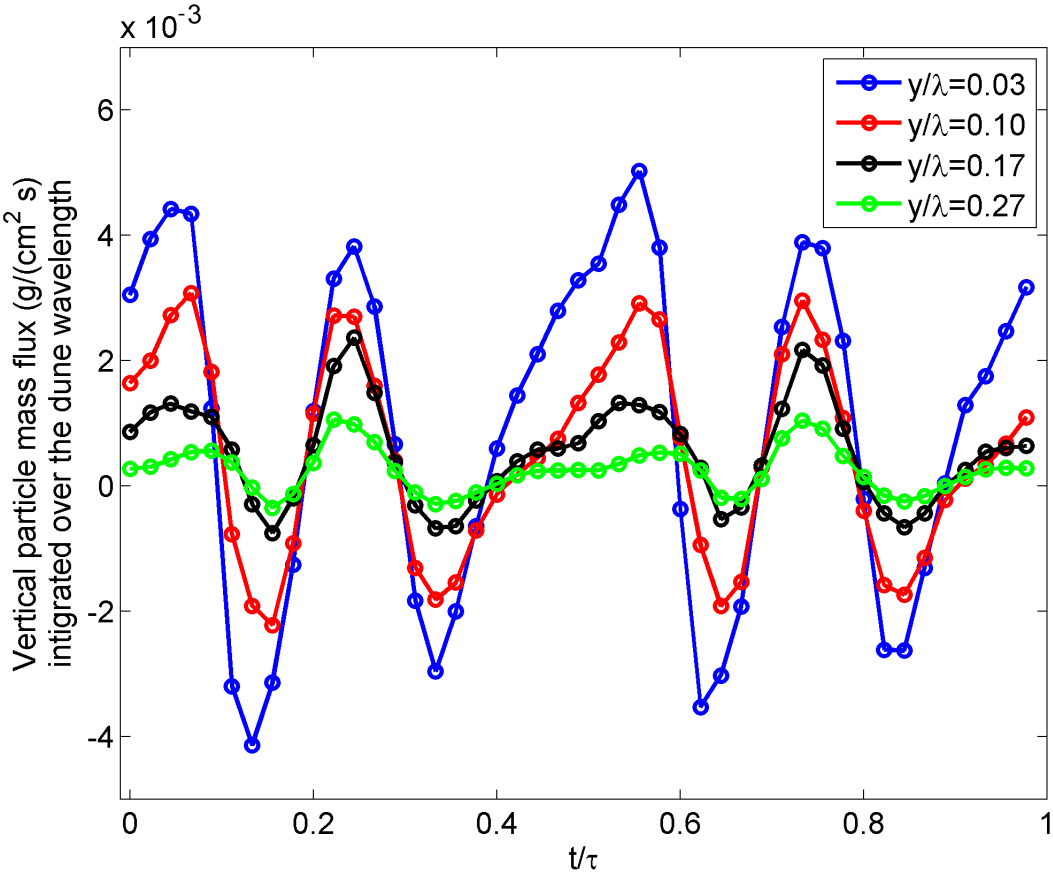

Figure 5.9: *Ensemble averaged particle flux integrated over entire wavelength at y/λ=0.03, 0.10, 0.17, and 0.24 as a function of time*

5.2.1 Sediment quantities

Figure 5.9 shows a plot of the vertical particle flux $\langle(\tilde{\rho_p} + \hat{\rho_p})(\tilde{v_p} + \hat{v_p})\rangle$ integrated over the entire wavelength at y/λ=0.03, 0.10, 0.17, and 0.24 as a function of time. The vertical particle flux shows a long broad peak a $t/\tau = 0.07$, then three alternating peaks of negative and positive flux, corresponding to the movement of the large sediment cloud over the lee (negative flux) and the stoss (positive flux) slope of the ripple. The peak is noticeably broader at flow reversal, during which time the large scale vortical structure is ejecting particles from the lee side of the

ripple outward into the flow, causing a net positive flux of particles into the flow. The subsequent peaks are narrower due to the cloud residence duration over these respective regions as it is advected by the mean flow, around the time of peak oscillation velocity. The maximum integral flux close to the bed ($y/\lambda = 0.03$) is a maximum at flow reversal, with the subsequent peaks exhibiting a steady decay in magnitude because of particles settling out of the flow until the next flow reversal. Interestingly in contrast to this trend, the peaks in vertical particle flux farther from the bed (y/λ=0.17 and 0.24), show an increase from flow reversal to maximum velocity at $t/\tau = 0.25$ due to the merging of the sediment cloud created at flow reversal (P1 in figure 5.4) and the second sediment cloud ejected into the flow around $t/\tau = 0.25$ (P2 in figure 5.4).

The amount of sediment suspended in the flow is an important parameter in predicting the migration of sediment. Figure 5.10 shows the ensemble averaged particle density (g/cm^3) integrated over the ripple wavelength at y/λ=0.03, 0.10, 0.17, and 0.24 as a function of time. Above the plot are instantaneous realizations of particle density at various times labeled T1, T2, T3, and T4, which correspond to various peaks in the ensemble averaged particle density integrated over the ripple wavelength, while the dashed lines in the instantaneous realizations of particle density correspond to the data locations integrated in the lower plot. Point measurements of concentration by Nakato et al (1977) and Sleath (1982) acquired over the ripple crest yielded similar 4 peak behavior. At $t/\tau = 0.04$ and $t/\tau = 0.56$ seconds, just after flow reversal, there is a large increase in suspended sediment near the sediment bed as large scale vortices eject sediment into the flow. As we move

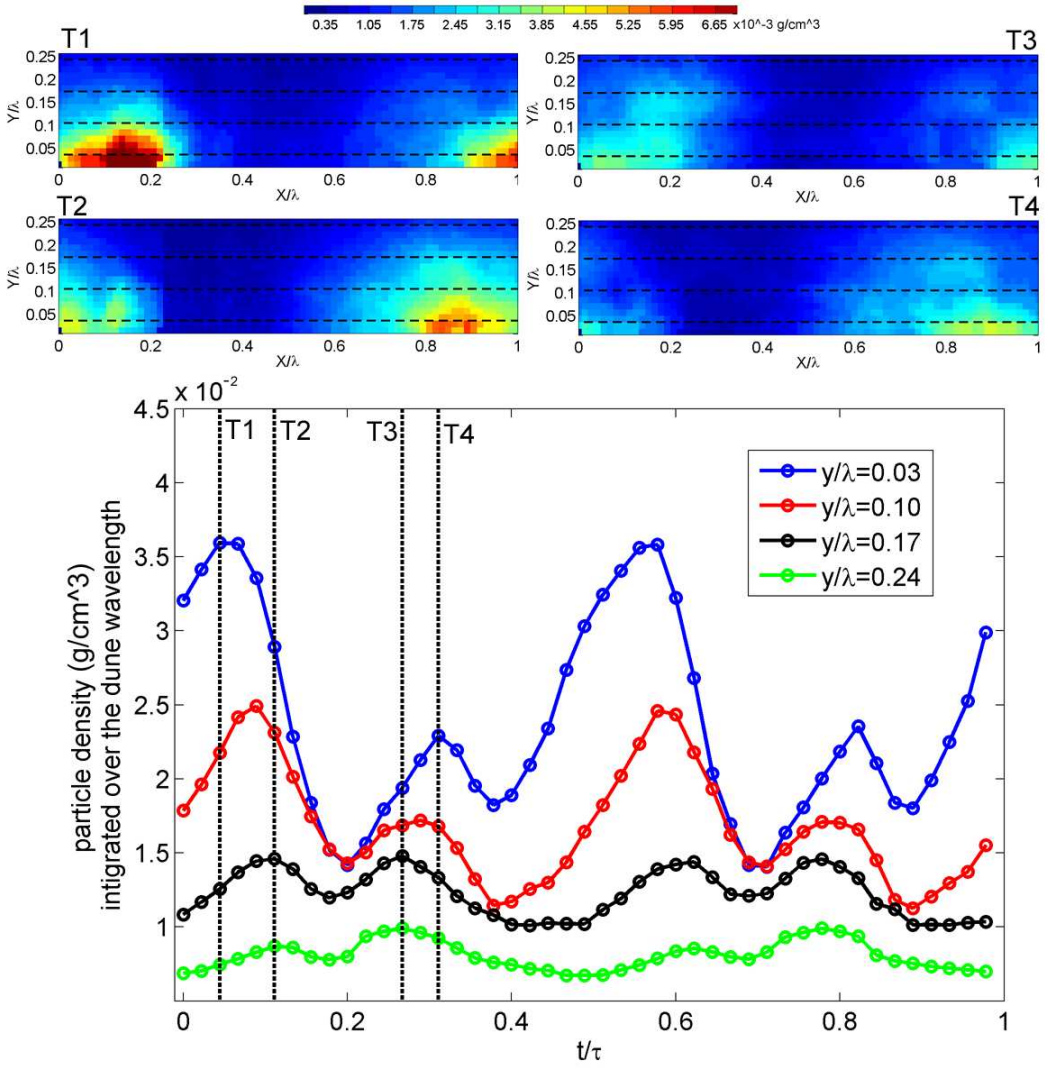

Figure 5.10: *Ensemble averaged particle density (g/cm^3) integrated over the ripple wavelength at y/λ=0.03, 0.10, 0.17, and 0.24 as a function of time. Above the plot are instantaneous realizations of particle density at various times labeled T1, T2, T3, and T4, which correspond to various peaks in the ensemble averaged particle density integrated over the ripple wavelength, while the dashed lines in the instantaneous realizations of particle density correspond to the data locations integrated in the lower plot.*

farther from the bed, the peak in particle density is delayed in time. Examining the phase averaged particle density at $T1$ and $T2$ indicate that the peak in particle density at T1 occurs just after flow reversal while the particle cloud remains small and concentrated. In contrast, the peaks for y/λ=0.17 and 0.24 at $T2$ are delayed in comparison to $T1$ because the sediment ejected from the bed requires time to diffuse and reach the outer regions of the flow. The particle density decreases then increases in magnitude as the suspended particle cloud moves upward and downward following the contours of the sediment bed. The second peak in particle density happens as the sediment cloud produced one wavelength downstream traverses over the ripple. However, the second peak happens earlier in time for regions farther from the sediment bed. The delayed peak at y/λ=0.03 and $T4$ occurs from the increased particle density at $0.8 < x/\lambda < 1.0$. The increase in particle density for y/λ=0.17 and 0.24, similar to the increase in vertical particle flux shown in figure 5.9) is due to the increase in particle density from the merging of the sediment cloud created at flow reversal (P1 in figure 5.4) and the second sediment cloud ejected into the flow around $t/\tau = 0.25$ (P2 in figure 5.4).

Early work by Nakato et al (1977) used optical probes to measure sediment concentration and hot wire anemometry to measure fluid velocity at various points directly over the ripple and valley. Assuming that the sediment velocity differed from the fluid velocity by the still water settling velocity, their measurements over a small portion of the flow indicated that the time averaged sediment flux was non-zero. The current work provides a more complete picture of the net flux hinted at by this prior work. Figure 5.11 shows the fluid stream lines in black solid lines and

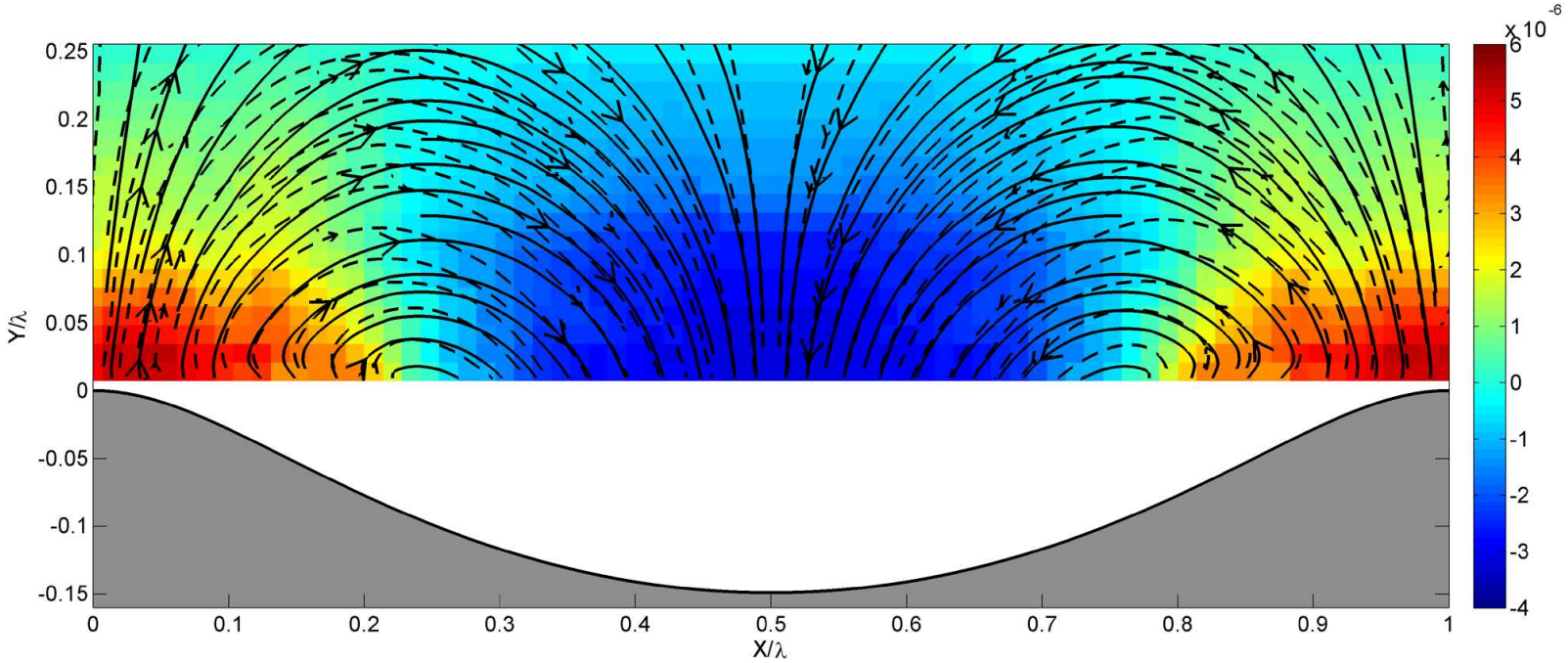

Figure 5.11: *Fluid stream lines in black solid lines and particle stream lines in black dashed lines with the background colored by the time averaged vertical sediment flux* $g/(m^2\ s)$

particle stream lines in black dashed lines with the background colored by the time averaged vertical sediment flux. The large scale recirculation of the fluid causes particles to be transported from the ripple near the crest into the valley between the ripples. The particles mostly follow the fluid streamlines, except gravitational settling allows the particles to cross fluid streamlines and return to the bed, with the largest vertical sediment flux near the ripple crest. Since the flow is purely oscillatory with no mean current, the net flux of the fluid and sediment is zero. This implies that the stream lines in the valley below the ripple crest (data not present in this study) must form closed shapes. Thus while figure 5.11 shows a negative flux of sediment from $0.25 < x/\lambda < 0.75$, the flux lines must implicitly reconnect to those emanating from $0 < x/\lambda < 0.25$ and $0.75 < x/\lambda < 1$ by following close to the ripple slope.

Figure 5.12 compares Nielsen's diffusive concentration model 2.9 for time averaged concentration over the ripple crest to the experimental data. Davies and Thorne in 2005, noted that Nielsen's reference concentration over predicted the concentration and suggested changing the constant for the reference concentration from 0.005 to 0.0022 to better match their results. Nielsen's model over predicts the time averaged concentration profile by roughly a factor of 2 everywhere in the domain in figure 5.12a, while the Davies and Thorne (2005) correction is within 7% of the exponential fit to the experimental data . Normalizing the concentration profiles by the reference concentration at the dune crest (5.12b), revels that the diffusive model predicts the exponential decay length (L_s) within 3% (2.04 1/cm and 1.98 1/cm for the model and fit to data respectfully). Note that Davies and

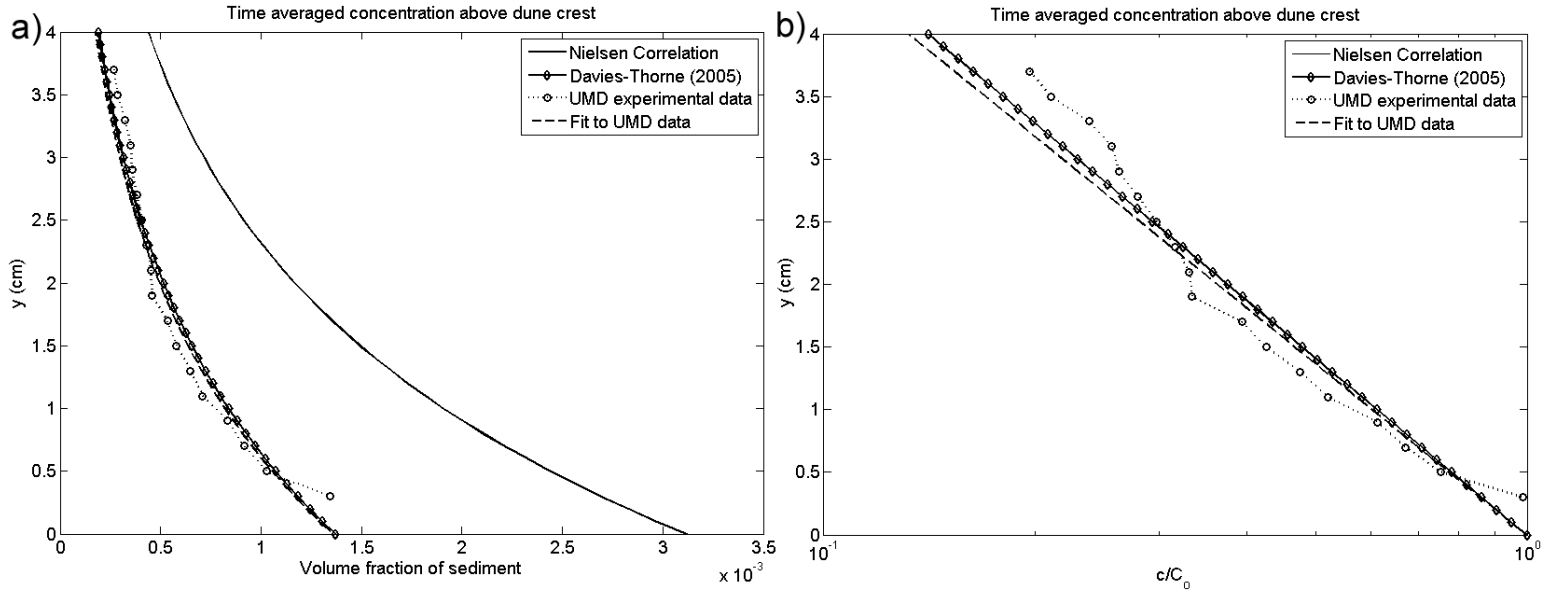

Figure 5.12: *Nielsen's diffusive concentration model 2.9 for time averaged concentration over the ripple crest along with Davies and Thorne's suggested reference concentration update to Nielsen's model compared to UMD experimental data and least squared exponential fit to data. Data is shown in a) linear and b) normalized semilog scale*

Thorne (2005) use the same exponential decay length as Nielsen. It can be concluded that the concentration in the measurement region is well represented by a diffusive model, however the reference concentration for Nielsen's model causes the factor of 2 difference between the predicted and measured concentration profiles. Other researchers [16] have shown that Nielsen's model has been shown to predict the time averaged concentration decay length over the ripple crest within a factor of 2, for concentration profiles within $y < 1.5\eta$ from the ripple crest for 89% of experiments tested.

5.2.2 Conservation equation terms

Figure 5.13 shows the scalar mass flux terms in the time averaged conservation of mass equation for the particles (equation 5.3). The long time averaged mean transport terms ($\rho_p\widetilde{\alpha_p}\widetilde{u_p}$ and $\rho_p\widetilde{\alpha_p}\widetilde{v_p}$) are largely responsible for the long time recirculation of sediment particles shown in figure 5.11, as it accounts for approximately 70% in the outer flow, but only 30% close to the boundary. Terms 3 and 4 are the time average of the cyclic mass flux terms in the stream-wise and wall normal directions respectfully, and term 3 is similar in magnitude to the long time average mean terms 1 and 2. The significance is that models for sediment transport must account for the contributions of both the long time mean sediment flux and the cyclic components. Terms involving ensemble fluctuations (5 and 6) are roughly 50 times smaller than the terms involving mean quantities (1 through 4), therefore the mean motion makes the most significant contribution to the conservation of mass

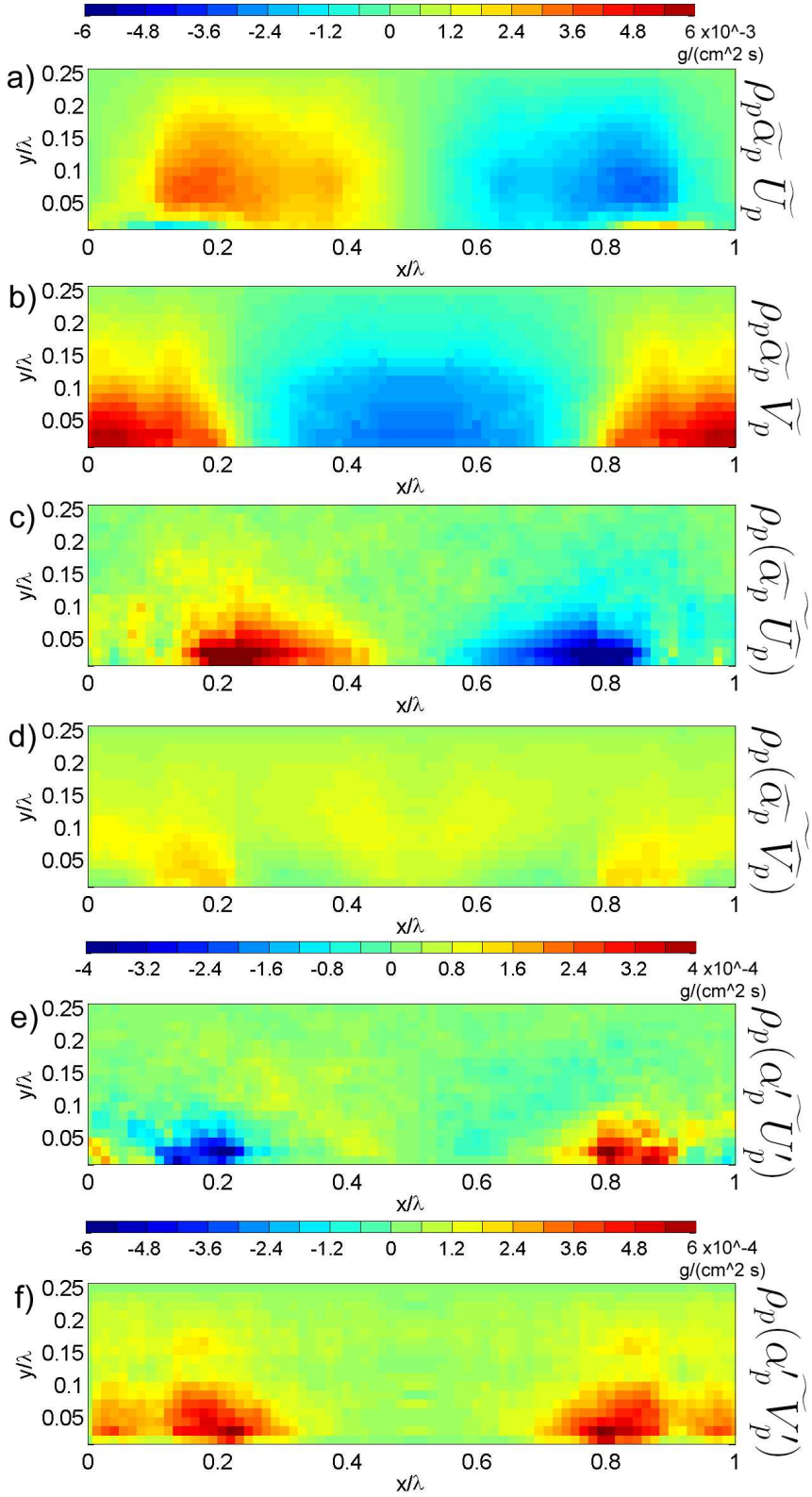

Figure 5.13: *Time averaged particle conservation of mass terms, a)* $\rho_p \widetilde{\alpha_p}\ \widetilde{u_p}$*, b)* $\rho_p \widetilde{\alpha_p}\ \widetilde{v_p}$*, c)* $\rho_p \widetilde{\alpha_p}\ \widetilde{u_p}$*, d)* $\rho_p \widetilde{\alpha_p}\ \widetilde{v_p}$*, e)* $\rho_p \widetilde{\alpha_p' u_p'}$*, f)* $\rho_p \widetilde{\alpha_p' v_p'}$

equation.

Figures 5.14 and 5.15 show the total particle drag (the sum of all 20 terms) and volume averaged body force in the y direction. At flow reversal ($t/\tau = 0$), the body force terms near the ripple crest are roughly 30% larger then the drag terms in the vertical direction, indicating that on average, the sediment particles in the flow will tend to settle back to the sediment bed. As the particle cloud moves over the ripple at $t/\tau = 0.09$, the body force terms near the ripple crest are roughly 30% larger then the vertical drag terms except very close to the ripple crest ($0.0 < x/\lambda < 0.1$ and $y/\lambda < 0.05$) where the body force terms are larger. As the particle cloud moves over the valley, the body force is diminishing from particles settling out of the flow, but remains similar in magnitude to the vertical drag force. At $t/\tau = 0.333$, separation of the flow from the ripple crest causes a large vertical particle drag near the ripple crest. For the remainder of the half cycle, the vertical particle drag remains similar in magnitude to the body force terms until the next flow reversal.

Figure 5.16 shows the sum of the convection terms in the y direction shown in equation 5.16. For comparison, the convection terms are plotted on the same scale as used in figures 5.14 and 5.15 for the vertical drag and body force terms. At all instances in time, the convection terms are smaller than the body force and vertical drag terms. At flow reversal ($t/\tau = 0$), the convection terms are 15% of the magnitude of the body force terms making a small contribution to the particle momentum. However, as time progresses, the convection terms become a more significant source of vertical momentum transport. From $t/\tau = 0.16$ until the next flow reversal, the convection terms are roughly 40 to 50% of the magnitude of the

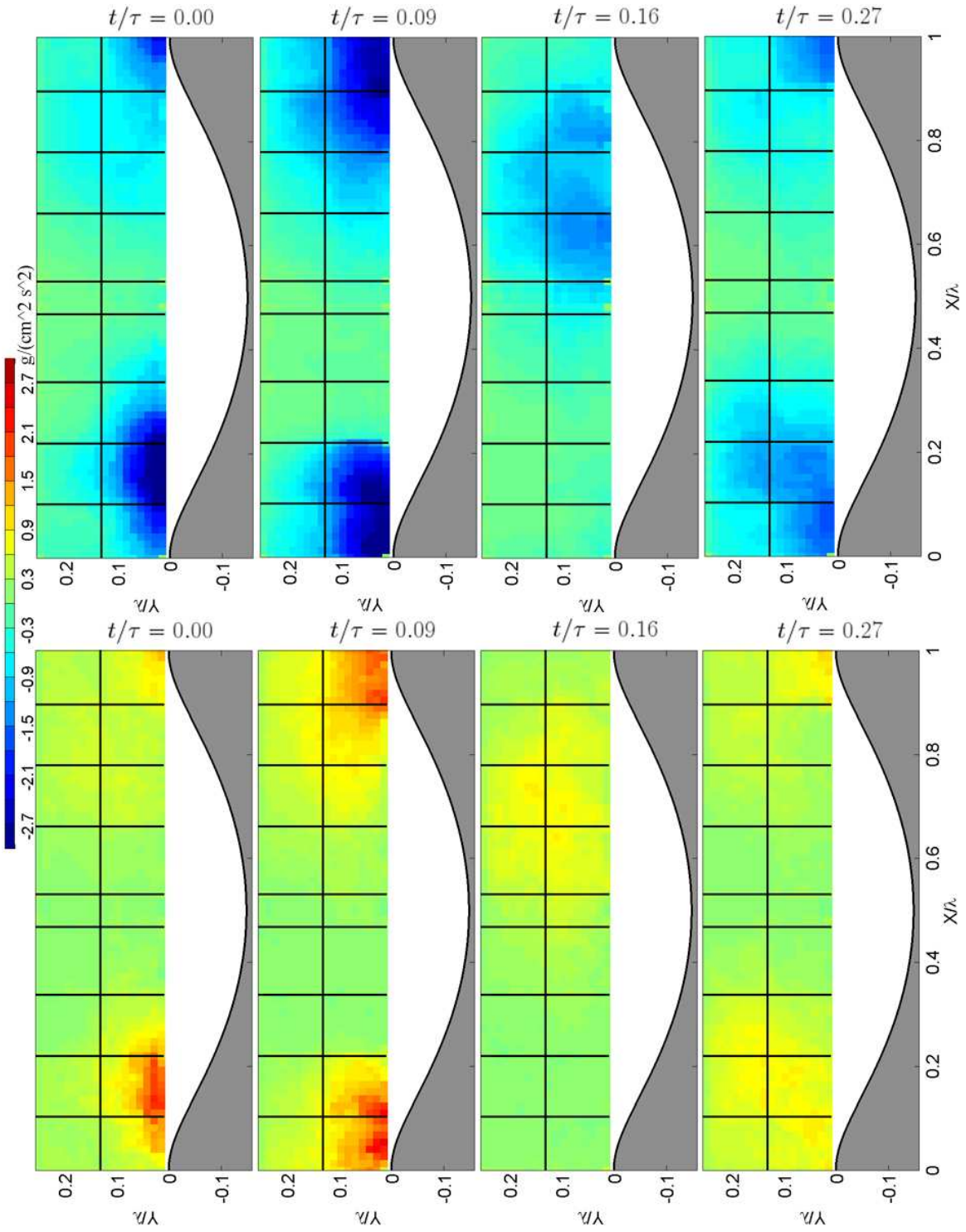

Figure 5.14: *Plots on the left are the total particle drag in the y direction, while the plots on the right are the magnitude of body forces at t/τ=0.00, 0.09, 0.16, and 0.27 with the origin located at the tip of the ripple crest. Solid black lines on each of the plots indicates the boundaries between measurement regions.*

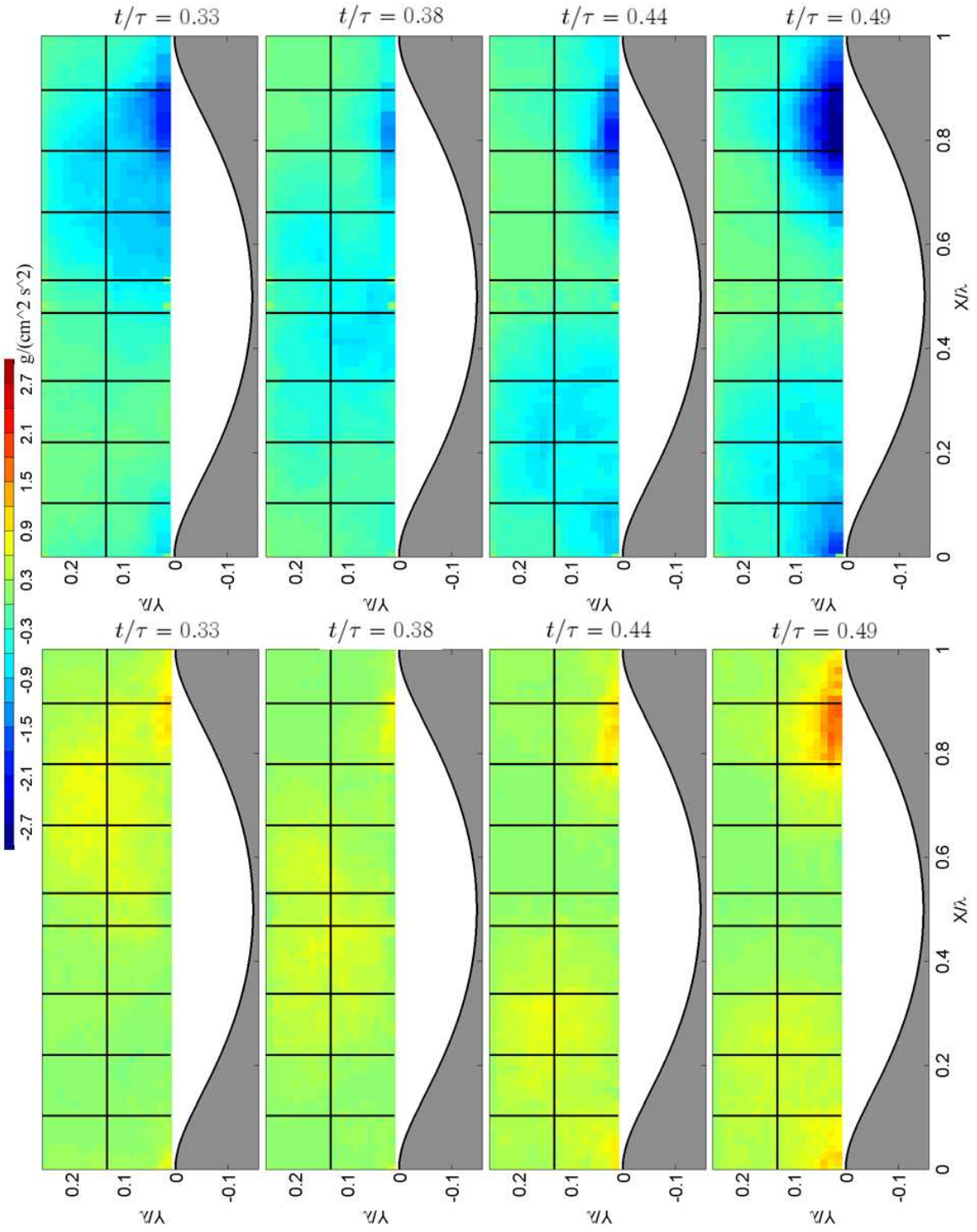

Figure 5.15: *Plots on the left are the total particle drag in the y direction, while the plots on the right are the magnitude of body forces at t/τ=0.33, 0.38, 0.44, and 0.49 with the origin located at the tip of the ripple crest. Solid black lines on each of the plots indicates the boundaries between measurement regions.*

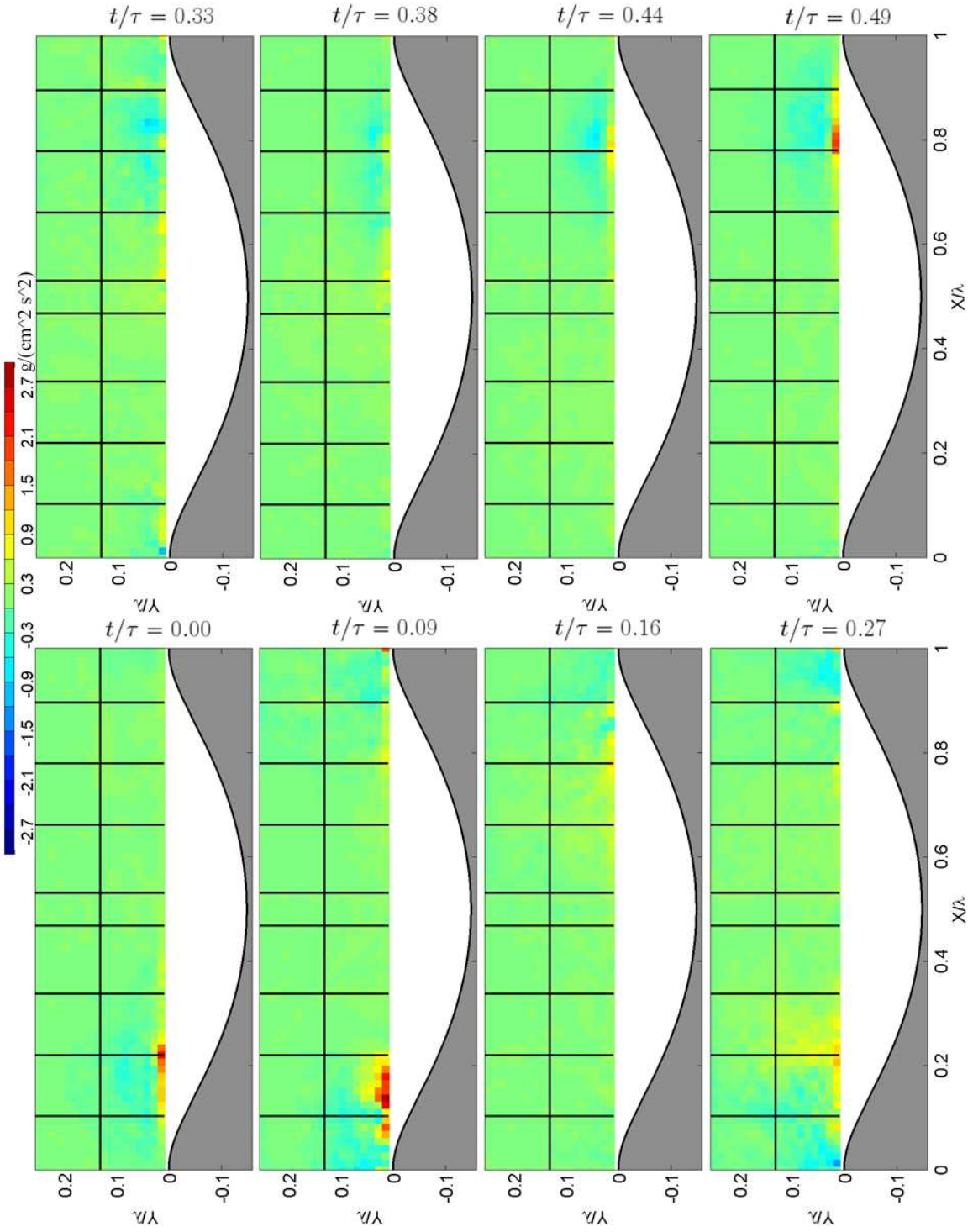

Figure 5.16: *Plots of the sum of the convection terms in the particle momentum equation in the y direction at t/τ=0.00, 0.09, 0.16, 0.27, 0.33, 0.38, 0.44, and 0.49. Solid black lines on each of the plots indicates the boundaries between measurement regions.*

body force terms for $y/\lambda < 0.1$. However, for $y/\lambda > 0.1$ the convection terms are much less significant than the body force or vertical particle drag, where the difference in magnitude between the body force and vertical drag is small.

Inspection of each term contributing to the vertical particle drag revels that terms 1, 3, 10, 14, and 18 through 20 in equation 5.5 (terms $\underbrace{-3\pi\mu D\tilde{n}\tilde{S}_y}_{1}$, $\underbrace{-3\pi\mu D\widehat{n}\tilde{S}_y}_{3}$, $\underbrace{3\pi\mu D 0.15\frac{D}{\nu}\tilde{S}_y\langle n'|S_y'^{0.687}|\rangle}_{10}$, $\underbrace{-3\pi\mu D 0.15\frac{D}{\nu}\widehat{n}\widehat{S_y}|\widehat{S_y^{0.687}}|}_{14}$, $\underbrace{-3\pi\mu D 0.15\frac{D}{\nu}\tilde{n}\langle S_y'|S_y'^{0.687}|\rangle}_{18}$, $\underbrace{-3\pi\mu D 0.15\frac{D}{\nu}\widehat{n}\langle S_y'|S_y'^{0.687}|\rangle}_{19}$, and $\underbrace{-3\pi\mu D 0.15\frac{D}{\nu}\langle n'S_y'|S_y'^{0.687}|\rangle}_{20}$ respectfully) make the most significant contributions to the vertical particle drag, each accounting for at least 10% of the drag. Of those 7 terms, all except term 20 are positive and terms 3, 19, and 20 account for 35%, 40%, and -30% of the total vertical particle drag. Two of the most significant terms for the total vertical particle drag all involve the fluctuations of the slip velocity around the mean, indicating that the turbulent fluctuations play an important role for the drag, which keeps the sediment particles suspended in the flow.

The terms that play the most important role in the particle vertical convection are terms 15, 16, 17, 18, 26, 28, and 30 in equation 5.7 (terms $\underbrace{\partial_x(\rho_p\tilde{\alpha}_p\widehat{u}_p\widehat{v}_p)}_{15}$, $\underbrace{\partial_y(\rho_p\tilde{\alpha}_p\widehat{v}_p\widehat{v}_p)}_{16}$, $\underbrace{\partial_x(\rho_p\widehat{\alpha_p}\widehat{u}_p\widehat{v}_p)}_{17}$, $\underbrace{\partial_y(\rho_p\widehat{\alpha_p}\widehat{v}_p\widehat{v}_p)}_{18}$, $\underbrace{\partial_y(\rho_p\tilde{\alpha}_p\langle v_p'v_p'\rangle)}_{26}$, $\underbrace{\partial_y(\rho_p\widehat{\alpha_p}\langle v_p'v_p'\rangle)}_{28}$, and $\underbrace{\partial_y(\rho_p\langle\alpha_p'v_p'v_p'\rangle)}_{30}$ respectfully) each accounting for at least 10% of the particle vertical convection. At flow reversal, the mean convection terms (15 through 18) are small (each approximately 7 to 10% of the total), while the fluctuating terms (26, 28, and 30) are the main contributors. After the particle cloud moves over the ripple and begins to transverse down the lee side at $t/\tau = 0.156$, the cyclic mean terms become

dominate and the Particle Reynolds stress become insignificant until the next flow reversal.

Chapter 6

Conclusion

Sediment transport plays a key role in the prediction of coastal flooding, beach erosion and dispersal of man-man pollutants. Because of large concentrations of sediment near the bed, the multi-phase flow of sea water and sediment near the bed may often be two-way coupled, depending on the parameters of the forcing and sediment size. In deriving multi-phase two-way coupled momentum equations, the interaction terms between the phases contain the conditional slip velocity between the phases. Previous experiments have measured either the carrier phase or the dispersed phase velocity, but not simultaneously, thus leaving a direct indication of this potentially important coupling unknown. Highly resolved detailed measurements of simultaneous fluid and particle information are necessary to better understand how the fluid and particle phases interact with each other. This thesis presents the first measurements of this type to be applied to an oscillating flow with a mobile bed, accomplished through the application of a novel two-phase Particle Image Velocimetry technique near the sediment bed.

By examining the results of the measurement technique in chapter 4 and the flow field measurements in chapter 5, serval conclusions can be obtained, namely:

1. Concentration measurements using light intensity as an indicator of concentration detection require a detailed understanding of how light scattered in

the measurement region affects the scattered light intensity and hence the effective measurement volume. Careful consideration of various particle illumination sources such as the laser light sheet, light scattering from other particles, and light scattering from the reflective bed must be understood to eliminate bias in the detectability of sediment particles. The effects of these sources on the intensity and measurement volume are often overlooked, and features such as the reflective sediment bed were found to effectively increase the measurement volume by as much as 40% for the optical setup used in this experiment. The resulting measurement volume can not be simply described using traditional measures of the sheet width such as the 1/e intensity. By accounting for the various illumination effects on the sediment particles, the concentration was found to be measured within $\pm 12\%$, which was limited by the coarse measure of the independent reference concentration, rather than the optical technique itself.

2. Measurements of the coherent and turbulent stress integrated over the wavelength show that at flow reversal the contributions from each source are similar in magnitude, however other portions of the wave cycle are dominated by the coherent stress. Qualitative observations of the ripple crest show that the crest profile is modified by accelerating flow over the ripple. Using the inflection points in the fluid streamlines before boundary layer separation as a qualitative indicter of the ripple crest position shows that large changes in the coherent stress occur as the ripple crest is being reoriented by the fluid. I postulate

that the reorientation of the ripple crest crest may have a significant impact on the over all stress of the bed as a function of time.

3. Simultaneous measurements of the fluid velocity, particle velocity, and sediment concentration reveal that vortical structures ejected from the bed at flow reversal play an important role in the dynamics of sediment transport. The adverse pressure gradient during flow deceleration causes the boundary layer to separate from the top of the ripple crest which in turn causes a turbulent wake region to form behind to ripple. Sediment particles are entrained into the flow and suspended by the large turbulent kinetic energy and Reynolds stress that are created in the separated flow region. At flow reversal, a large vortex is ejected outward into the flow, ejecting sediment over the ripple crest. Comparison of the vertical particle drag and the reduced gravity indicate that the reduced gravity is 30% larger than the vertical particle drag at flow reversal. It is likely that the other neglected terms in the particle force coupling equation account for the balance of this difference. Triple deposition and calculation of the vertical particle drag terms indicate that the turbulent motion of the particles is the primary contributor to the drag at flow reversal. As the flow accelerates, a sediment cloud suspended by decaying turbulence convects over the ripple crest, following the contours of the sediment bed. When the sediment cloud traverses over the ripple crest at $t/\tau = 0.16$, the turbulence and sediment concentration decay significantly from their magnitudes at flow reversal. The reduced gravity is 15% larger than the vertical particle drag

from $0.16 < t/\tau < 0.5$, while inspection of the vertical particle drag terms indicate that the mean drag terms make a similar contribution to the vertical drag as the ensemble fluctuating drag terms.

4. The plots of the time averaged fluid velocity, particle velocity, and vertical sediment flux reveal that two counter-rotating cells eject sediment outward into the flow near the ripple crest, which recirculates in the flow with a large negative flux toward the bed in the valley between the ripples. Because the bed shape is a steady state formation, the streamlines for the fluid and sediment must form closed orbitals in the region below the ripple crest between the ripples that was not measured.

5. Calculation of the resulting terms in the triple decomposed time-average conservation mass revealed that the cyclic mean terms are similar in magnitude as the long-time averaged terms, while the ensemble fluctuating terms are an order of magnitude smaller. In order to model the sediment flux on the scale of the experiment, sediment flux models must account for the cyclic nature of the mass flux because of its significant contribution to the conservation of mass.

6. Previous researchers have found that the time averaged sediment concentration from $0 < y < 2\eta$ over the ripple crest can be modeled using a diffusive equation. The decay length between correlations by Neilsen (1982) and Davies and Thorne (2005) compare with in $\pm 3.2\%$ of the exponential fit to the concentration data from the UMD experiments. While time-averaged concentration

over the ripple crest is well described by a diffusive flux equation, the ensemble-averaged concentration clearly shows distinct turbulent structures suspending the sediment in specific regions of the flow flied implying that the distribution of concentration is not by a diffusive process. The largest uncertainty in using these correlations as a predictive model is determining the reference concentration of sediment at the ripple crest. Neilsen's reference concentration over predicted the concentration profile by a 128% as compared to the UM experimental data, while Davies and Thorne's correction over predicted the concentration by .7%. To make these correlations more predictive requires to correlations to better account for the localized sediment flux at specific instances in the cycle.

Appendix A: Experimental facility drawings

(all dimensions in mm unless otherwise specified)

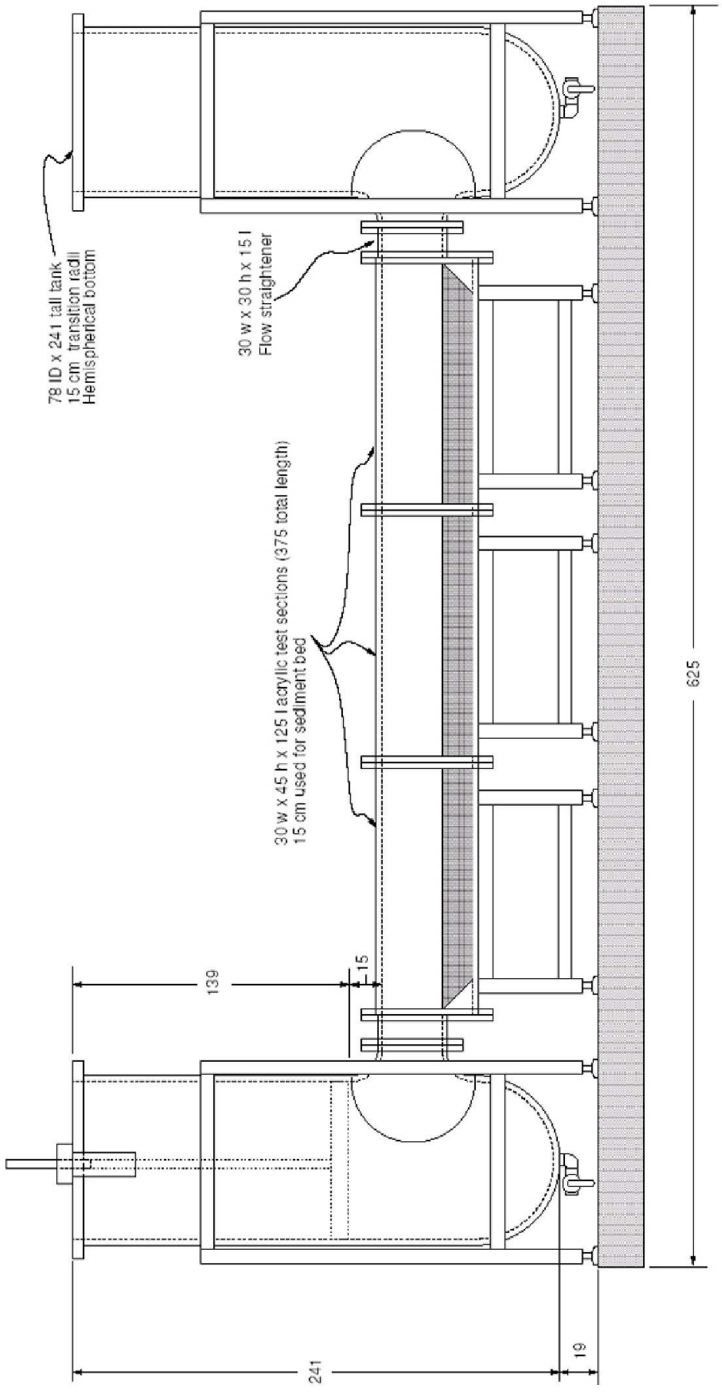
78 ID x 241 tall tank
15 cm transition radii
Hemispherical bottom
30 w x 30 h x 15 l
Flow straightener
30 w x 45 h x 125 l acrylic test sections (375 total length)
15 cm used for sediment bed
139
15
625
241
19

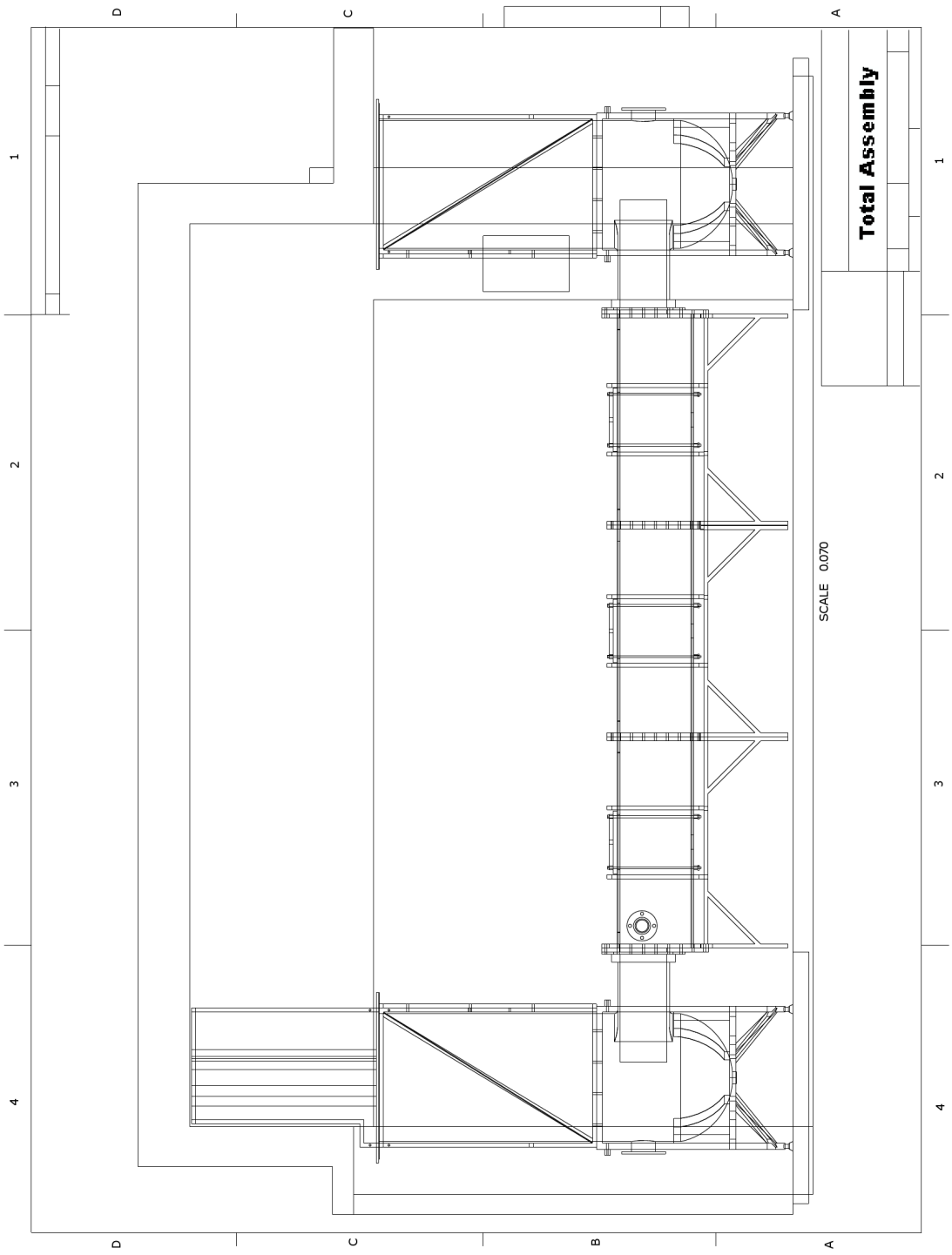
Total Assembly
SCALE 0.070
D
C
B
A
1
2
3
4

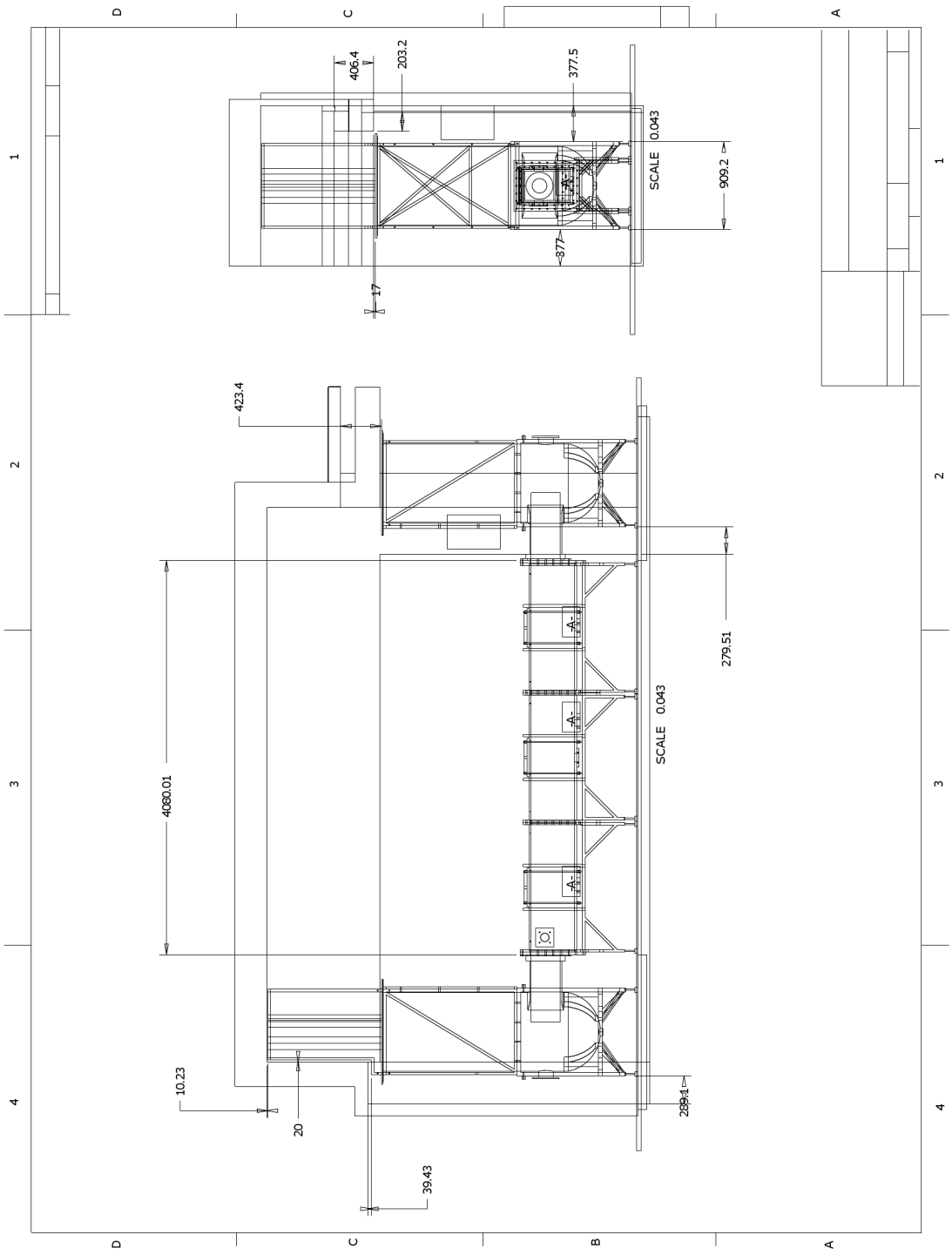
406.4
203.2
377.5
0.043
SCALE
909.2
377
17
423.4
279.51
4080.01
A-
A-
A-
SCALE 0.043
10.23
20
39.43
289.1

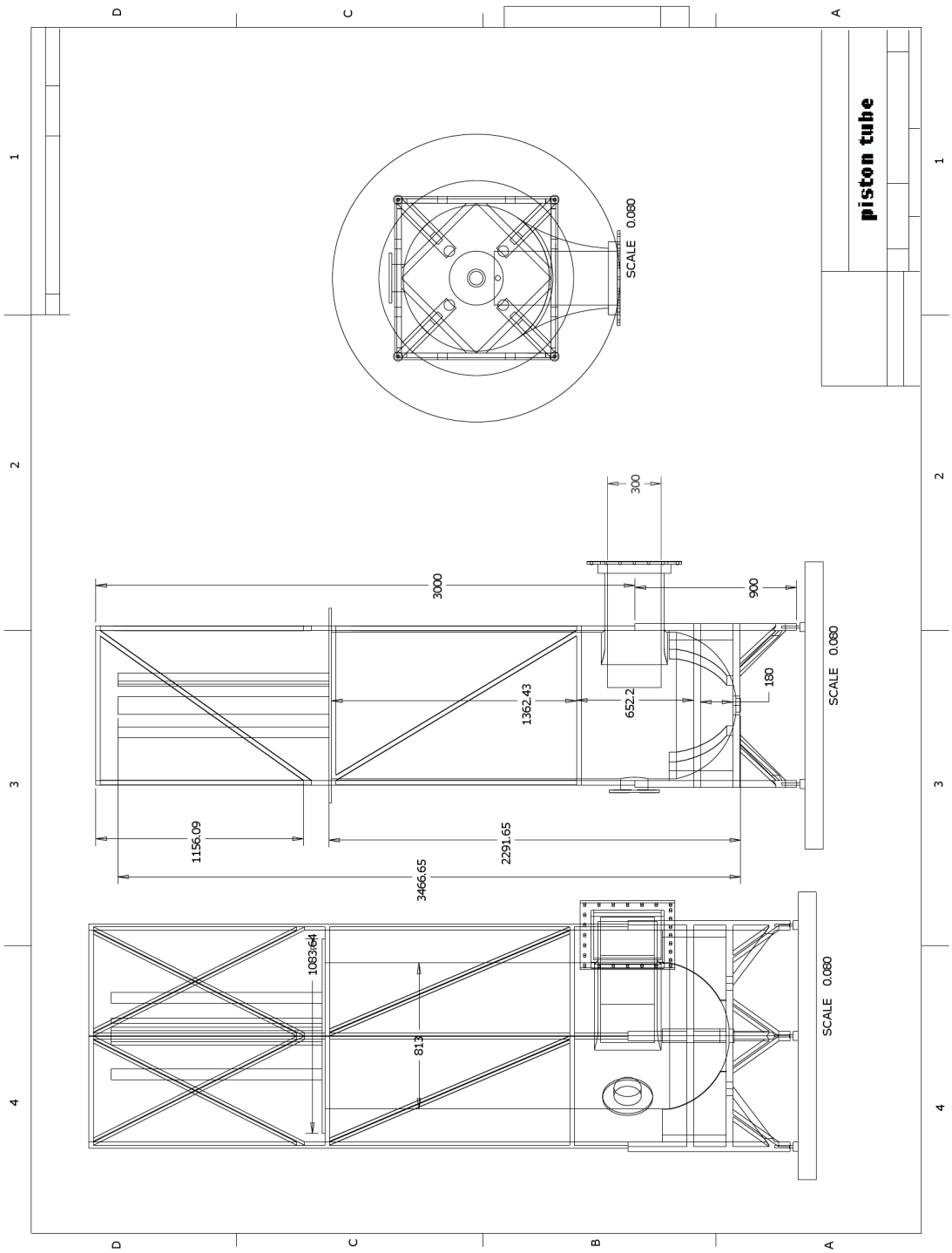
piston tube
SCALE 0.080
300
3000
900
180
1362.43
652.2
1156.09
2291.65
3466.65
1083.64
813
SCALE 0.080
SCALE 0.080

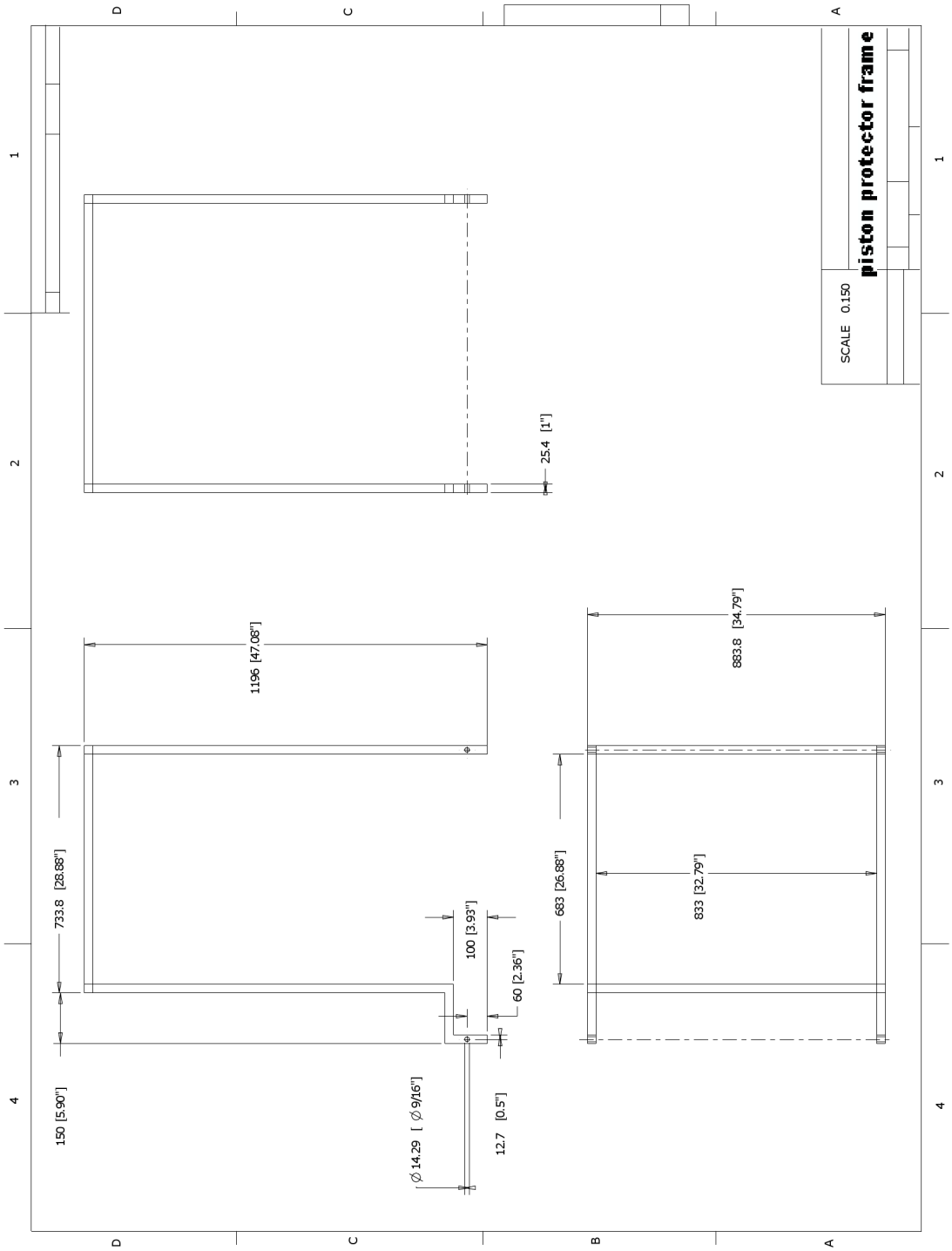
piston protector frame
SCALE 0.150
25.4 [1"]
1196 [47.08"]
733.8 [28.88"]
150 [5.90"]
100 [3.93"]
60 [2.36"]
Ø14.29 [Ø9/16"]
12.7 [0.5"]
883.8 [34.79"]
683 [26.88"]
833 [32.79"]

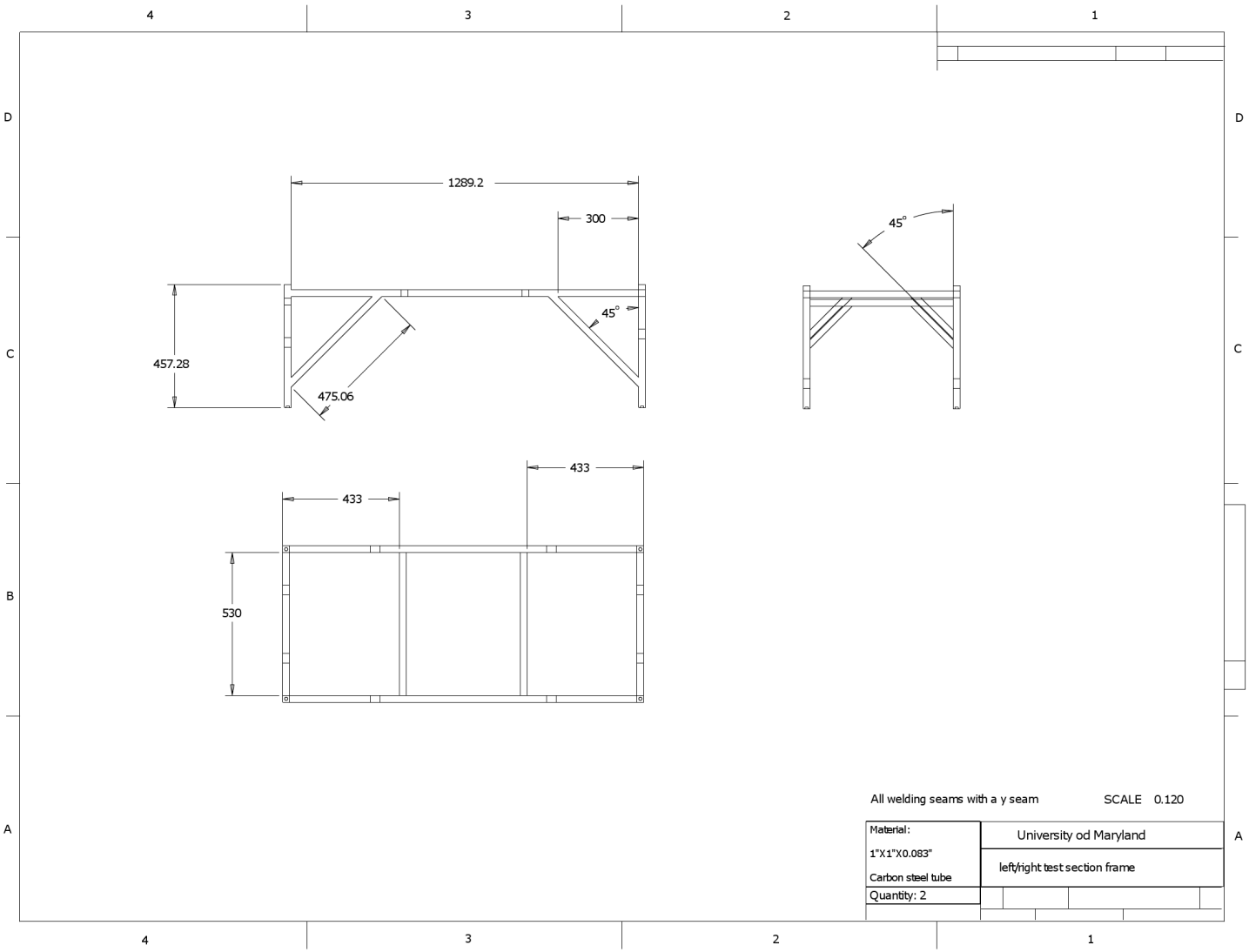
4
3
2
1
D
C
B
A
1289.2
300
45°
457.28
475.06
45°
433
433
530
All welding seams with a y seam
SCALE 0.120
Material:
1"X1"X0.083"
Carbon steel tube
Quantity: 2
University od Maryland
left/right test section frame

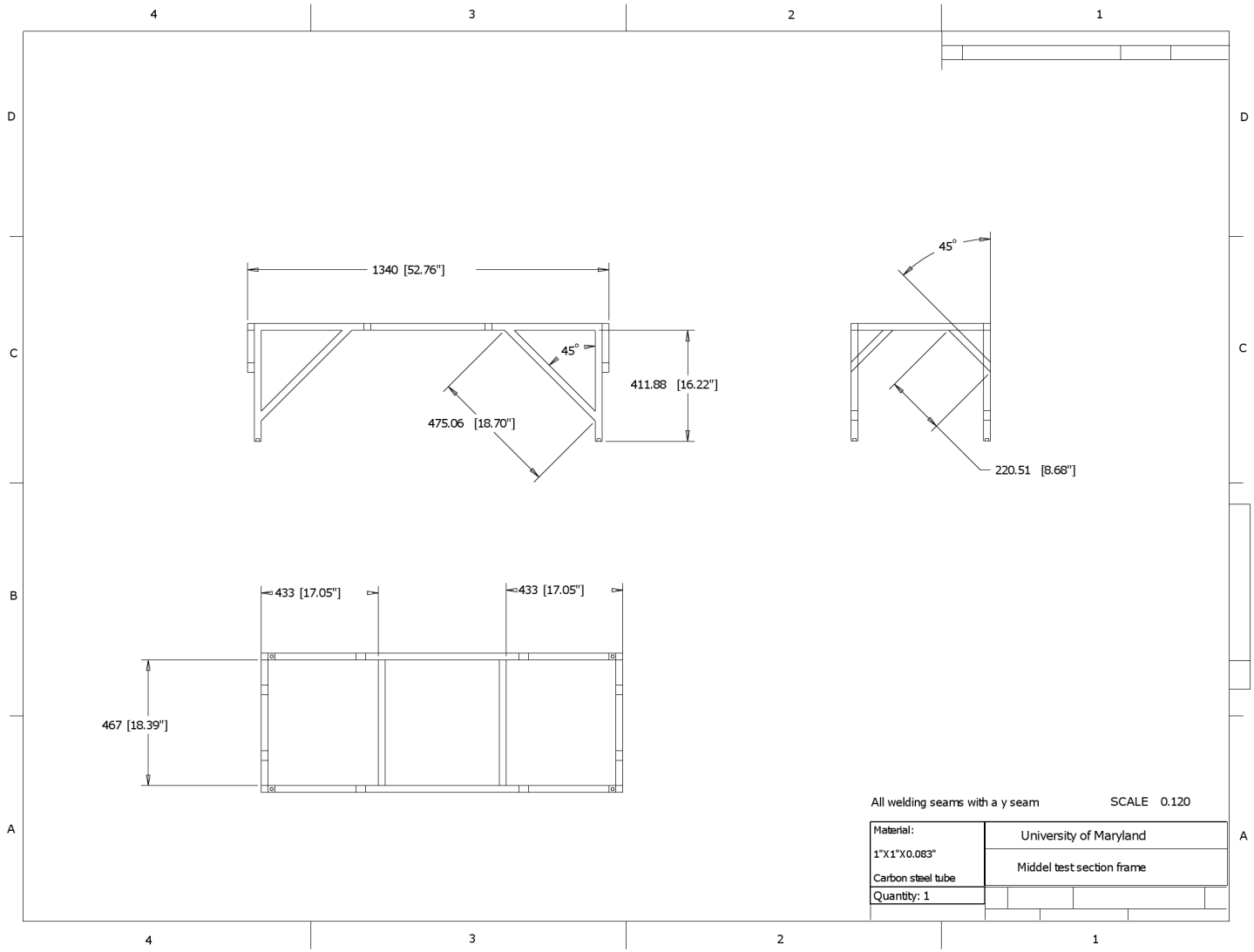
4
3
2
1
D
C
B
A
1340 [52.76"]
45°
411.88 [16.22"]
475.06 [18.70"]
45°
220.51 [8.68"]
433 [17.05"]
433 [17.05"]
467 [18.39"]
All welding seams with a y seam
SCALE 0.120
Material:
1"X1"X0.083"
Carbon steel tube
Quantity: 1
University of Maryland
Middel test section frame

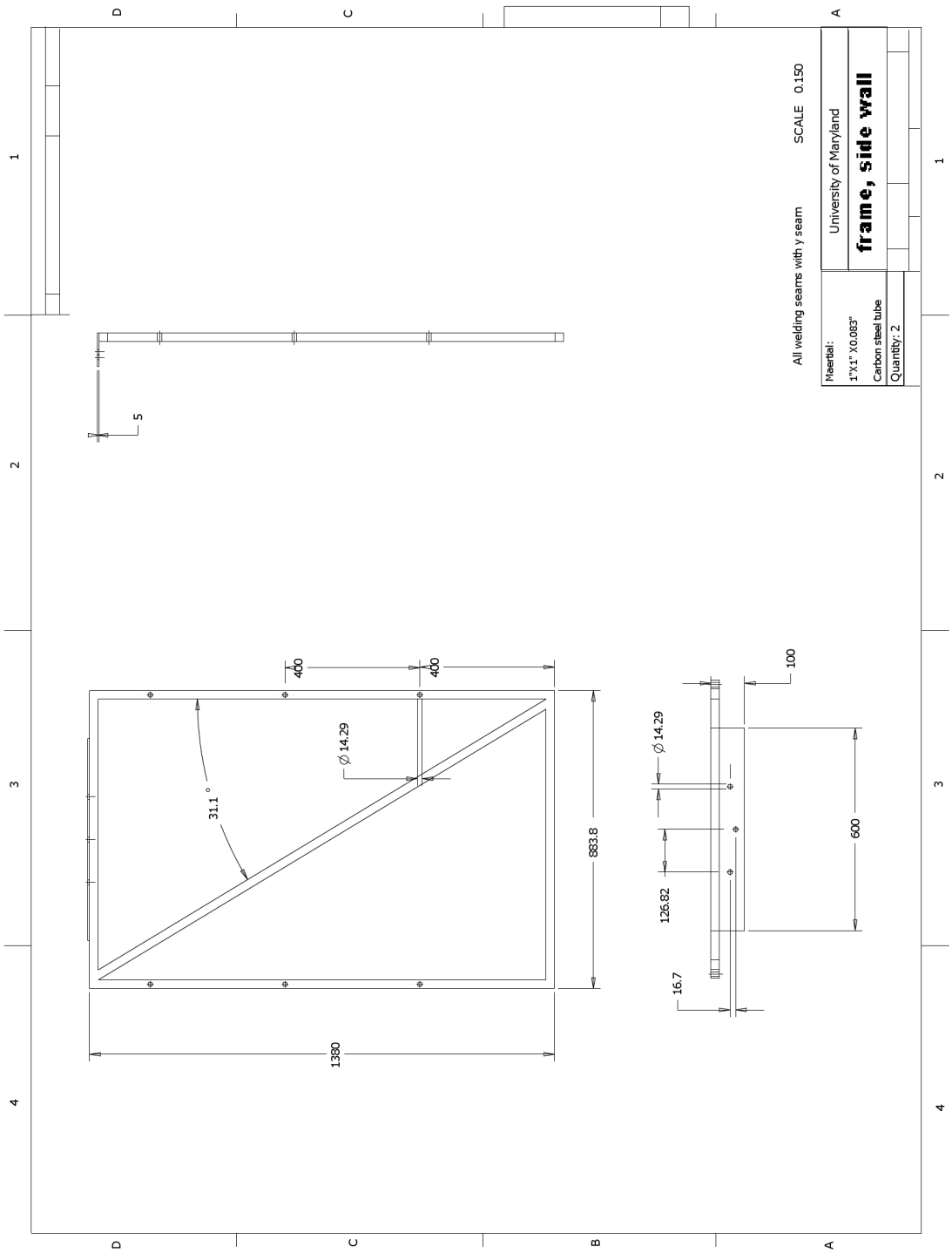
All welding seams with y seam
SCALE 0.150
University of Maryland
frame, side wall
Maertial:
1"X1" X0.083"
Carbon steel tube
Quantity: 2
5
400
400
∅ 14.29
31.1 °
883.8
1380
100
∅ 14.29
126.82
600
16.7

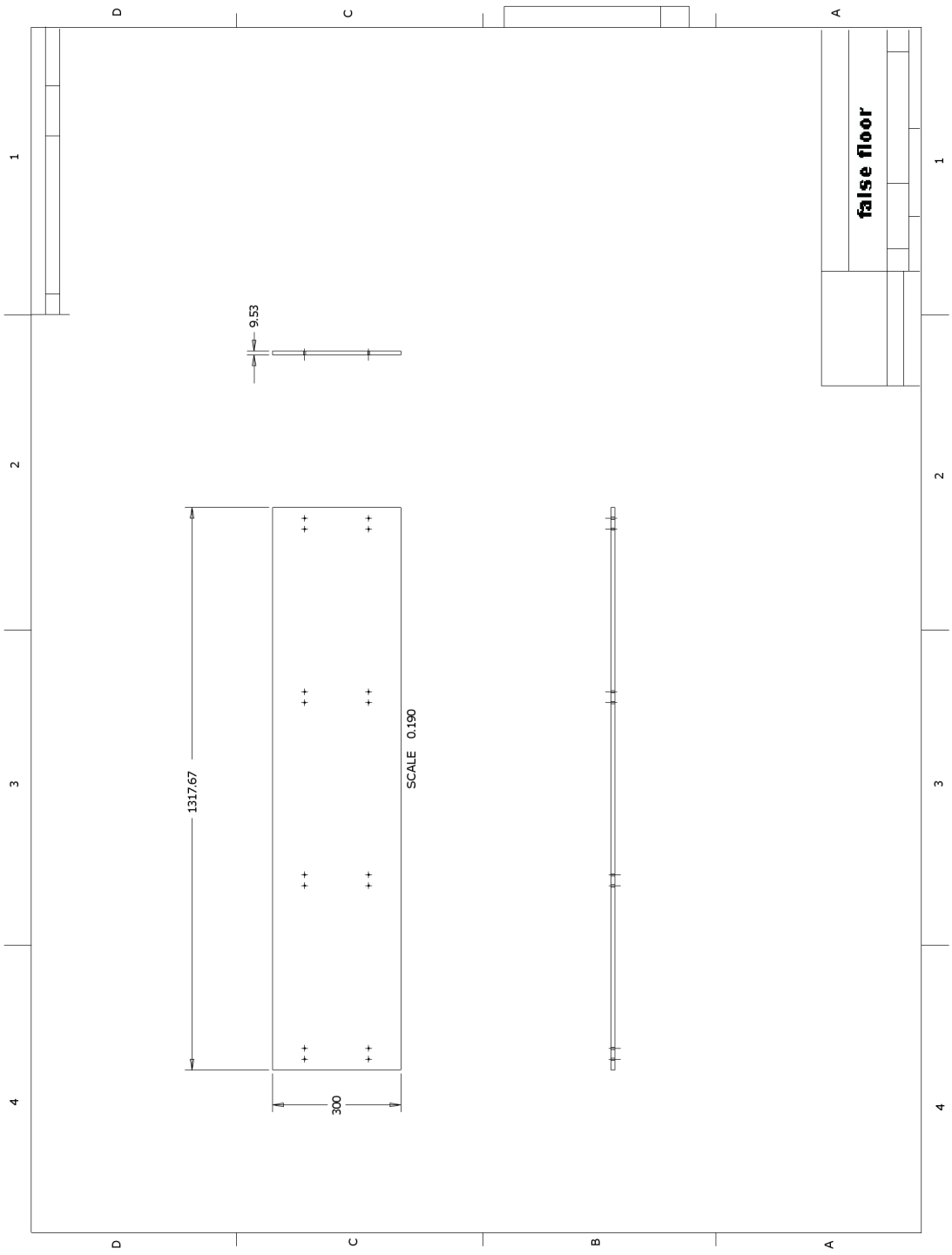
false floor
9.53
1317.67
SCALE 0.190
300

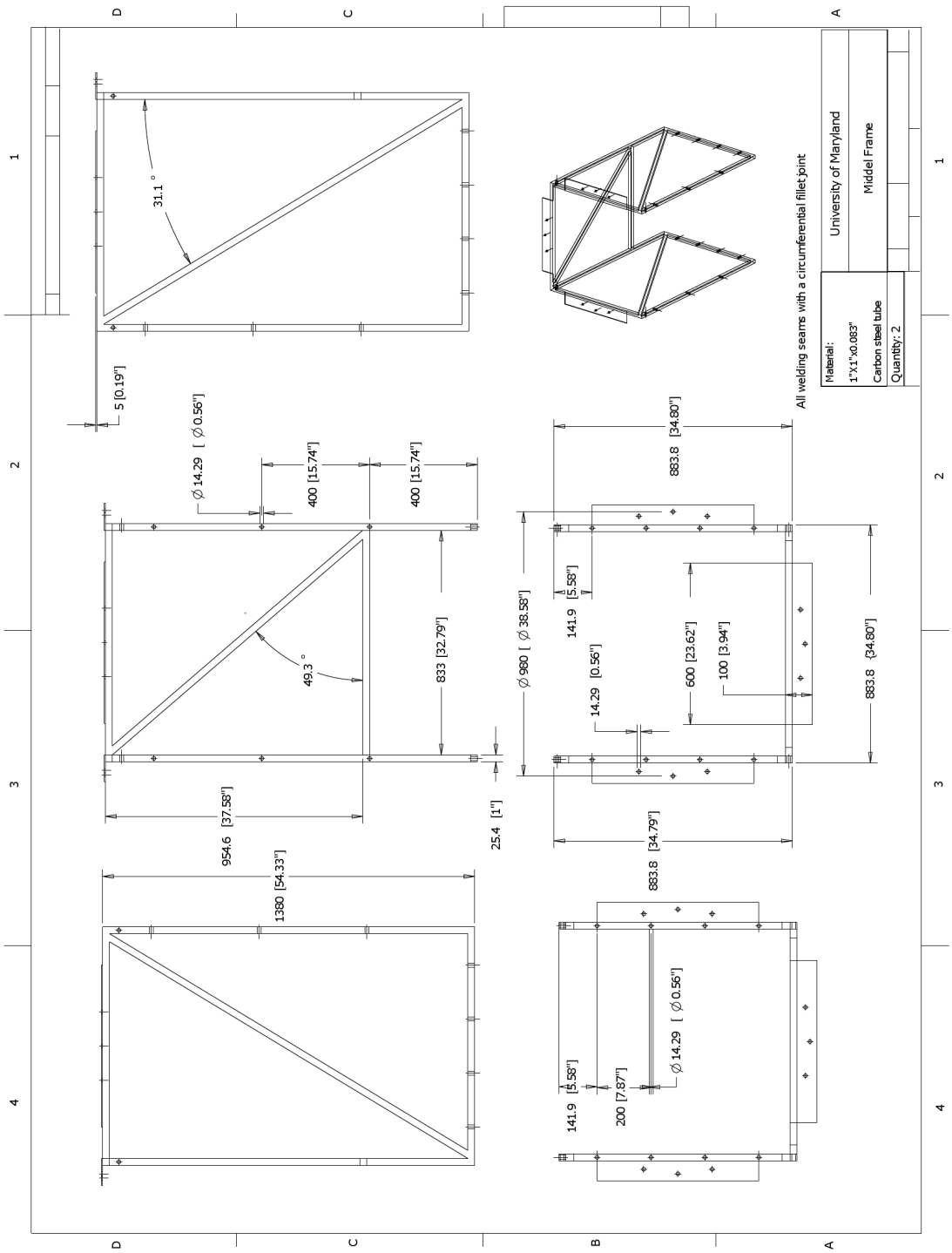
31.1 °
5 [0.19"]
∅ 14.29 [∅0.56"]
400 [15.74"]
400 [15.74"]
49.3 °
833 [32.79"]
954.6 [37.58"]
1380 [54.33"]
25.4 [1"]
883.8 [34.80"]
∅ 980 [∅ 38.58"]
141.9 [5.58"]
14.29 [0.56"]
600 [23.62"]
100 [3.94"]
883.8 [34.80"]
883.8 [34.79"]
141.9 [5.58"]
200 [7.87"]
∅ 14.29 [∅0.56"]
All welding seams with a circumferential fillet joint
Material:
1"X1"X0.083"
Carbon steel tube
Quantity: 2
University of Maryland
Middel Frame

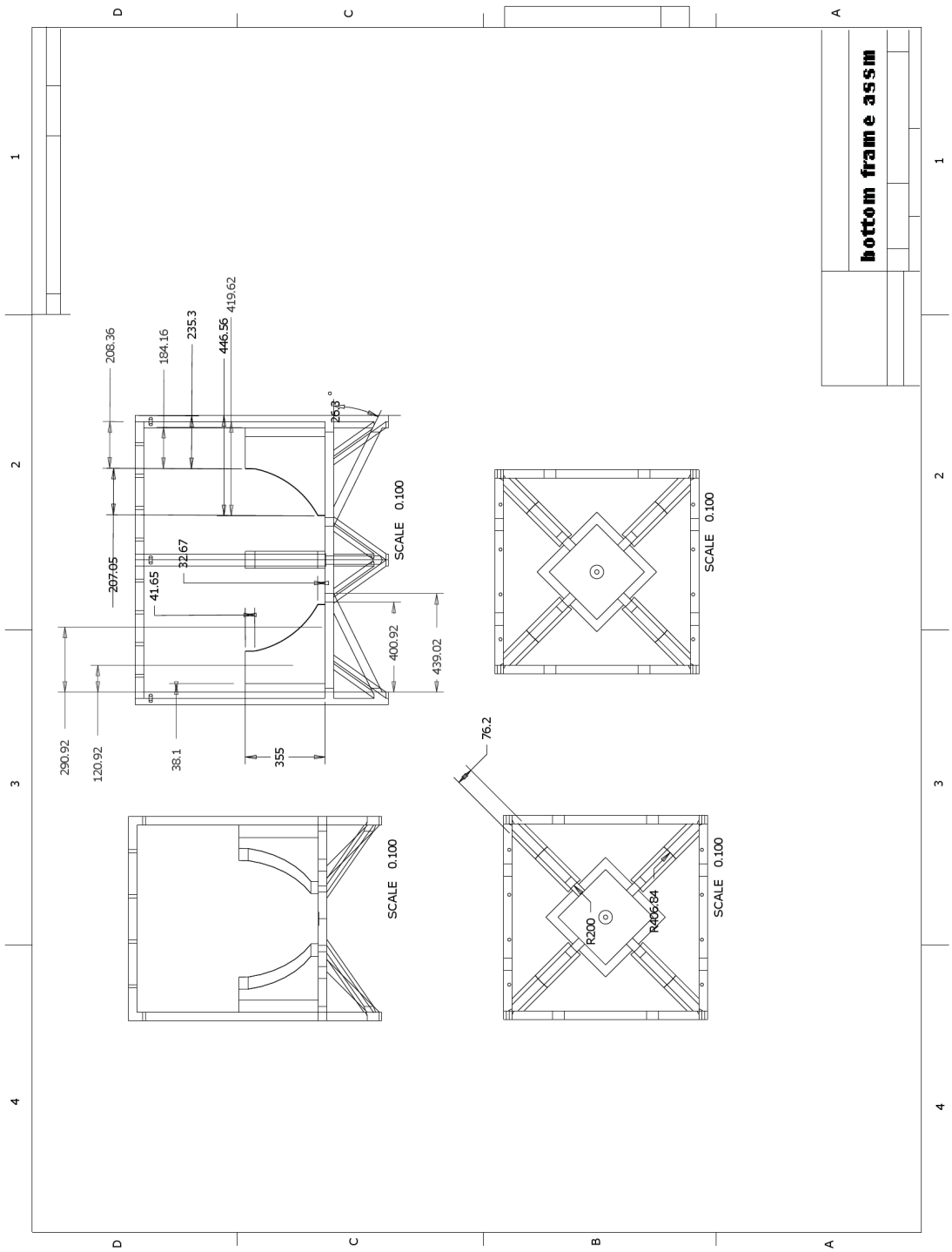
bottom frame assm
SCALE 0.100
SCALE 0.100
SCALE 0.100
SCALE 0.100
208.36
184.16
235.3
446.56
419.62
26.0 °
207.05
32.67
41.65
400.92
439.02
290.92
120.92
38.1
355
76.2
R200
R406.84

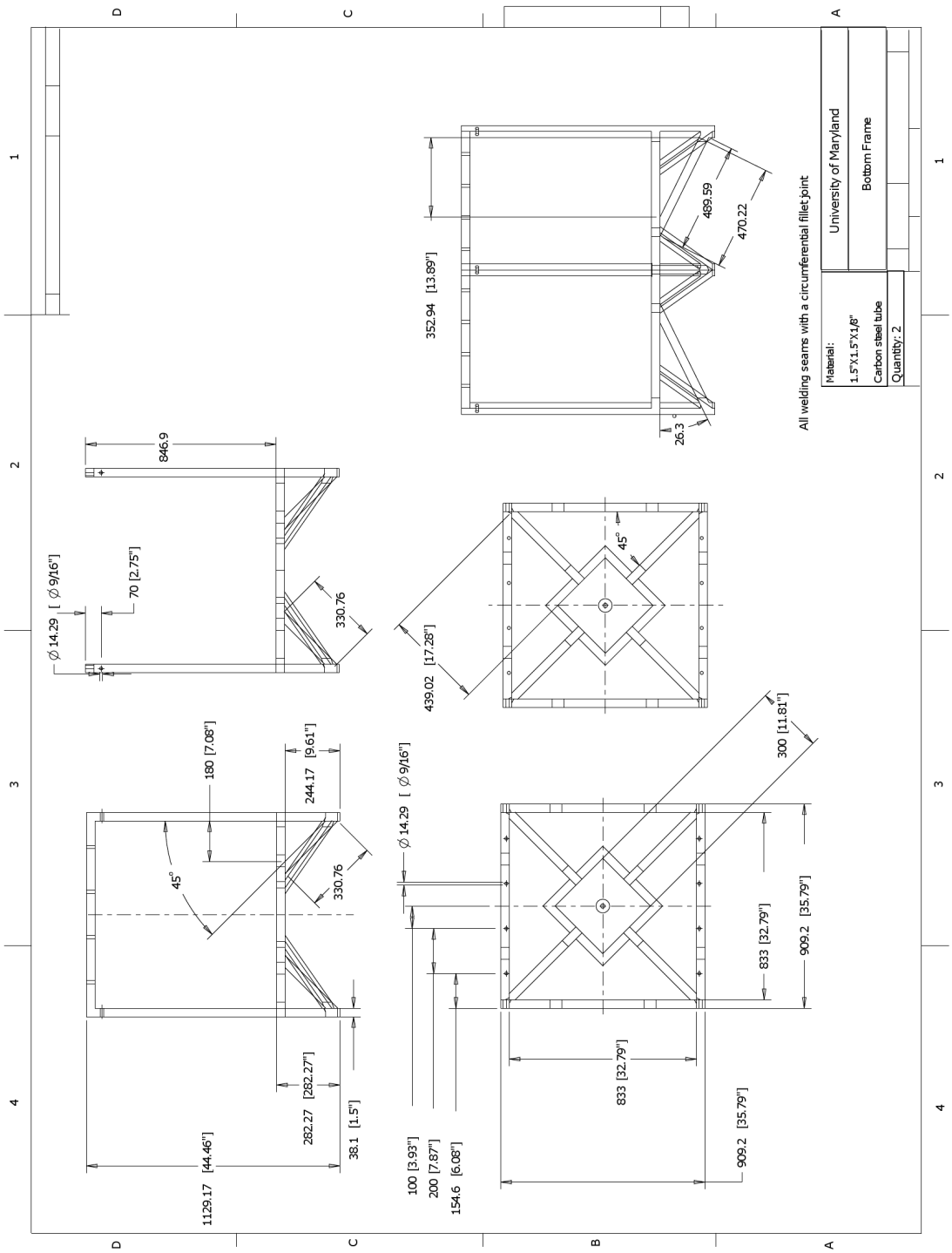
All welding seams with a circumferential fillet joint
University of Maryland
Bottom Frame
Material:
1.5"X1.5"X1/8"
Carbon steel tube
Quantity: 2
352.94 [13.89"]
499.59
470.22
26.3
846.9
70 [2.75"]
Ø 14.29 [Ø 9/16"]
330.76
45°
439.02 [17.28"]
180 [7.08"]
244.17 [9.61"]
300 [11.81"]
833 [32.79"]
909.2 [35.79"]
282.27 [282.27"]
38.1 [1.5"]
1129.17 [44.46"]
100 [3.93"]
200 [7.87"]
154.6 [6.08"]

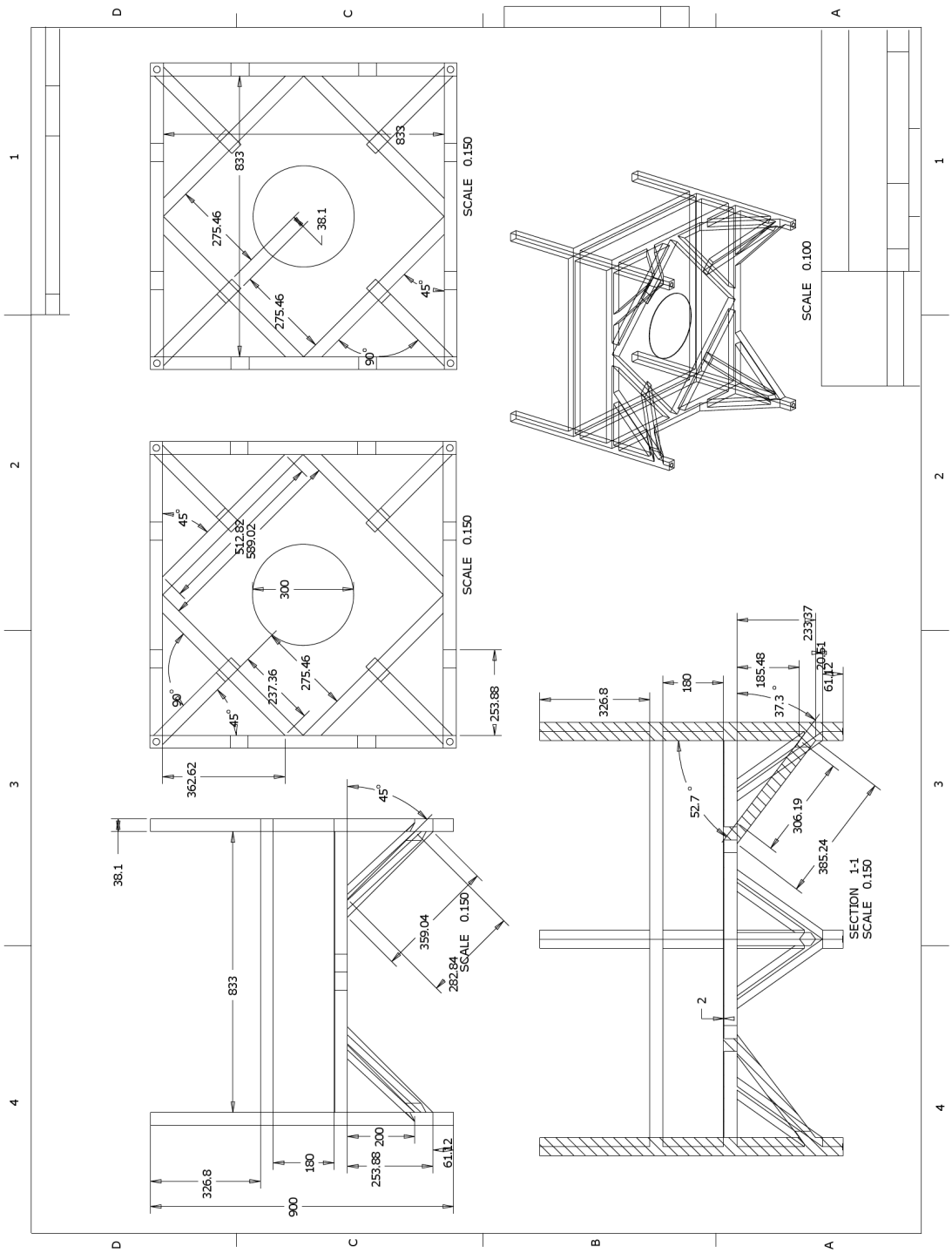
SCALE 0.150
833
833
275.46
38.1
275.46
45°
90°
SCALE 0.100
SCALE 0.150
45°
512.82
589.02
300
90°
45°
237.36
275.46
253.88
362.62
45°
38.1
833
359.04
0.150
SCALE
282.84
326.8
180
253.88
200
61.12
900
326.8
180
185.48
37.3 °
233.37
20.91
61.12
52.7 °
306.19
385.24
SECTION 1-1
SCALE 0.150
2

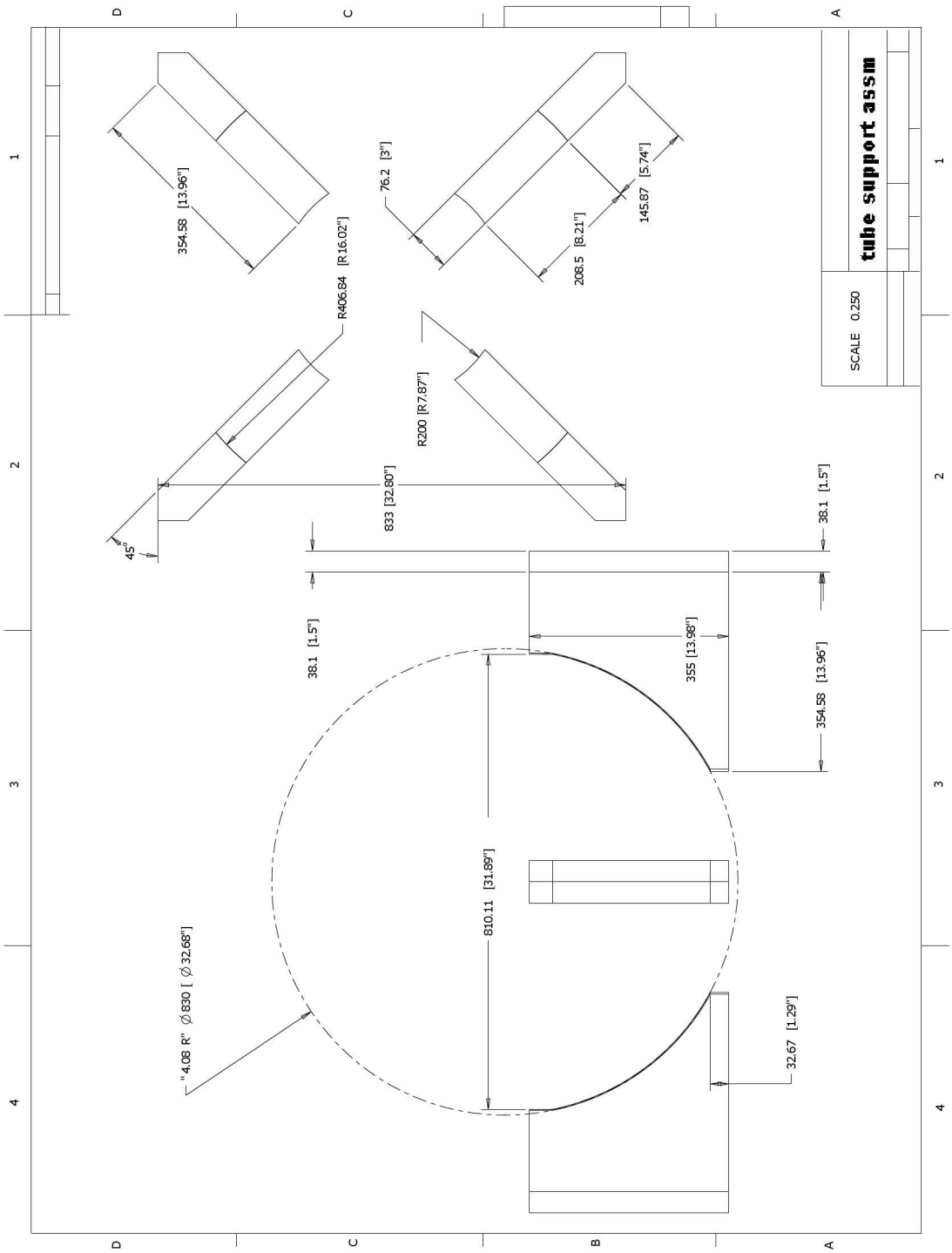
tube support assm
SCALE 0.250
354.58 [13.96"]
R406.84 [R16.02"]
45°
833 [32.80"]
R200 [R7.87"]
76.2 [3"]
145.87 [5.74"]
208.5 [8.21"]
38.1 [1.5"]
38.1 [1.5"]
355 [13.98"]
354.58 [13.96"]
810.11 [31.89"]
"4.08 R" Ø830 [Ø32.68"]
32.67 [1.29"]

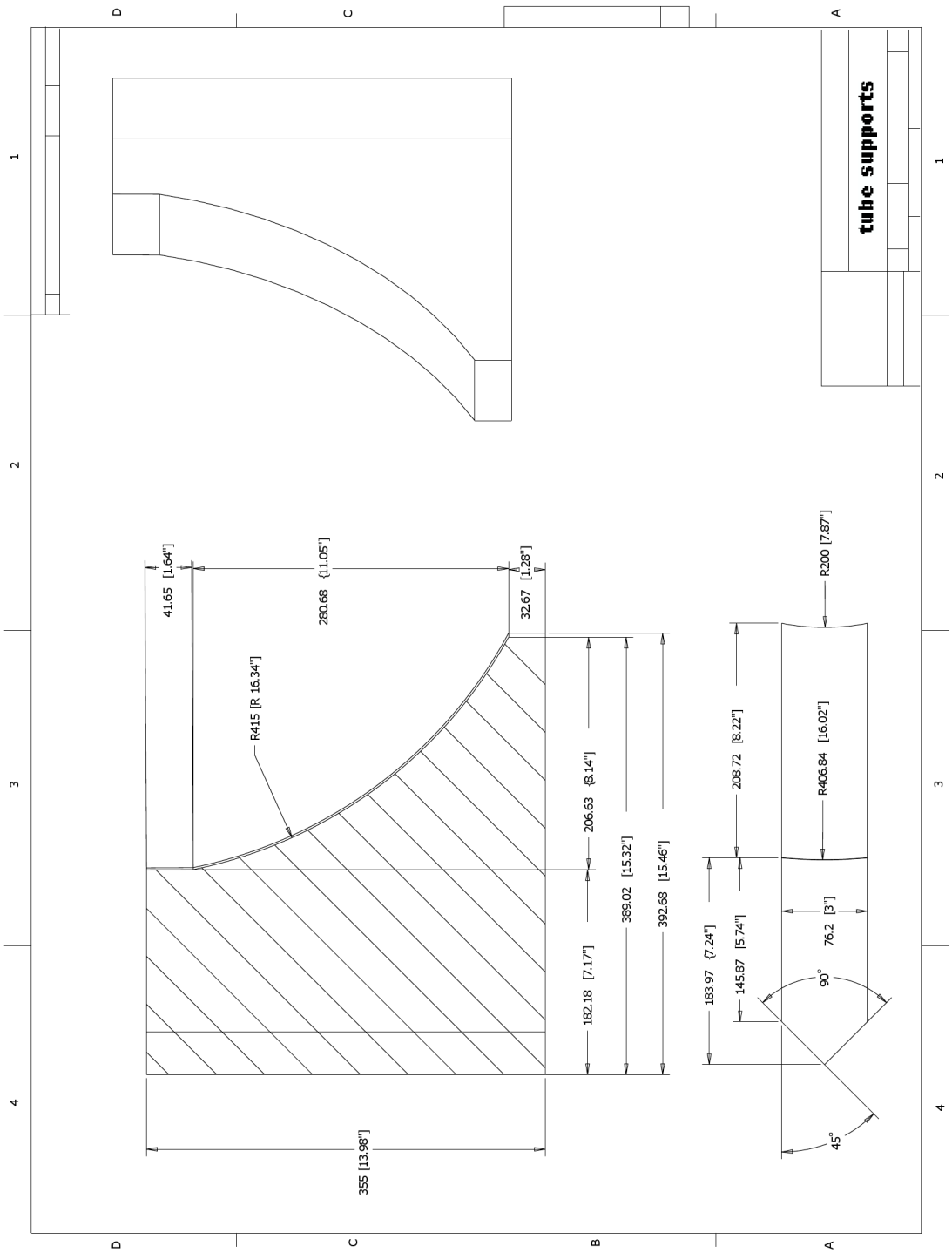
tube supports
41.65 [1.64"]
280.68 [11.05"]
32.67 [1.28"]
R415 [R 16.34"]
206.63 [8.14"]
389.02 [15.32"]
392.68 [15.46"]
182.18 [7.17"]
355 [13.98"]
R200 [7.87"]
208.72 [8.22"]
R406.84 [16.02"]
183.97 [7.24"]
145.87 [5.74"]
76.2 [3"]
90°
45°

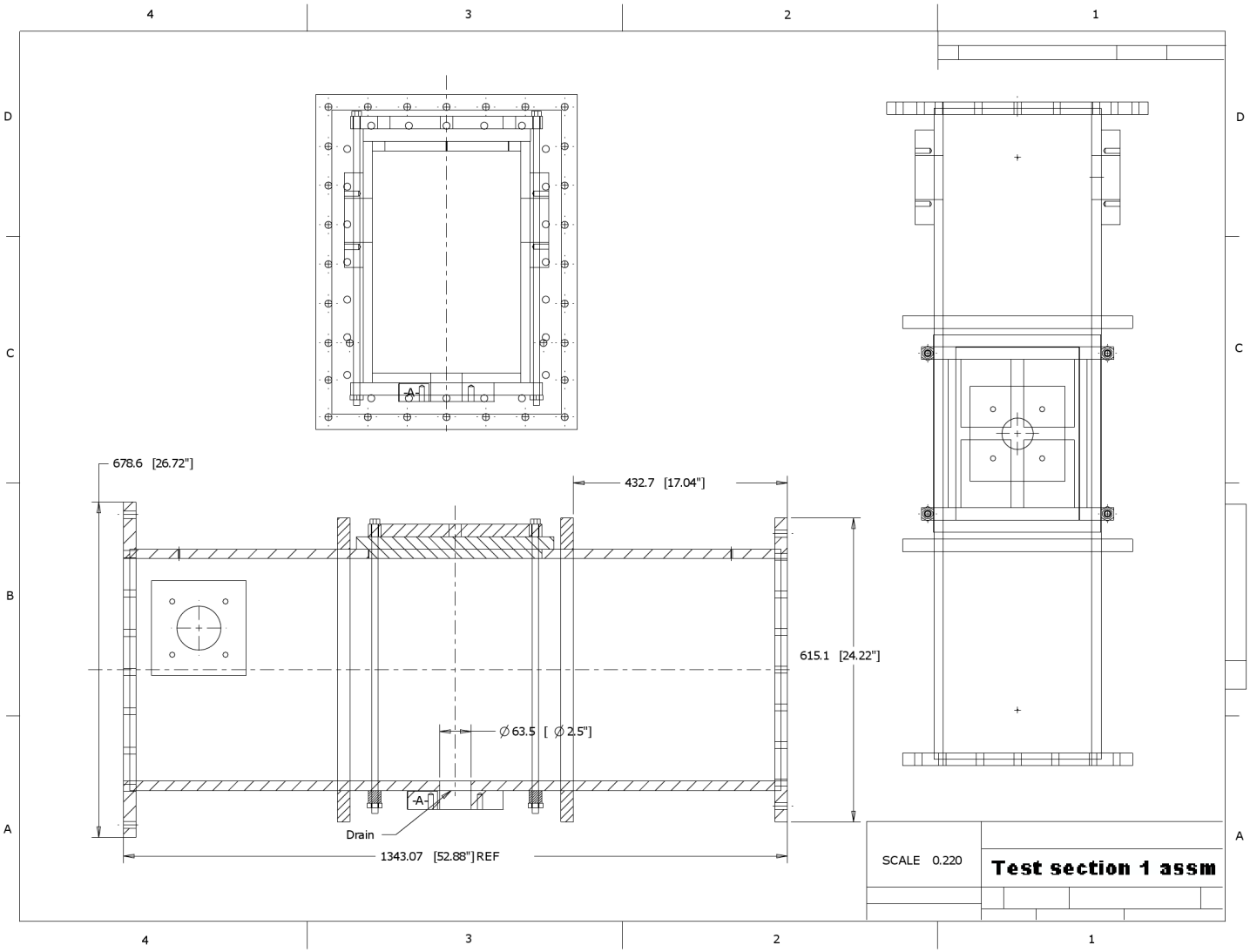
4
3
2
1
D
C
B
A
678.6 [26.72"]
432.7 [17.04"]
615.1 [24.22"]
Ø 63.5 [Ø 2.5"]
Drain
1343.07 [52.88"] REF
SCALE 0.220
Test section 1 assm

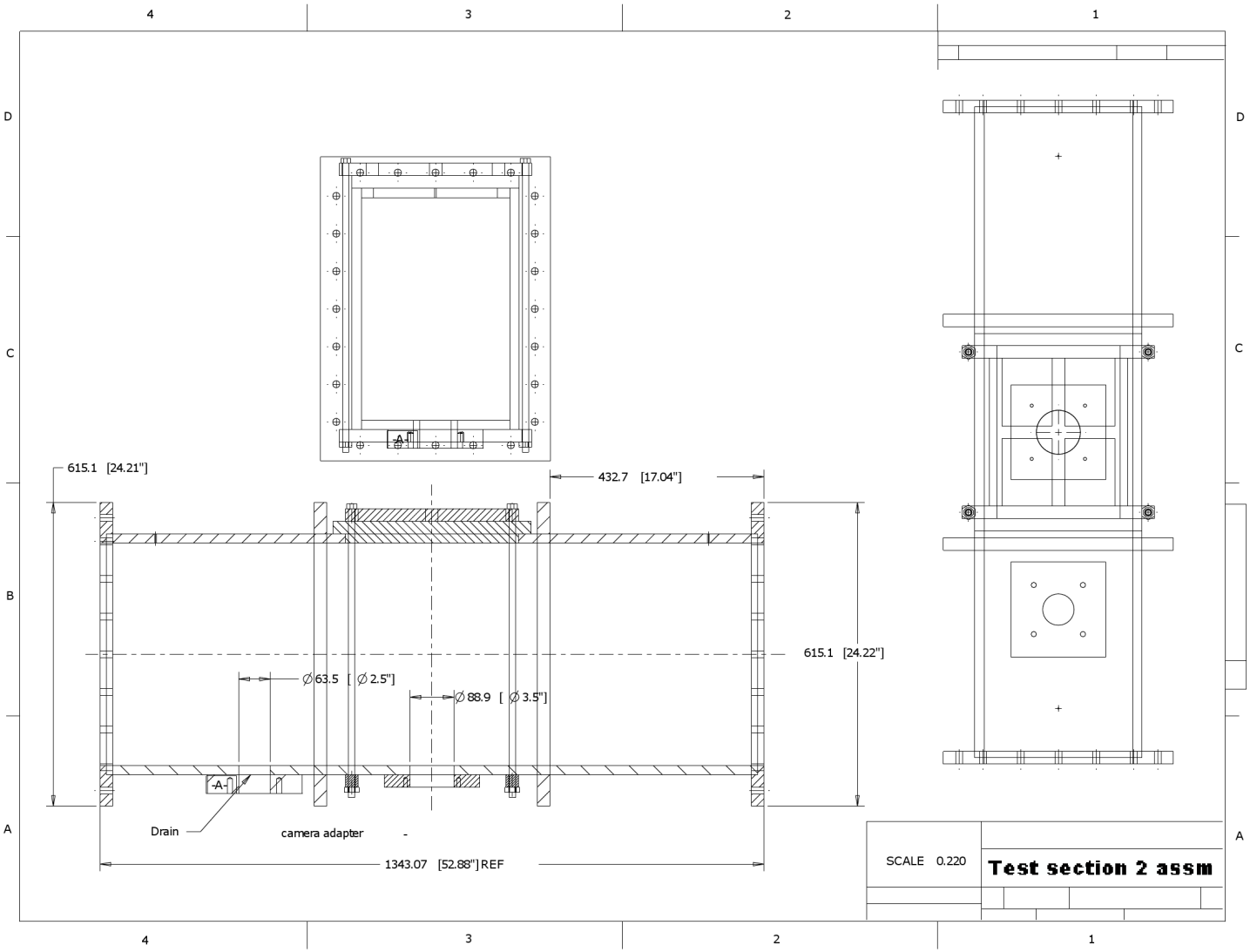
4
3
2
1
D
C
B
A
615.1 [24.21"]
432.7 [17.04"]
615.1 [24.22"]
Ø63.5 [Ø2.5"]
Ø88.9 [Ø3.5"]
-A-
Drain
camera adapter
1343.07 [52.88"] REF
SCALE 0.220
Test section 2 assm

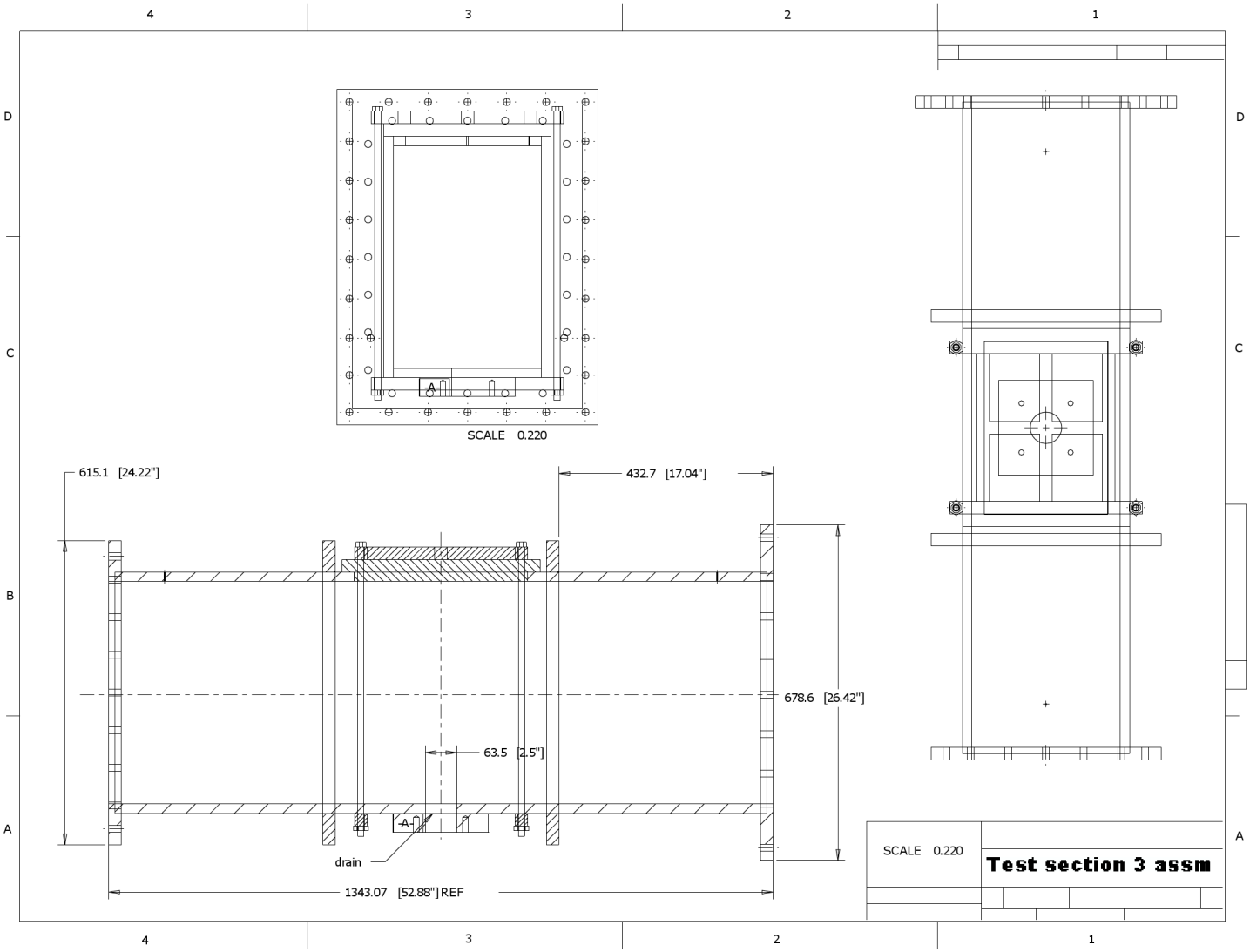
4
3
2
1
D
C
B
A
-A-
SCALE 0.220
615.1 [24.22"]
432.7 [17.04"]
678.6 [26.42"]
63.5 [2.5"]
drain
1343.07 [52.88"] REF
SCALE 0.220
Test section 3 assm

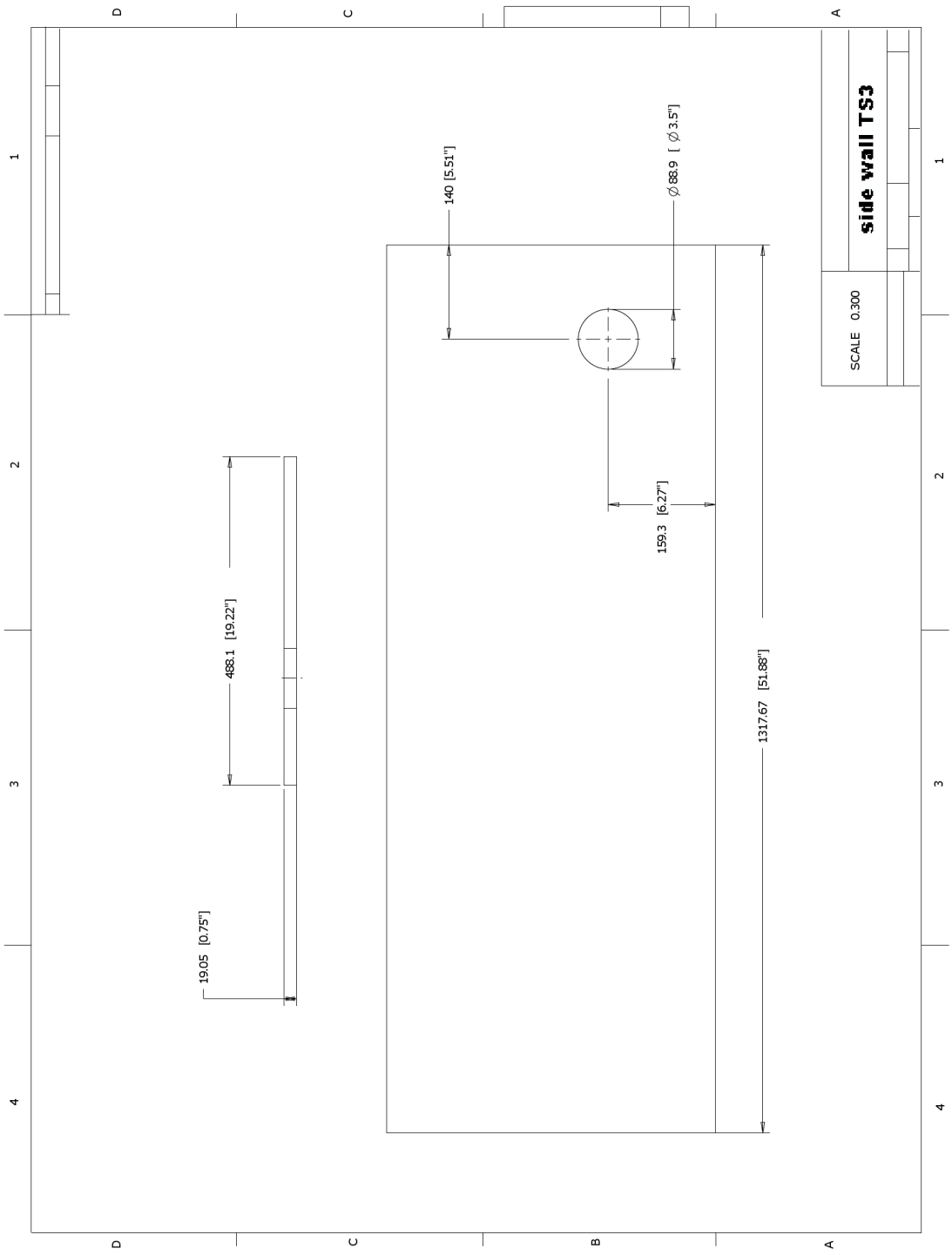
side wall TS3
SCALE 0.300
140 [5.51"]
Ø 88.9 [Ø3.5"]
159.3 [6.27"]
1317.67 [51.88"]
488.1 [19.22"]
19.05 [0.75"]

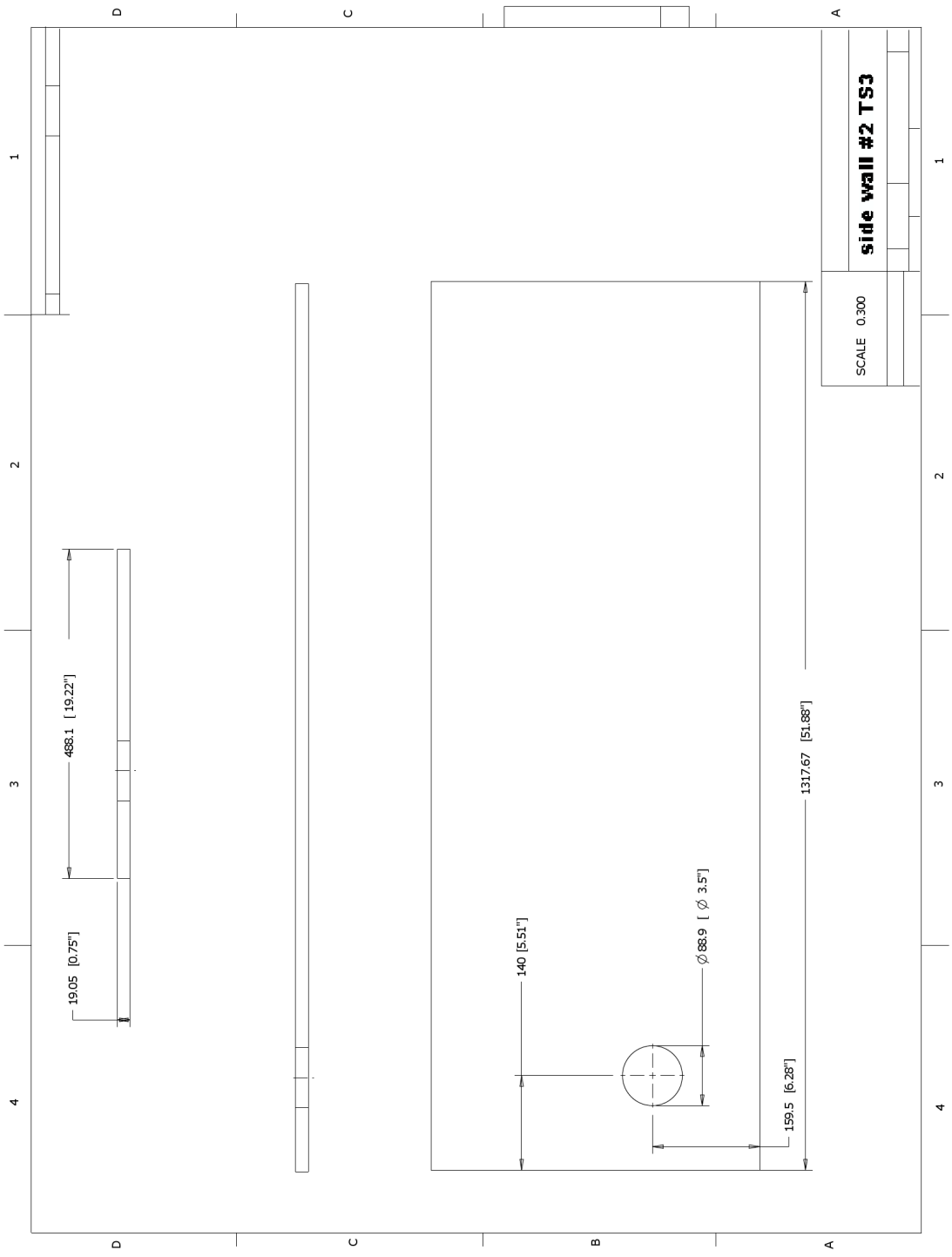
side wall #2 TS3
SCALE 0.300
488.1 [19.22"]
19.05 [0.75"]
140 [5.51"]
Ø 88.9 [Ø 3.5"]
159.5 [6.28"]
1317.67 [51.88"]

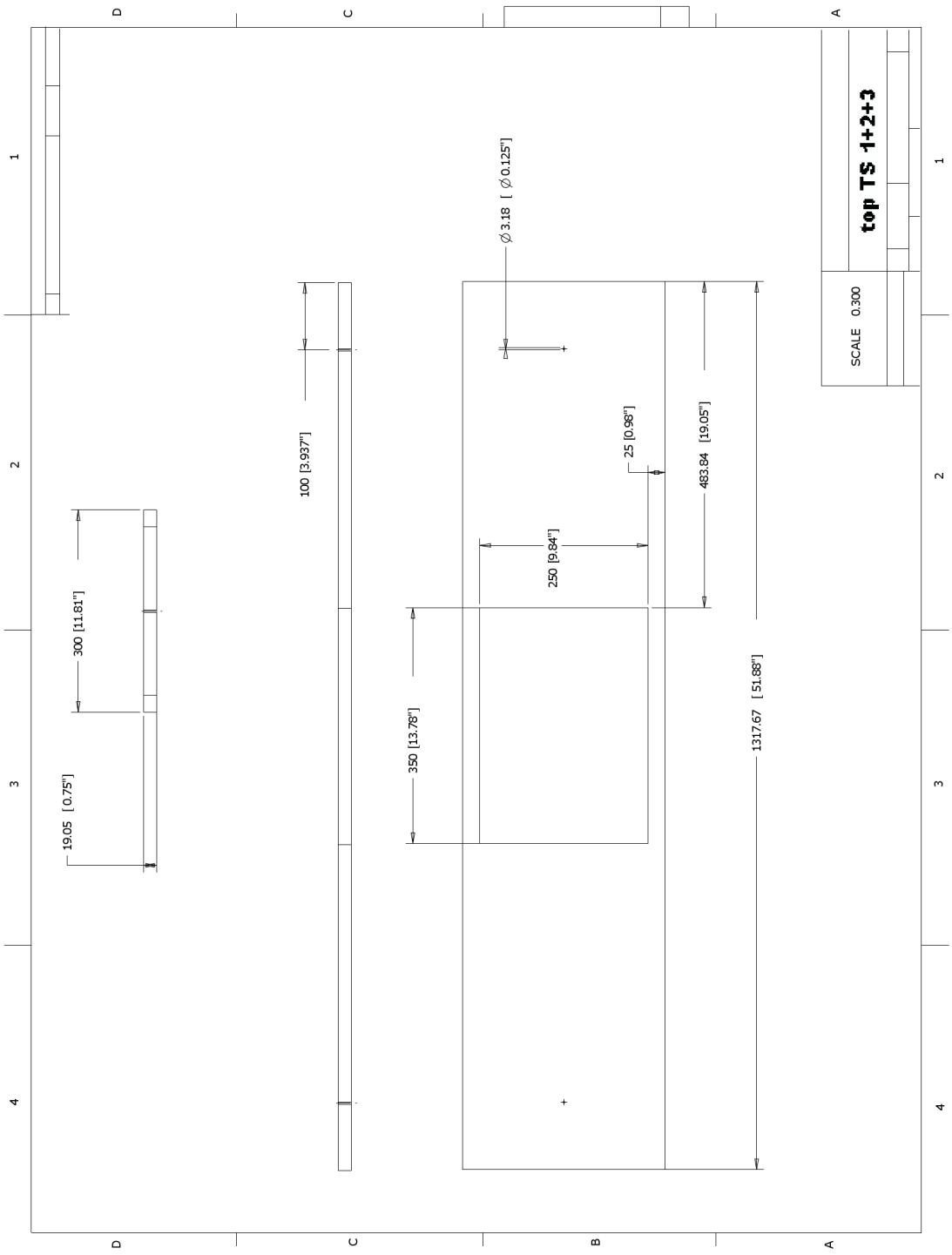
top TS 1+2+3
SCALE 0.300
Ø 3.18 [Ø 0.125"]
100 [3.937"]
25 [0.98"]
483.84 [19.05"]
250 [9.84"]
300 [11.81"]
350 [13.78"]
1317.67 [51.88"]
19.05 [0.75"]

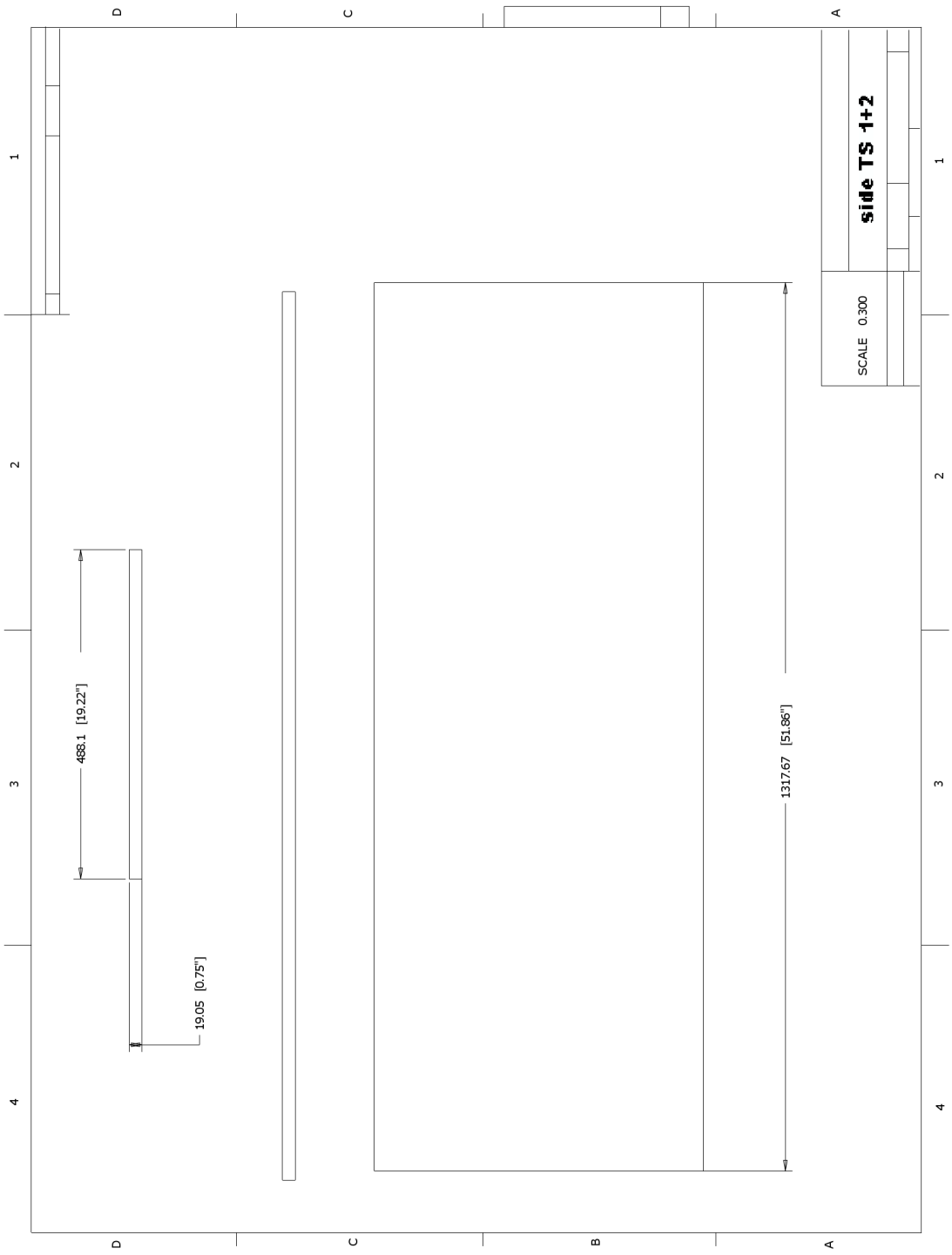
side TS 1+2
SCALE 0.300
488.1 [19.22"]
19.05 [0.75"]
1317.67 [51.86"]

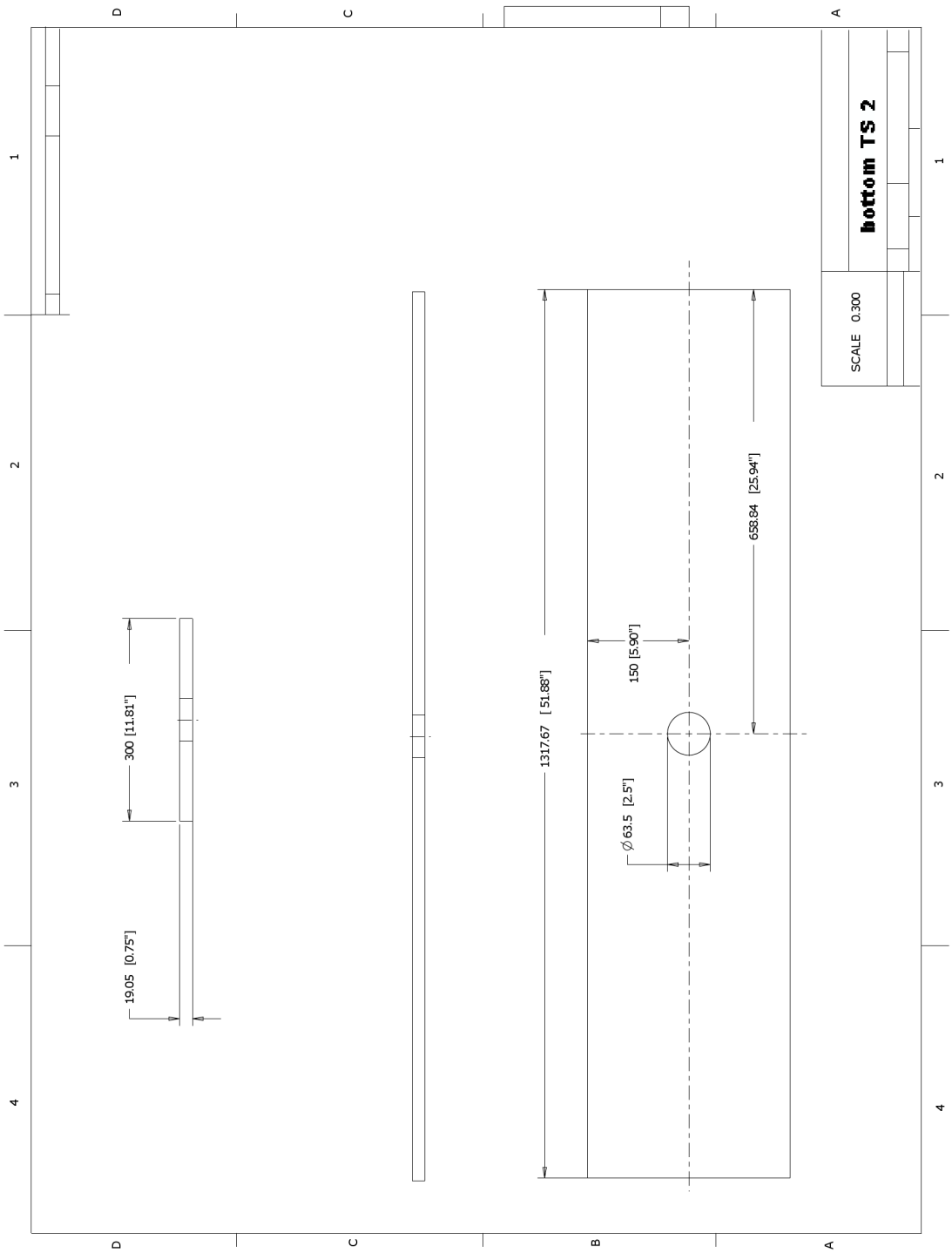
bottom TS 2
SCALE 0.300
1317.67 [51.88"]
658.84 [25.94"]
150 [5.90"]
Ø63.5 [2.5"]
300 [11.81"]
19.05 [0.75"]

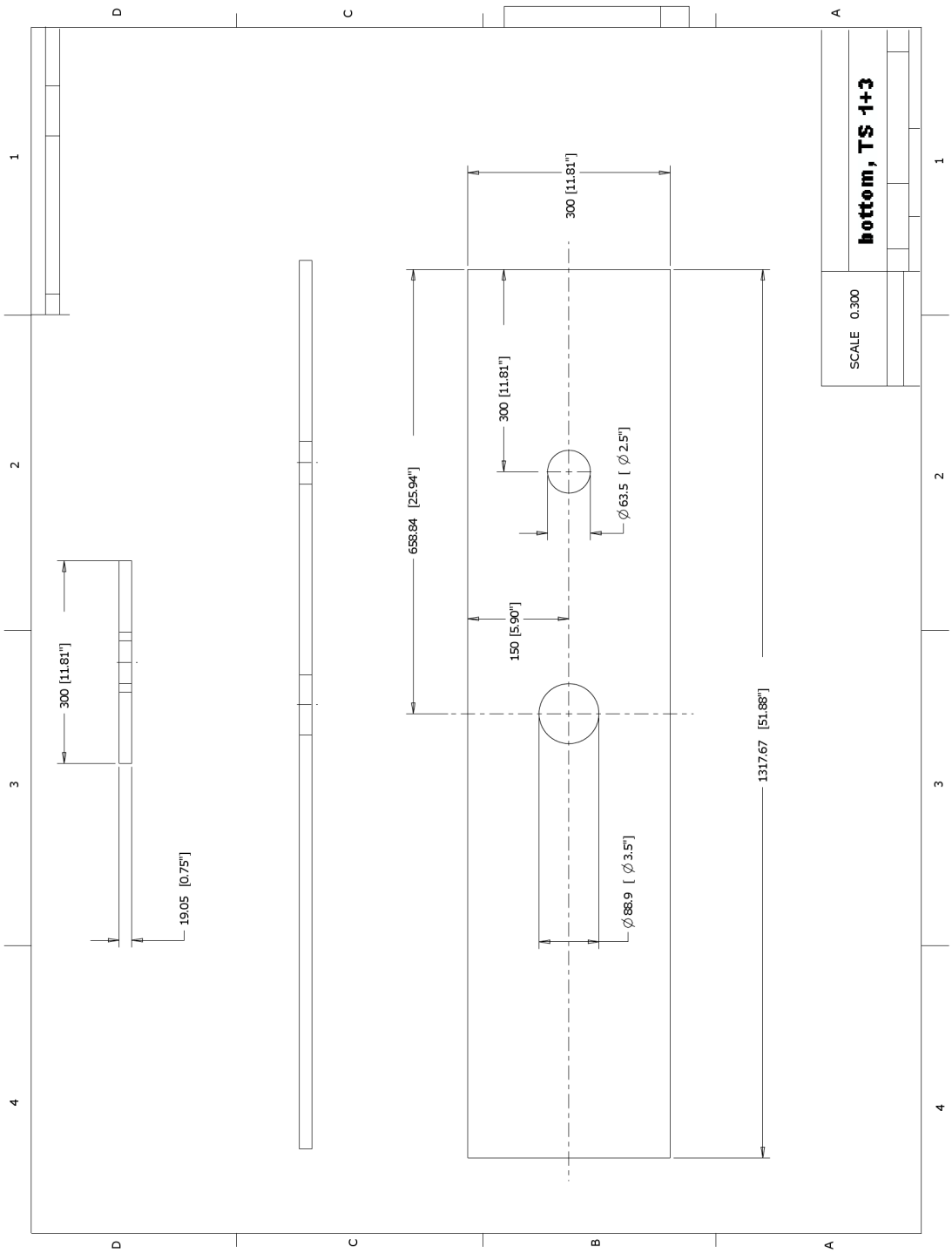
bottom, TS 1+3
SCALE 0.300
300 [11.81"]
658.84 [25.94"]
300 [11.81"]
Ø63.5 [Ø2.5"]
150 [5.90"]
1317.67 [51.88"]
Ø88.9 [Ø3.5"]
300 [11.81"]
19.05 [0.75"]

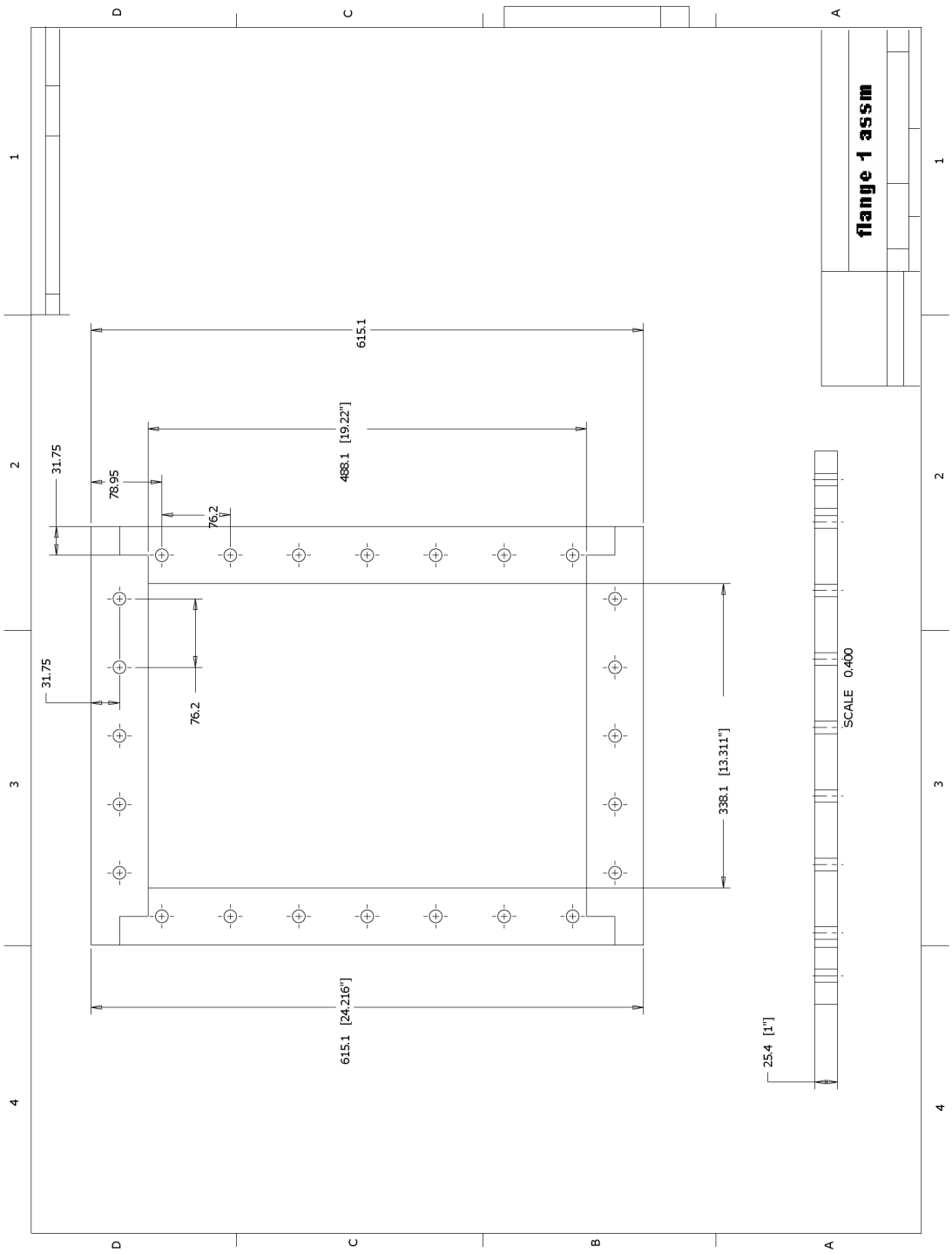
flange 1 assm
615.1
[19.22"]
488.1
31.75
78.95
76.2
31.75
76.2
338.1 [13.311"]
615.1 [24.216"]
SCALE 0.400
25.4 [1"]

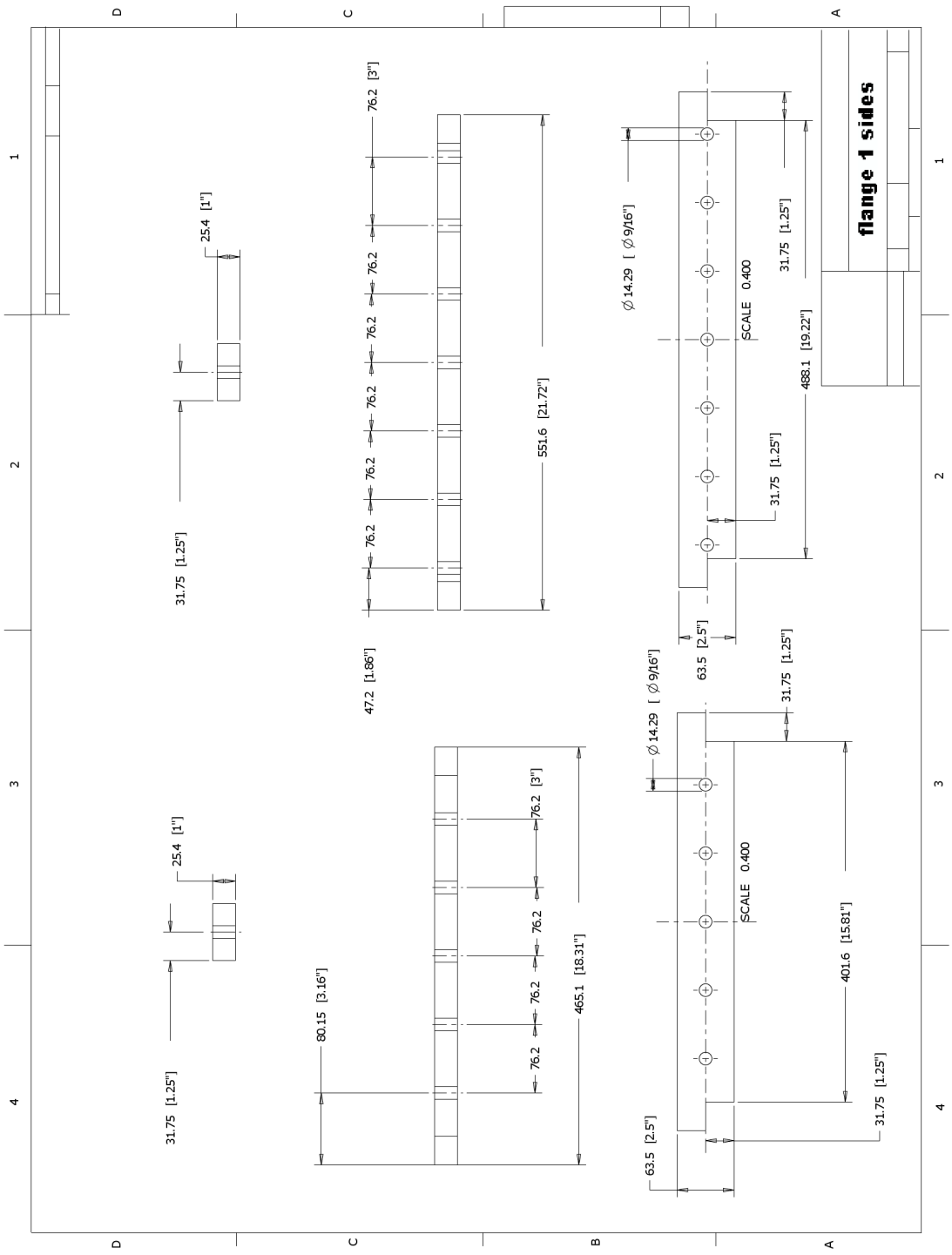
flange 1 sides
SCALE 0.400
SCALE 0.400
25.4 [1"]
31.75 [1.25"]
25.4 [1"]
31.75 [1.25"]
80.15 [3.16"]
76.2 [3"]
76.2
76.2
76.2
465.1 [18.31"]
47.2 [1.86"]
76.2 [3"]
76.2
76.2
76.2
76.2
551.6 [21.72"]
∅ 14.29 [∅ 9/16"]
63.5 [2.5"]
31.75 [1.25"]
401.6 [15.81"]
31.75 [1.25"]
∅ 14.29 [∅ 9/16"]
63.5 [2.5"]
31.75 [1.25"]
488.1 [19.22"]
31.75 [1.25"]

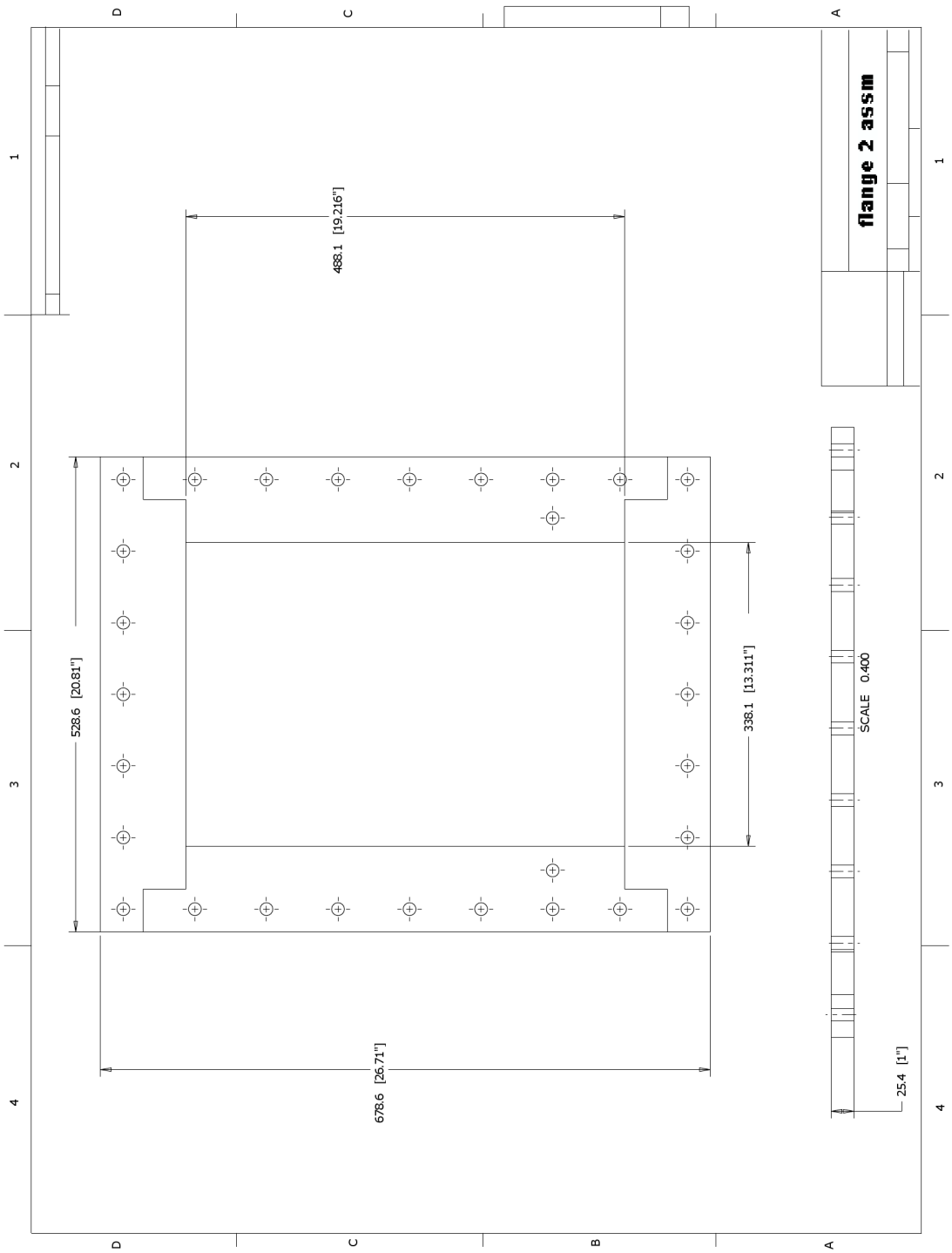
flange 2 assm
488.1 [19.216"]
528.6 [20.81"]
338.1 [13.311"]
678.6 [26.71"]
SCALE 0.400
25.4 [1"]

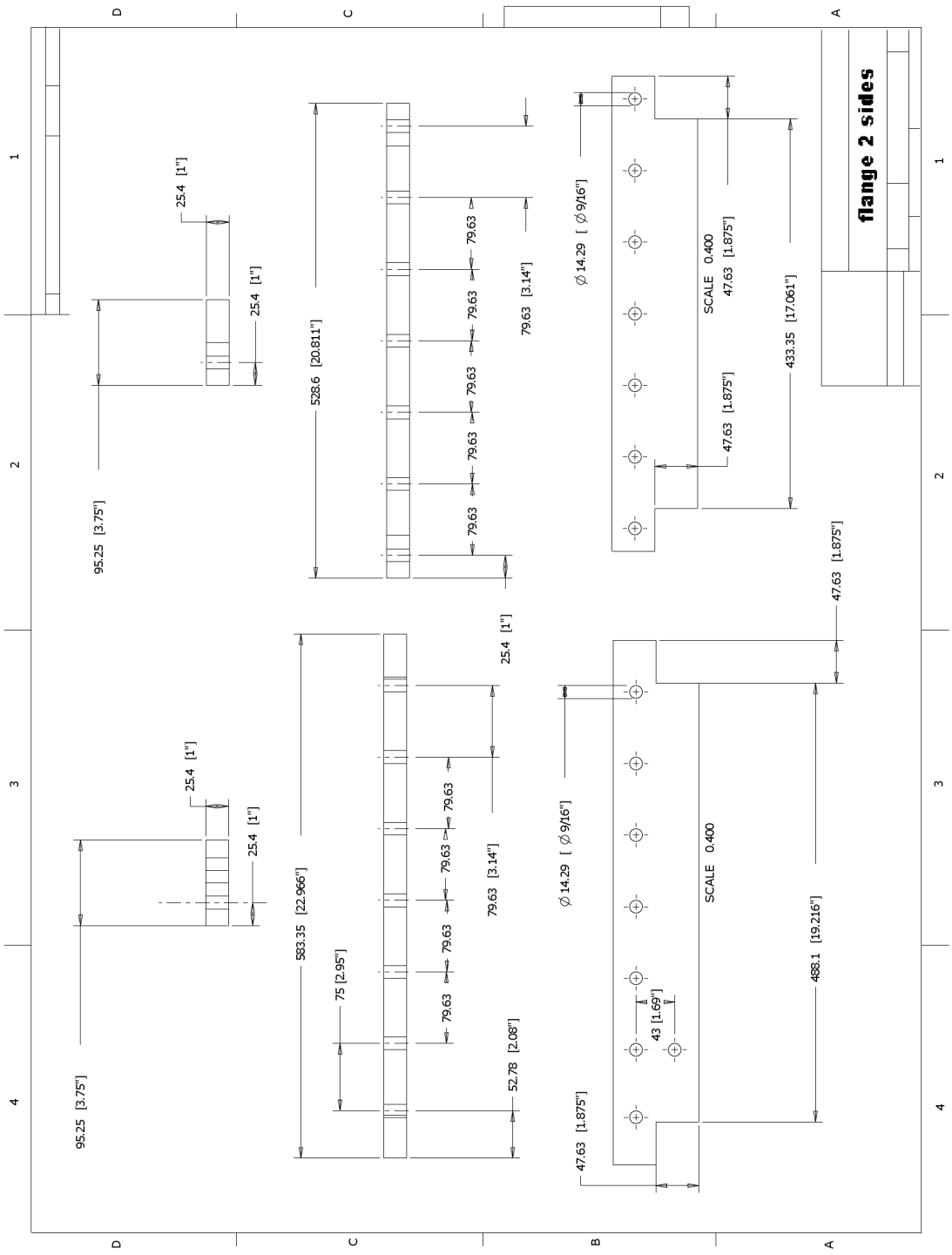
flange 2 sides
SCALE 0.400
SCALE 0.400
95.25 [3.75"]
25.4 [1"]
25.4 [1"]
528.6 [20.811"]
79.63 [3.14"]
79.63
79.63
79.63
79.63
79.63
79.63
Ø 14.29 [Ø9/16"]
47.63 [1.875"]
47.63 [1.875"]
433.35 [17.061"]
95.25 [3.75"]
25.4 [1"]
25.4 [1"]
583.35 [22.966"]
75 [2.95"]
79.63 [3.14"]
25.4 [1"]
79.63
79.63
79.63
79.63
52.78 [2.08"]
Ø 14.29 [Ø9/16"]
47.63 [1.875"]
47.63 [1.875"]
43 [1.69"]
488.1 [19.216"]
A
B
C
D
1
2
3
4

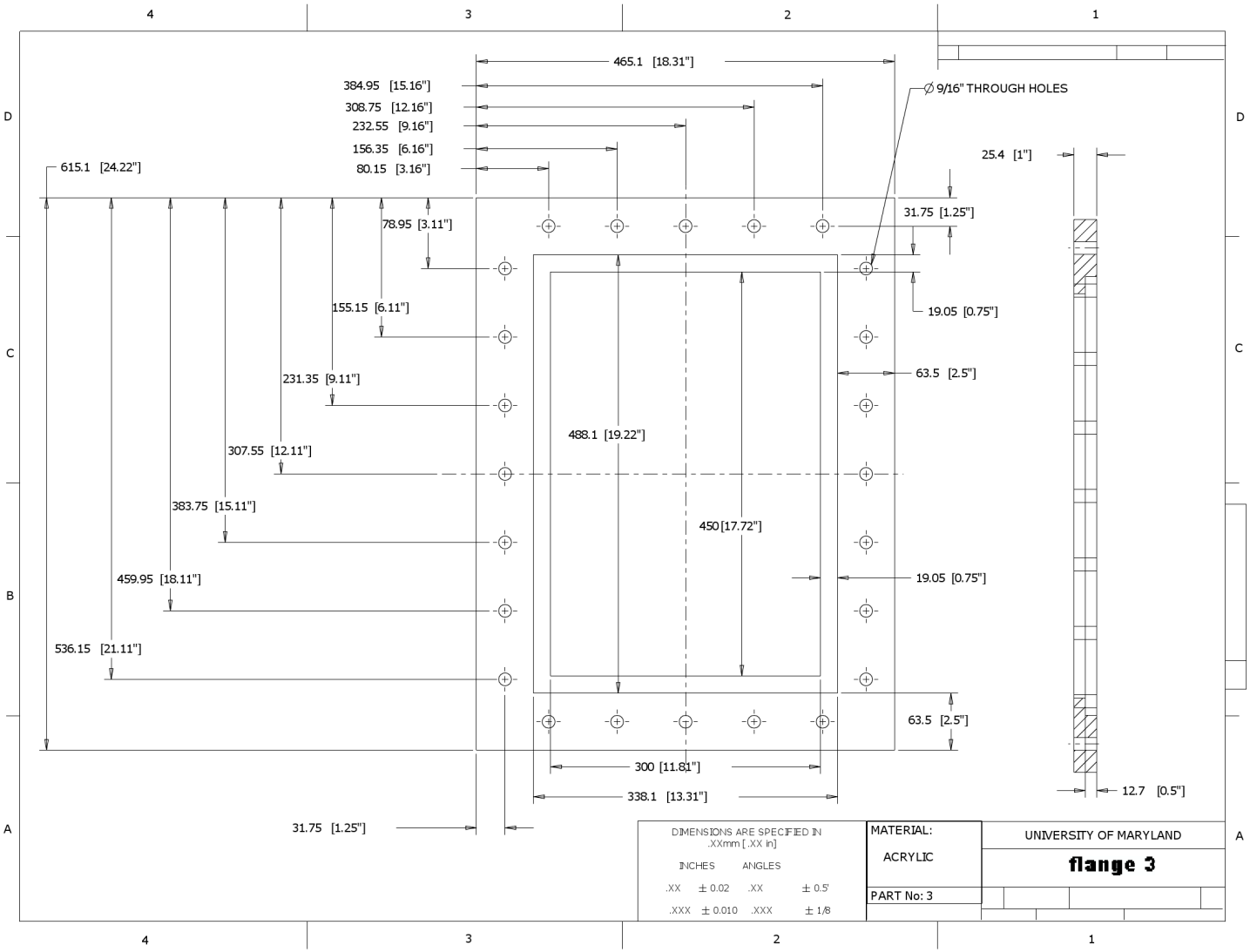
4
3
2
1
D
C
B
A
465.1 [18.31"]
384.95 [15.16"]
308.75 [12.16"]
232.55 [9.16"]
156.35 [6.16"]
80.15 [3.16"]
615.1 [24.22"]
∅ 9/16" THROUGH HOLES
25.4 [1"]
31.75 [1.25"]
78.95 [3.11"]
19.05 [0.75"]
155.15 [6.11"]
63.5 [2.5"]
231.35 [9.11"]
488.1 [19.22"]
307.55 [12.11"]
383.75 [15.11"]
450 [17.72"]
19.05 [0.75"]
459.95 [18.11"]
536.15 [21.11"]
63.5 [2.5"]
300 [11.81"]
338.1 [13.31"]
12.7 [0.5"]
31.75 [1.25"]
DIMENSIONS ARE SPECIFIED IN
.XXmm [.XX in]
INCHES ANGLES
.XX ± 0.02 .XX ± 0.5'
.XXX ± 0.010 .XXX ± 1/8
MATERIAL:
ACRYLIC
PART No: 3
UNIVERSITY OF MARYLAND
flange 3

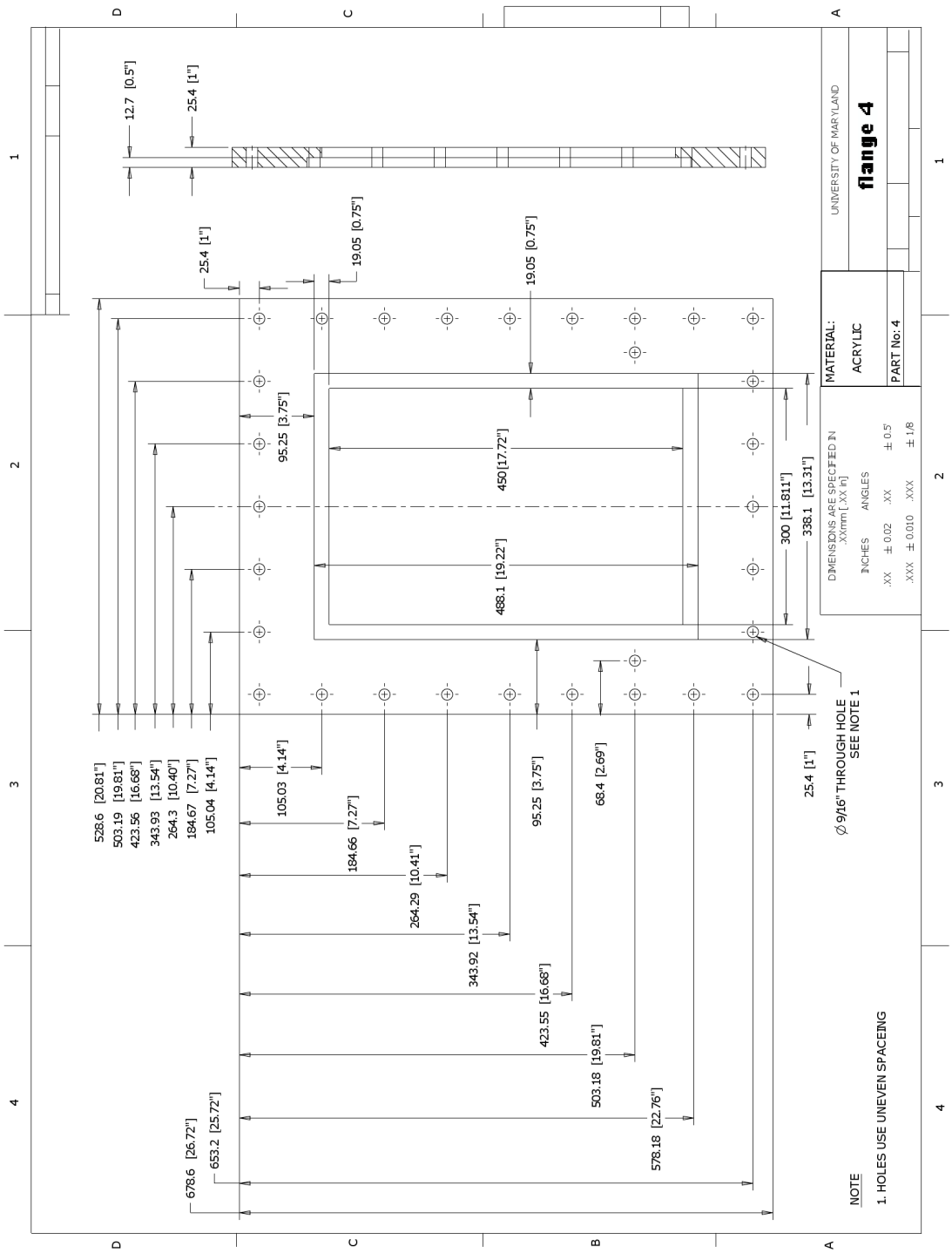
UNIVERSITY OF MARYLAND
flange 4
MATERIAL:
ACRYLIC
PART No: 4
DIMENSIONS ARE SPECIFIED IN
.XX[mm] [.XX in]
INCHES ANGLES
.XX ± 0.02 .XX ± 0.5°
.XXX ± 0.010 .XXX ± 1/8
12.7 [0.5"]
25.4 [1"]
19.05 [0.75"]
95.25 [3.75"]
450 [17.72"]
488.1 [19.22"]
300 [11.811"]
338.1 [13.31"]
Ø 9/16" THROUGH HOLE
SEE NOTE 1
528.6 [20.81"]
503.19 [19.81"]
423.56 [16.68"]
343.93 [13.54"]
264.3 [10.40"]
184.67 [7.27"]
105.04 [4.14"]
105.03 [4.14"]
184.66 [7.27"]
264.29 [10.41"]
343.92 [13.54"]
423.55 [16.68"]
503.18 [19.81"]
578.18 [22.76"]
653.2 [25.72"]
678.6 [26.72"]
68.4 [2.69"]
NOTE
1. HOLES USE UNEVEN SPACEING

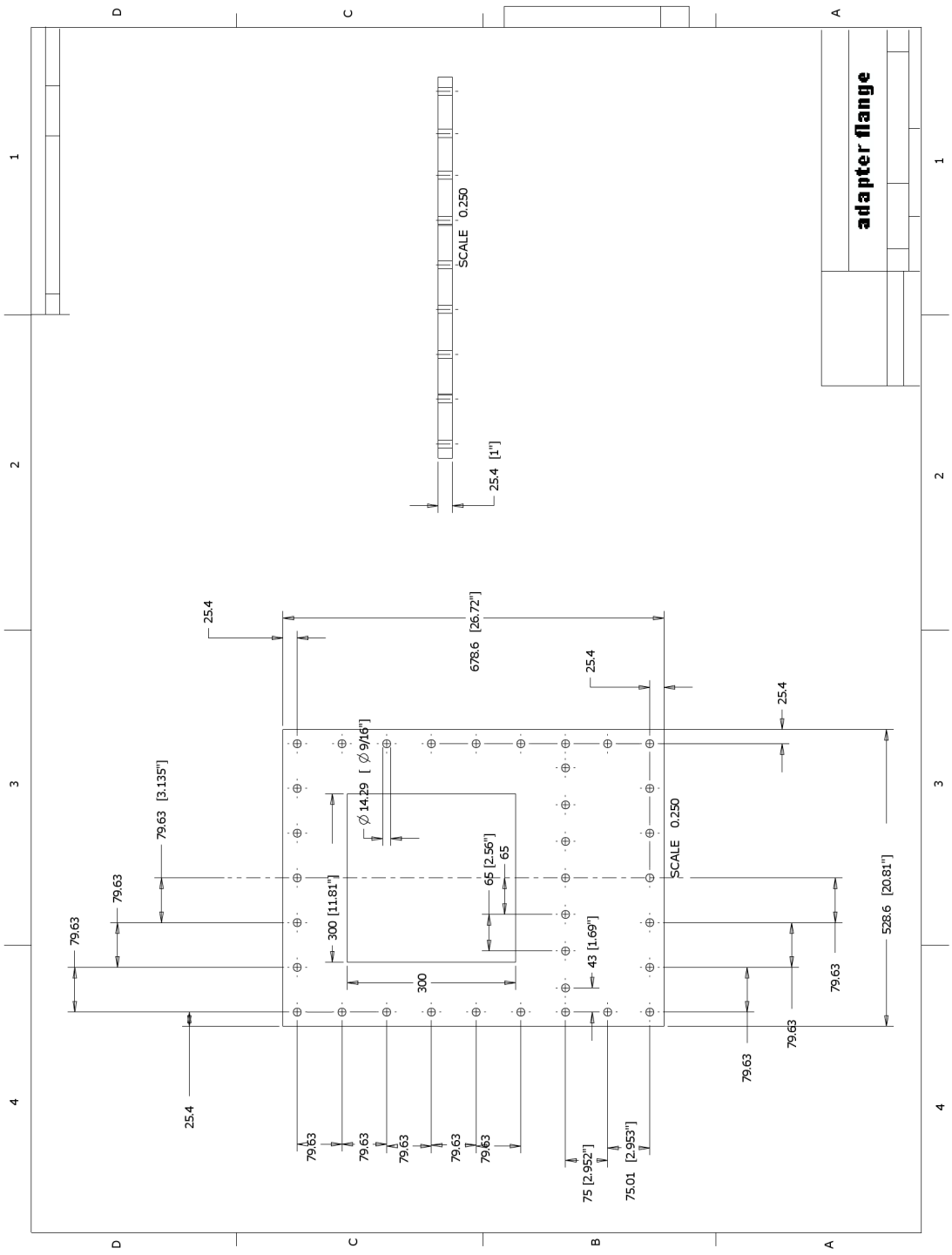
adapter flange
SCALE 0.250
25.4 [1"]
678.6 [26.72"]
25.4
79.63 [3.135"]
Ø 14.29 [Ø 9/16"]
65 [2.56"]
300 [11.81"]
43 [1.69"]
528.6 [20.81"]
75 [2.952"]
75.01 [2.953"]

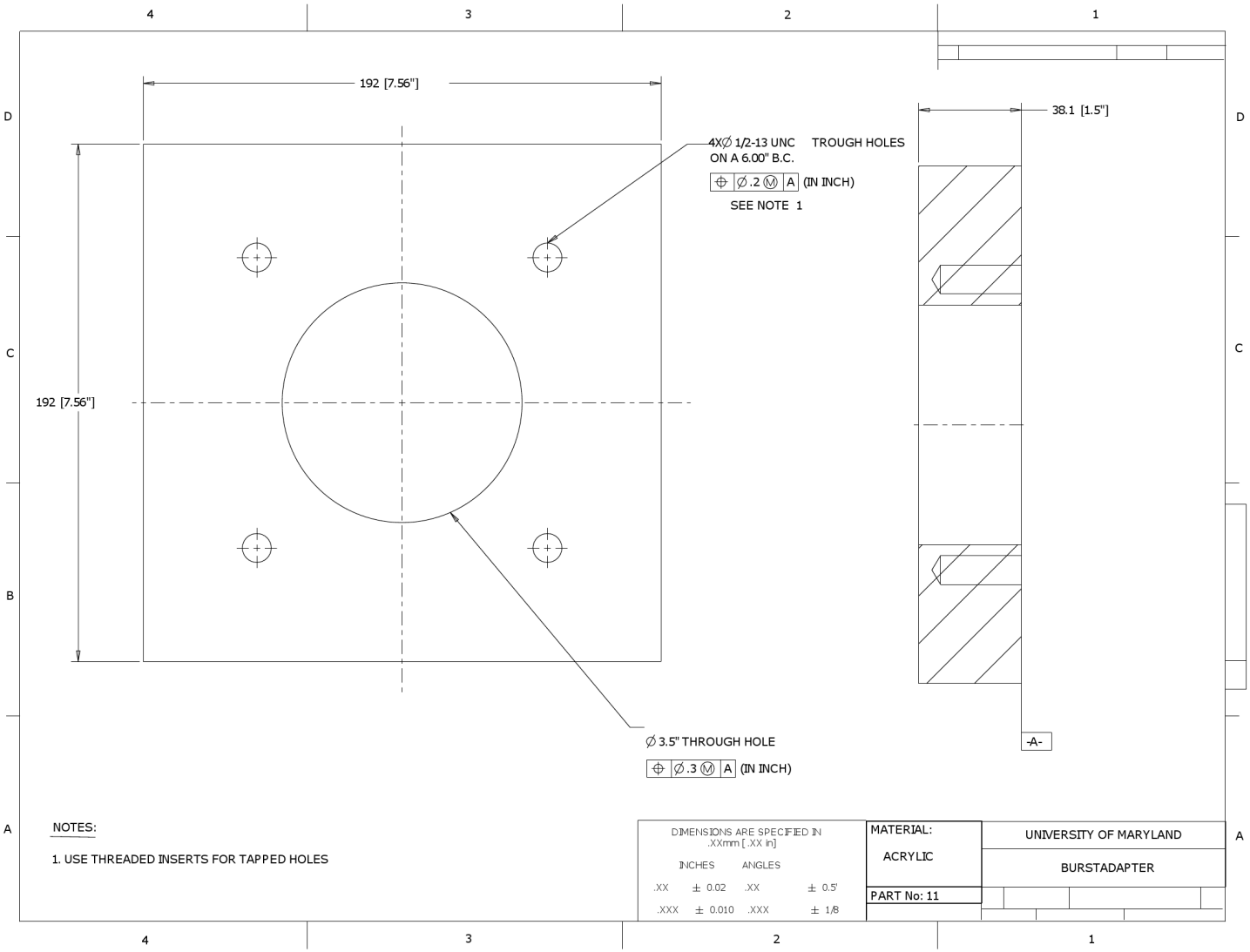
4
3
2
1
D
C
B
A
192 [7.56"]
192 [7.56"]
4XØ 1/2-13 UNC TROUGH HOLES
ON A 6.00" B.C.
Ø.2 M A (IN INCH)
SEE NOTE 1
38.1 [1.5"]
Ø 3.5" THROUGH HOLE
Ø.3 M A (IN INCH)
-A-
NOTES:
1. USE THREADED INSERTS FOR TAPPED HOLES
DIMENSIONS ARE SPECIFIED IN
.XXmm [.XX in]
INCHES ANGLES
.XX ± 0.02 .XX ± 0.5°
.XXX ± 0.010 .XXX ± 1/8
MATERIAL:
ACRYLIC
PART No: 11
UNIVERSITY OF MARYLAND
BURSTADAPTER

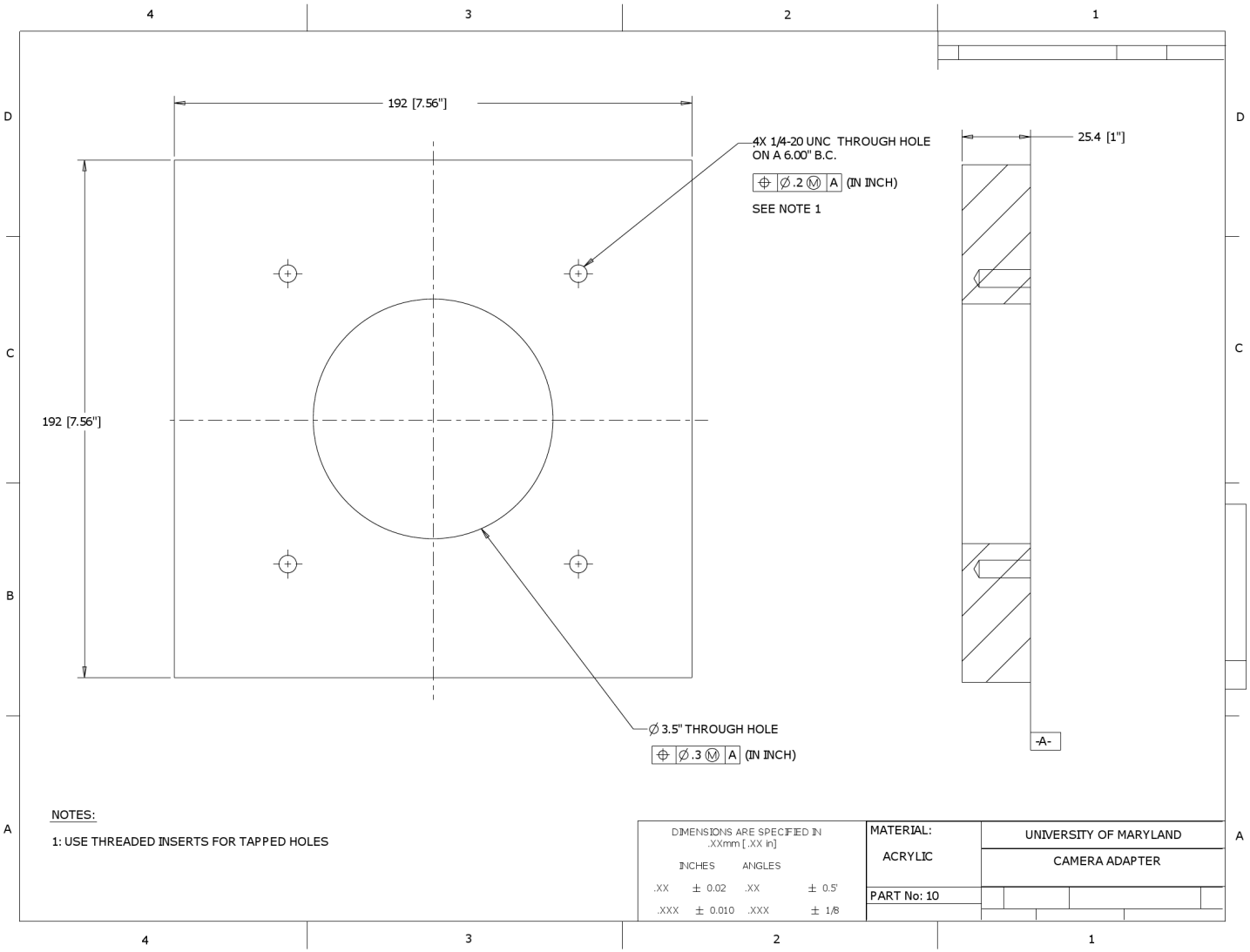
4
3
2
1
D
C
B
A
192 [7.56"]
192 [7.56"]
4X 1/4-20 UNC THROUGH HOLE
ON A 6.00" B.C.
⌖ Ø.2 Ⓜ A (IN INCH)
SEE NOTE 1
25.4 [1"]
-A-
Ø 3.5" THROUGH HOLE
⌖ Ø.3 Ⓜ A (IN INCH)
NOTES:
1: USE THREADED INSERTS FOR TAPPED HOLES
DIMENSIONS ARE SPECIFIED IN
.XXmm [.XX in]
INCHES ANGLES
.XX ± 0.02 .XX ± 0.5°
.XXX ± 0.010 .XXX ± 1/8
MATERIAL:
ACRYLIC
PART No: 10
UNIVERSITY OF MARYLAND
CAMERA ADAPTER

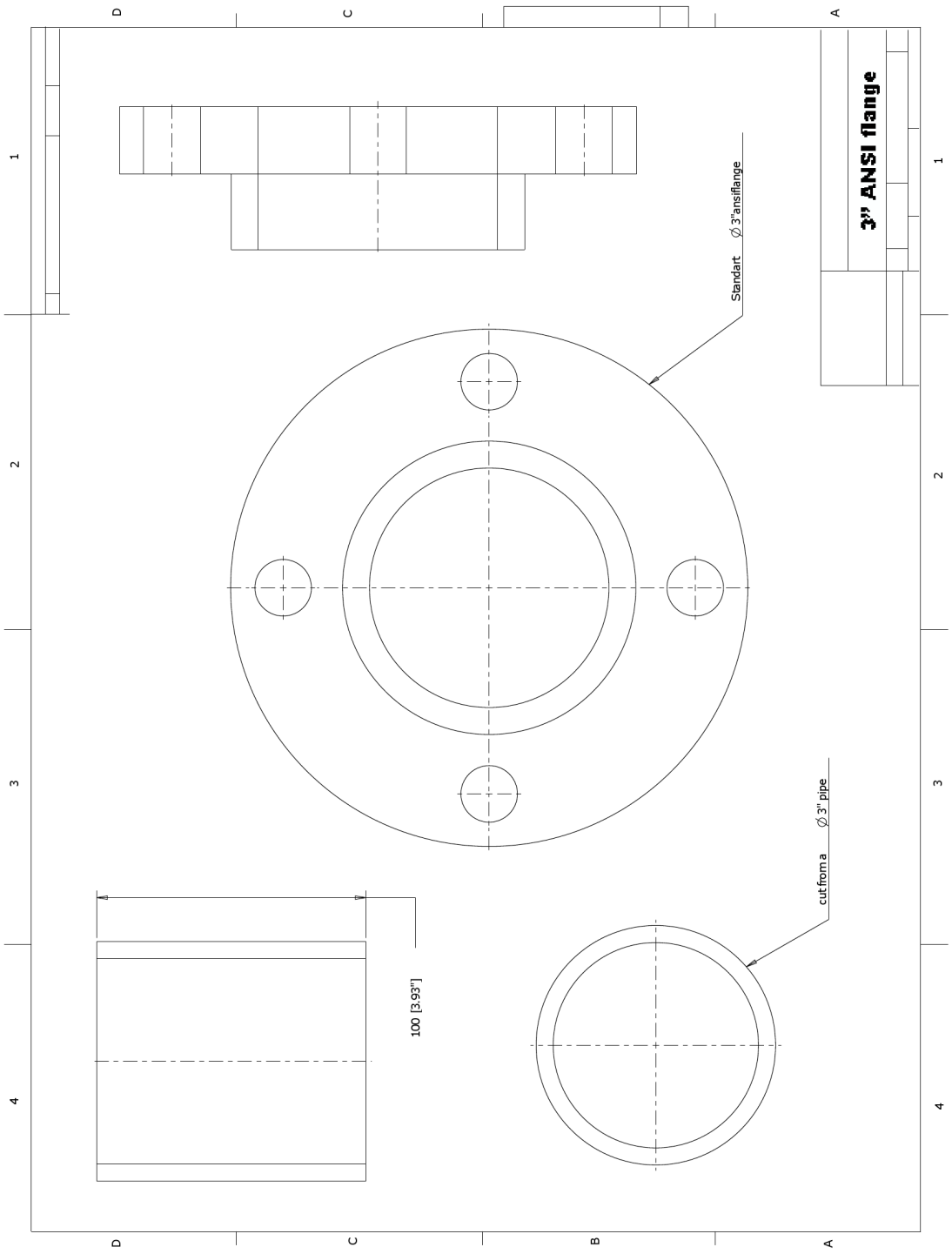
3" ANSI flange
Standart ∅ 3"ansiflange
cut from a ∅ 3" pipe
100 [3.93"]

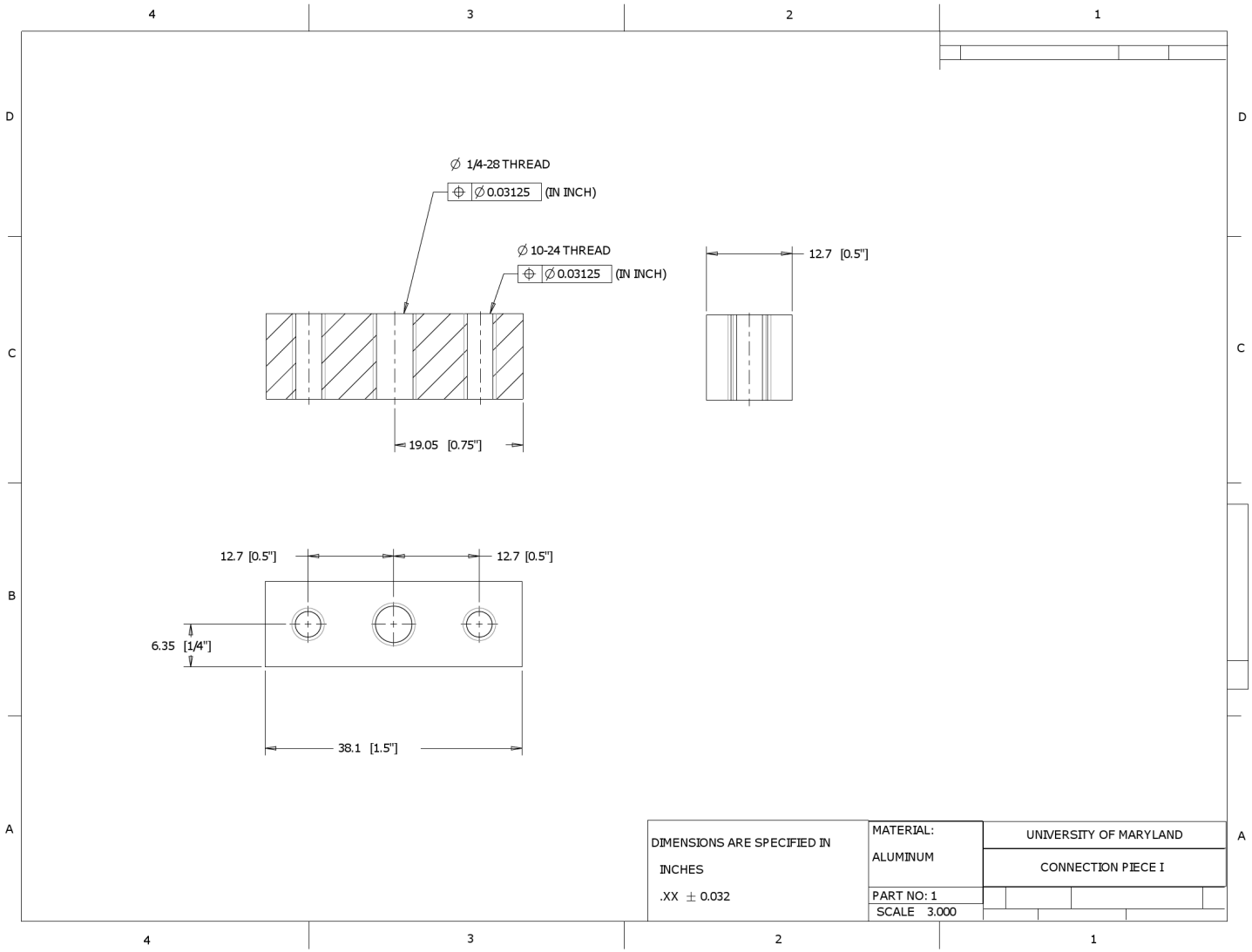
4
3
2
1
D
C
B
A
∅ 1/4-28 THREAD
∅0.03125 (IN INCH)
∅ 10-24 THREAD
∅0.03125 (IN INCH)
12.7 [0.5"]
19.05 [0.75"]
12.7 [0.5"]
12.7 [0.5"]
6.35 [1/4"]
38.1 [1.5"]
DIMENSIONS ARE SPECIFIED IN
INCHES
.XX ± 0.032
MATERIAL:
ALUMINUM
PART NO: 1
SCALE 3.000
UNIVERSITY OF MARYLAND
CONNECTION PIECE I

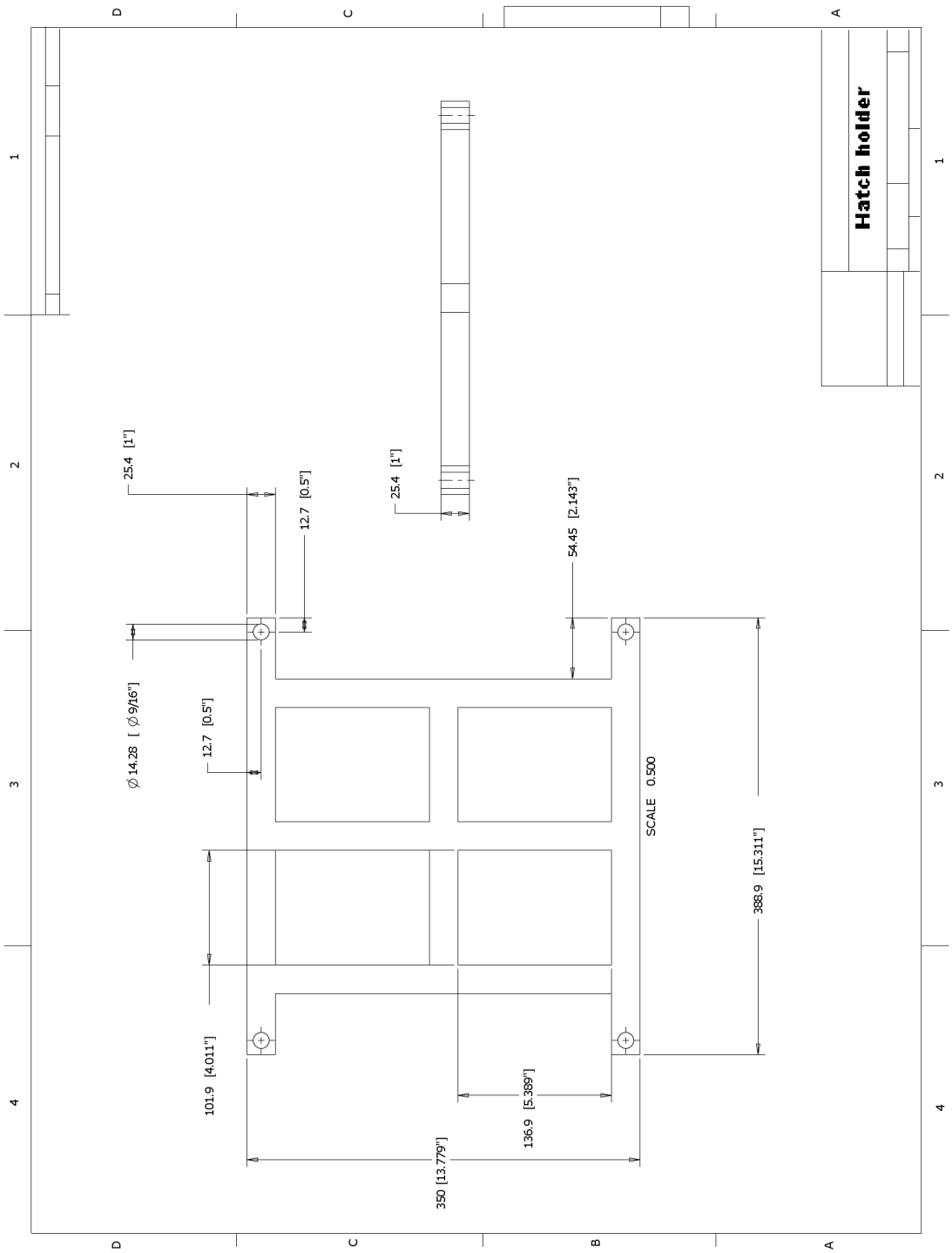
Hatch holder
SCALE 0.500
25.4 [1"]
12.7 [0.5"]
25.4 [1"]
54.45 [2.143"]
∅14.28 [∅9/16"]
12.7 [0.5"]
388.9 [15.311"]
101.9 [4.011"]
136.9 [5.389"]
350 [13.779"]

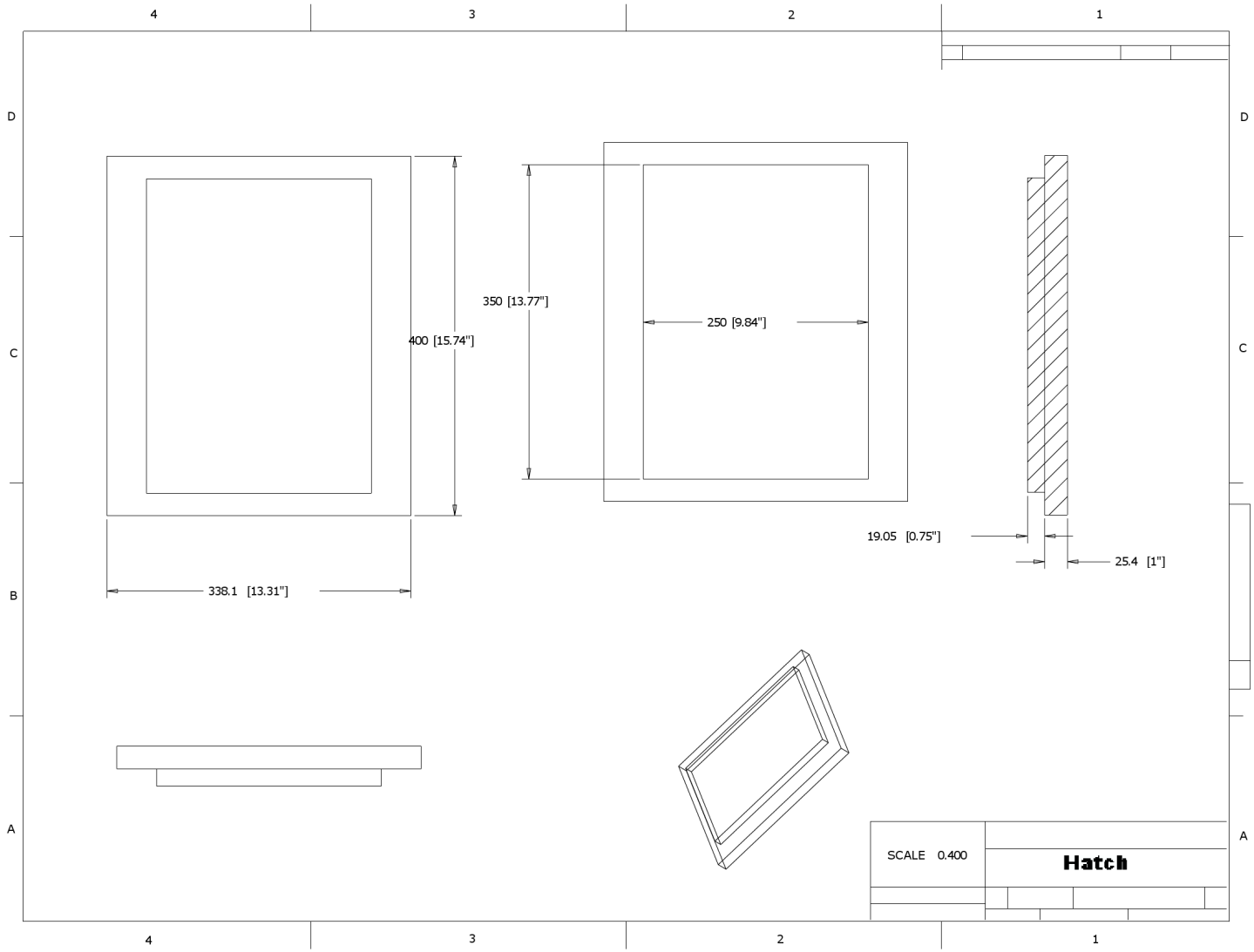
4
3
2
1
D
C
B
A
400 [15.74"]
338.1 [13.31"]
350 [13.77"]
250 [9.84"]
19.05 [0.75"]
25.4 [1"]
SCALE 0.400
Hatch

Bibliography

[1] Ishii, Mamoru and Takashi Hibiki. Thermo-fluid dynamics of two-phase flow. New York: Springer Science and Business media, 2006.

[2] Sleath, J. F. A. Sea bed mechanics. New York: John Wiley & Sons, 1984.

[3] Bagnold, R.A. "Motion of waves in shallow water. Interaction of waves and sand bottoms." *Proc. Roy. Soc* **187**(A):1-15, 1946.

[4] Anderson, K.H. "A Particle model of rolling grain ripples under waves" *Phys. Fluids*, **13**(1): 58-64, Jan 2001.

[5] Faraci, C. and E. Foti "Geometry, migration and evolution of small-scale bedforms generated by regular and irregular waves" *Coastal Eng.*, **47**: 32-52, 2002.

[6] Mogridge, G. R. and J. W. Kamphuis. "Experiments on bed form generation by wave action". *Proc. 13th Conf. Coastal Eng. Vancouver.* 1123-1142, 1972

[7] Nielsen, P. "Dynamics and geometry of wave-generated ripples" *J. Geophys. Res.*, **86**(C7):6467-6472,1981.

[8] Mogridge, G.R., M.H. Davies, and D.H. Willis "Geometry prediction for wave-generated bedforms" *Coastal Eng.*, **22**, 255286, 1994

[9] O'Donoghue, T. and G.S. Clubb "Sand ripples generated by regular oscillatroy flow" *Coastal Eng.*, **44**: 101-115, 2001.

[10] Wiberg. P.L. and C.K. Harris "Ripple geometry in wave-dominated environment" *J. Geophys. Res.*, **99**(C1):775-789, 1994.

[11] Vongvisessomjai, S. "Oscillatory ripple geometry" *J. Hydraul. Eng., Am. Soc. Civ. Eng.* **110**(3):247-266, 1984.

[12] Vincent, G.E. "Contribution to the study of sedimenttransport on a horizontal bed due to wave action" *Proc. 6th Conf. Coastal Eng. Miami.* 326-355, 1952

[13] Lyne W.H. "Unsteady viscous flow over a wavy wall" *J. Fluid Mech.*, **50**:33-48, 1971.

[14] Nakato, T., M. Kennedy, J. Glover and F. Locher "Wave Entrainment of Sediment from Rippled Beds" *J. Waterway Port C. Div* **103**:1 83-99, 1977.

[15] Coleman, N. L. "Flume studies of the sediment transfer coefficient" *Water Resource Res* **6**(3):801-809, 1970.

[16] van der Werf, J.J., J.S. Ribberink, T. O'Donoghue, and J.S. Doucette "Modelling and measurement of sand transport processes over full-scale ripples in oscillatory flow" *Coastal Eng.*, **53**, 657-673, 2006.

[17] Nielsen, P. "Entrainment and distribution of different sand sizes under water waves". *J Sedimentary Petrology* **52**(2):423-428, 1983.

[18] Sleath J.F.A. "The suspension of sand by waves" *J. Hydraul Res.* **20** 439-452, 1982.

[19] Nielsen, P. Coastal bottom boundry layers and sediment transport, World Scientific Publishing Co., Singapore, 1992.

[20] Lee, T.H., and D.M. Hanes "Comparison of field observations of the vertical distribution of suspended sand and its prediction by models" *J. Geophys. Res.*, **101**, 35613572, 1996.

[21] Thorne, P. D., J. J. Williams and A. Davies. "Suspended sediments under waves measured in a large scale flume facilty" *J. Geophys. Res.*, **107**(C8): 1-16,2002.

[22] Earnshaw, H.C. and Greated C.A. "Dynamics of ripple bed vortices" *Exp. Fluids*, **25**: 265-275, 1998.

[23] Sleath, J. F. A. and S. Wallbridge. "Pickup from rippled beds in oscillatory flow" *J. Wat. Port Coast. Ocean Engrg.*, **128**(6):228-237, 2002.

[24] Mutlu Sumer, B., L. Chua, N. Cheng, and J. Fredsoe "Influence of Turbulence on Bed Load Sediment Transport" *J. Hydraul. Eng.* **129**(8): 585-596, 2003.

[25] Bosman, J.J. and H.J. Steetzel "Time- and bed-averaged concentration under waves" *Proc. 20th ICCE Taipei. ASCE*, 9861000, 1986.

[26] Dick, J. E. and J. F. A. Sleath. "Velocities and concentrations in oscillatory flow over beds of sediment" *J. Fluid Mech.*, **233**:165-196, 1991.

[27] Ribberink J. and A. Al-Salem "Sheet flow and suspension of sand in oscillatory boundary layers" *Coastal Eng.*, **25**: 205-225, 1995.

[28] Flores, N. Zala and J. F. A. Sleath. "Mobile layer in oscillatory sheet flow" *J. Geo. Res.*, **103**(C6):12783-12793,1998.

[29] Ahmed, A.S.M. and S. Sato "Investigation of bottom boundary layer dynamics of movable bed by using enhanced piv technique" *Coastal Eng.*, **43**(4): 239-258, 2001.

[30] Dohmen-Janssen, C. M., W.N. Hassan, and J.S. Ribberink. "Mobile-bed effects in oscillatory sheet flow" *J. Geophys. Res.*, **106**(C11):27103-27115, 2002.

[31] Horikawa, H. and S. Mizutani "Oscillatory flow behavoir in the vicinity of ripple models" *Proc. 23rd Int. Conf. Coastal Eng.*, 2122-2135, 1992.

[32] Scotti, A. and U. Piomelli. "Numerical simulation of pulsating turbulent channel flow". *Phys. Fluids*, **13**(5): 1367-1384, May 2001.

[33] Chang, Y. and A. Scotti "Modeling unsteady turbulent flows over ripples: Reynolds-averaged Navier-Stokes equations (RANS) versus large-eddy simulation (LES)" *J. Geophys. Res.*, **109**,C09012, doi:10.1029/2003JC002208, 2004

[34] Wang, Q, K.D. Squires and O. Simonin. "Large eddy simulation of turbulent gas-solid flows in a vertical channel and evaluation of the second-order models." *Int. J. Heat and Fluid Flow.*, 19: 505-511, 1998.

[35] Simonin, O., E. Deutsch, M. Boivin. "Large eddy simulation and second-moment closure model of particle fluctuating motion in two-phase turbulant shear flows" *Turbulant Shear Flow* **9**:85-115, 1995.

[36] Chang, Y. and A. Scotti "Turbulent convection of suspended sediments due to flow reversal" *J. Geophys. Res.*, **111**, C07001, doi:10.1029/2005JC003240, 2006

[37] Raffel, M., C. Willert, and J. Kompenhans Particle Image Velocimetry. New York: Springer, 1998.

[38] Bosman, J.J., E. Van der Velden and C.H. Hulsbergen, "Sediment concentration measurements by transverse suction" *Coastal Eng.*, **11**: 353-370, 1987.

[39] Riley, C. Acree and M.Y. Louge "Quantitative capacitive measurements of voidage in dense gassolid flows" *Part. Sci. Technol.* **7** 51-57, 1989.

[40] Crowe, C. , M. Sommerfeld and Y. Tsuji Multiphase flows with droplets and particles, CRC Press, New York, 1998.

[41] Jonasz, M. and G. Fourmier Light scattering by particles in water: theoretical and experiment Academic Press, Amsterdam, 2007.

[42] Downing, J.P, R.W. Sterberg and C.R.B. Lister "New Instrumentation for the investigation of sediment suspension processes in the shallow marine environment." *Mar. Geol.* **42** 19-34, 1981.

[43] Sheng J. and A. E. Hay, "An examination of the spherical scatterer approximation in aqueous suspensions of sand" *J. Acoust. Soc. Am.* **83**: 598610, 1988.

[44] Thorne P.D and S.C. Campbell, "Backscattering by a suspension of spheres" *J. Acoust. Soc. Am.* **92**: 978986, 1992.

[45] Crawford, A.M., and Hay, A.E. "Determining suspended sand size and concentration from multifrequency acoustic backscatter." *J. of the Acoustical Society of America*, **94**(6): 3312-3324, 1993.

[46] Best J., S Bennett, J. Bridge and M. Leader "Turbulence Modulation and Particle Velocities over Flat Sand Beds at Low Transport Rates" *J. Hydraulic Engr.* **123**:12 11181129, 1997.

[47] Bennett S.J. and J.L. Best "Particle Size and Velocity Discrimination in a Sediment-Laden Turbulent Flow Using Phase Doppler Anemometry" *J. Fluids Engr.* **117**: 505511, 1995.

[48] Qiu H.H. and M. Sommerfeld "A reliable method for determining the measurement volume size and particle mass fluxes using phase-Doppler anemometry" *Exp. Fluids*, **13**(6): 393-404, 1992.

[49] Albrecht H.E., M. Borys, N. Damaschke and C. Tropea *Laser Doppler and Phase Doppler Measurement Techniques* Springer, Berlin, 2003

[50] Westerweel, J. "Fundamentals of digital particle image velocimetry." *Meas. Sci. Technol.* **8** 1379-1392, 1997.

[51] Adrian, R. J. "Particle-imaging techniques for experimental fluid mechanics" *Ann. Rev. Fluid Mech.* **23**: 261-304, 1991.

[52] Philip O G, Schmidl W D and Hassan Y A "Development of a high speed particle image velocimetry technique using fluorescent tracers to study steam bubble collapse" *Nucl. Eng. Des.* **149** 375-385, 1994

[53] Sridhar, G. and J. Katz "Drag and lift forces on microscopic bubbles entrained by a vortex" *Phys. Fluids* **7** 389-399, 1995.

[54] Delnoij, E., J. Westerweel, N. Deen, J. Kuipers, W. Swaaij "Ensemble-Correlation PIV applied to bubble plumes rising in a bubble column" *Chem. Eng. Sci.* **54** 5159-5171, 1999.

[55] Khalitov, D. A. and E. K. Longmire. "Simultanous two-phase PIV by two-parameter phase discrimination." *Exp. Fluids*, **32**(2): 252-268, 2002.

[56] Kiger, K. T. and C. Pan. "PIV technique for the simultaneous measurement of dilute two-phase flows." *J. Fluids Eng.*, **122**: 811-818, 2000.

[57] Lindken R. and W. Merzkirch "A novel PIV technique for measurements in multiphase flows and its application to two-phase bubbly flows" *Exp. Fluids*, **33**: 814-825, 2002.

[58] van der Mark, M. B., M. P. van Albada and A. Lagendijk "Light scattering in strongly scattering media: Multiple scattering and weak localization" *Phys. Rev. B*, **37**(7): 3575-3592, 1988.

[59] van der Werf, J.J., J.S. Doucette, T. O'Donoghue, and J.S. Ribberink "Detailed measurements of velocities and suspended sand concentrations over full-scale ripples in regular oscillatory flow" *J. Geophys. Res.*, **112**, F02012, doi:10.1029/2006JF000614, 2007

[60] Westerweel, J. and F. Scarano "Universal outlier detection for PIV data" *Exp. Fluids* **39**:6 1096-1100, 2005.

[61] Hage B. and J. Werther "The Guarded Capacitance Probe - A Tool for the Measurement of Solids Flow Patterns in Laboratory and Industrial Fluidized-Bed Combustors" *Powder Technology* **93** 234-245, 1997.

[62] Rundqvist R, A. Magnusson, B. G. M. van Wachem, and A. E. Almstedt, "Dual optical fibre measurements of the particle concentration in gas/solid flows" *Exp. Fluids*, **35**(6): 572-579, 2003.

[63] Maxey M.R. and J.J. Riley "Equation of motion for a small rigid sphere in a nonuniform flow" *Phys. Fluids*, **26**(4): 883-889, 1983.

[64] D.A. Drew "Mathematical modeling of two-phase flow" *Ann. Rev. Fluid Mech.*, 15: 261-291, 1983.

[65] Ishii, M. and K. Mishima "Two-fluid Model and Hydrodynamic Constitutive Relations" *Nucl. Eng. Des.*, **82**: 107-126, 1984.

[66] Schillar L. and Naumann, A., "Uber die grundlegenden Berechungen bei der Schwerkraftaufbereitung", *Ver. deut. Ing.*. **77**, 318, 1933

[67] Armenio, V. and V. Fiorotto "The importance of the forces acting on particles in turbulent flows" *Phys. Fluids*, **13**(8): 2437-2440, Aug 2001.

[68] Sleath, J. F. A. "On rolling grain ripples". *J. Hydraul. Res.* **14**(1): 69-81, 1976.

[69] Sleath, J. F. A. "Measurements of the bed load in oscillatory flow" *J. Waterway, Port, Coast. And Ocean Div.*, **104**(4): 291-307, 1978.